UNITED NATIONS EDUCATIONAL, SCIENTIFIC AND CULTURAL ORGANIZATION
INTERNATIONAL ATOMIC ENERGY AGENCY
INTERNATIONAL CENTRE FOR THEORETICAL PHYSICS
I.C.T.P., P.O. BOX 586, 34100 TRIESTE, ITALY, CABLE: CENTRATOM TRIESTE

SMR/989 - 22

"Course on Shallow Water and Shelf Sea Dynamics"
7 - 25 April 1997

"Numerical Model Exercises"

A. PARES-SIERRA
CICESE
Ensenada
Mexico

Please note: These are preliminary notes intended for internal distribution only.

Program

1: Some needed theory

2: Vertical diffusion in the sea

3: A one-dimensional tidal model
advection-diffusion equation

4: Topographic waves. Weak bottom slope.

5: More Topographic waves

6: Kelvin waves. Reduced gravity equation.
Boundary conditions.

7: Aplication: The California Current

8: Capacitance method.

Programs

	model	in	out	plot
ex1.d	Vertdif.f	vertdif.in	vertdif.out vertdif.out2	→ plvd.f
	Vertdifhh.f	(to compute h of penetration for $\Delta x = 2, \ldots N-1$		
ex2.d	Tide2.f	Tide2.dat2	Tide.out Tide.nf	→ pltide.f
	Tideaddif.f (with advection diffusion eq)	Tide2dat2	Tide.out Tide.nf	→ pltide2.f
	Tideaddifend.f (right side closed)	"	"	
ex3.d	Topo.f ($\alpha=0$)		uTopo vTopo HTOPO	plTopo.f
ex4.d	bumps.f (~~with~~ exponential topography, $\gamma \neq 0$) $\tau^* = \sin(kz)$)		ubumpc vbumpc Hbumpc	plbumps.f
	bumps2.f (constant wind, $\gamma = .130$)			
ex5.d	Redgrav.f			
	Creared.f	To create the mask needed for redgrav.f to run		

The objective of this presentation is to illustrate with a few simple computer exercises some of the phenomena that can occur near a coast and at the same time the process of passing from the physical to the numerical model.

We would like to implement, for example, the numerical version of a model like:

$$\frac{\partial U}{\partial t} - fV = -gH\frac{\partial \eta}{\partial x} + F_x - B_x$$

$$\frac{\partial V}{\partial t} + fU = -gH\frac{\partial \eta}{\partial y} + F_y - B_y$$

$$\frac{\partial U}{\partial x} + \frac{\partial V}{\partial y} = -\frac{\partial \eta}{\partial t}$$

+ Some geometry, boundary conditions, bathymetry, etc.

One way of doing this is by the use of finite differences which consist on transforming the partial derivatives into its numerical approximations. There are many possibilities leading to many different numerical schemes.

From the Taylor expansion of a function we know that:

$$f(x+\Delta x) = f(x) + \Delta x f'(x) + \frac{(\Delta x)^2}{2} f''(x) + \cdots \quad (1)$$

and

$$f(x-\Delta x) = f(x) - \Delta x f'(x) + \frac{(\Delta x)^2}{2} f''(x) + \cdots \quad (2)$$

from ①, $f'(x)$ can be written as

$$f'(x) = \frac{f(x+\Delta x) - f(x)}{\Delta x} - \frac{(\Delta x)}{2} f''(x) + \cdots$$

So that one possible approximation for $f'(x)$ is:

$$f'(x) \approx \frac{f(x+\Delta x) - f(x)}{\Delta x} \quad \underbrace{[+ O(\Delta x)]}_{\text{error}} \quad (3)$$

another possible aproximation is, from ②

$$f'(x) \approx \frac{f(x) - f(x-\Delta x)}{\Delta x} \quad [+ O(\Delta x)] \quad (4)$$

and still another is, from ① and ②

$$f''(x) \approx \frac{f(x+\Delta x) - f(x-\Delta x)}{2\Delta x} \quad [+ O(\Delta x^2)] \quad (5)$$

one approximation for the second derivative is from ① and ②

$$f''(x) = \frac{f(x+\Delta x) + f(x-\Delta x) - 2f(x)}{(\Delta x)^2} \quad (6)$$

3, 4 and 5 are called the forward, backward and centered finite difference for $f'(x)$.

From a purely point of view of the error involved (Truncation error or accuracy of aproximation)

it seems obvious that (5) is best since it has a truncation error of only $O(\Delta x^2)$ while in (3) and (4) the error is of order (Δx). We will see that this is not always the case, it depends on the equation being solved.

Numerical Grid

Let's consider ϕ a function of space and time, $\phi = \phi(x,t)$, we can represent ϕ in a 2-D grid where $x = m\Delta x$ and $t = n\Delta t$

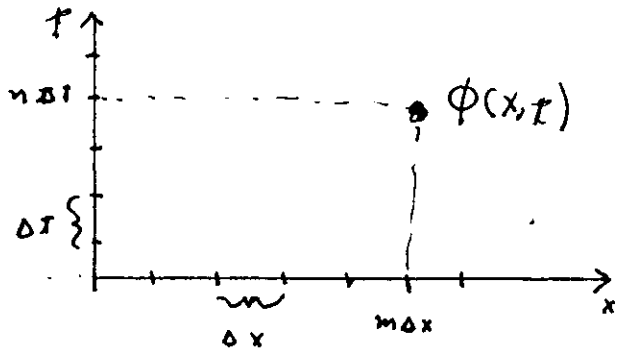

we write $\phi(x,t) = \phi(m\Delta x, n\Delta t) = \phi_m^n$

We can construct a finite difference equation by replacing the derivatives by finite differences. For example for the lineal friction equation.

$$\frac{\partial \phi}{\partial t} = -k\phi \qquad (7)$$

using the forward difference approximation ⑨ for the time derivative, we get

$$\frac{\phi(T+\Delta t, x) - \phi(T,x)}{\Delta T} = -k\,\phi(T,x)$$

or with the sub and superscript notation

$$\frac{\phi((n+1)\Delta t, m\Delta x) - \phi(n\Delta t, m\Delta x)}{\Delta t} = -k\,\phi(n\Delta t, m\Delta x)$$

or

$$\frac{\phi_m^{n+1} - \phi_m^n}{\Delta t} = -k\phi_m^n$$

so that we can estimate the valve of ϕ at the future time $n+1$ by the predictor equation

$$\phi_m^{n+1} = \phi_m^n - \Delta T k\,\phi_m^n = [1 - \Delta T K]\,\phi_m^n \qquad (8)$$

we estimate the future (advance in time) in terms of the present. Note that we have to solve one of these equations for each point in x (m)

Equation (8) is a recursion relationship, using $G = [1 - \Delta T K]$ in ⑧ we have.

$$\phi_m^{n+1} = G\,\phi_m^n$$

$$\phi_m^{n+1} = G[G\,\phi_m^{n-1}] = \cdots = G^n\,\phi_m^0$$

where ϕ_m^0 is the initial condition.

For the lineal friction equation ($k>0$) we know that the solution ϕ goes to zero has $t \to \infty$.

$$\phi \to 0 \qquad \text{as} \qquad t \to \infty \qquad (9)$$

for the numerical scheme (8) [Euler] we can see that in order to have any hope of finding a solution that satisfies (9), $|G|$ must be less than 1, ie.

$$\text{for} \quad \phi_m^{n+1} = G^n \phi_n^0 \longrightarrow 0 \quad \text{for} \quad n \to 0$$

$$\Rightarrow \quad |G| < 1$$

this places a limit on Δt, since

$$|G| = |1 - \Delta t\, k| < 1 \Longrightarrow \Delta t < \frac{2}{k}$$

For the 1-D <u>advection equation</u>

$$\frac{\partial \phi}{\partial t} = -A \frac{\partial \phi}{\partial x} \qquad (10)$$

if we use forward difference in time and centered in space we get

$$\frac{\phi_m^{n+1} - \phi_m^n}{\Delta t} = -A \left[\frac{\phi_{m+1}^n - \phi_{m-1}^n}{2\Delta x} \right]$$

so that the recursion relation is

$$\phi_m^{n+1} = \phi_m^n - \frac{A\Delta t}{2\Delta x}\left[\phi_{m+1}^n - \phi_{m-1}^n\right] \qquad (11)$$

using $a = \frac{A\Delta t}{\Delta x}$ and assuming

$$\phi_j^n = \Phi_n e^{ik_j\Delta x}$$

(considering a single wave number; $\phi(x,t) = \Phi(t)e^{ikx}$)

in (11) we get

$$\Phi_{n+1} e^{ik_j\Delta x} = \Phi_n e^{ik_j\Delta x} + \frac{a}{2}\left[\Phi_n e^{ik(m+1)\Delta x} - \Phi_n e^{ik(m-1)\Delta x}\right]$$

or dividing by $e^{ik_j\Delta x}$

$$\Phi_{n+1} = \Phi_n\left[1 + \frac{a}{2}\left(e^{ik\Delta x} - e^{-ik\Delta x}\right)\right]$$

$$\Phi_{n+1} = \left[1 + a\,i\cos(k\Delta x)\right]\Phi_n \qquad (12)$$

defining the amplification factor as

$$\Phi_{n+1} = G\,\Phi_n$$

in (12) after division by Φ_n we get

$$G = 1 + i\,a\cos(k\Delta x) \qquad (13)$$

For Φ_{n+1} to be bounded for large n it is required that $|G| \le 1$ but from (13)

we see that, for any $\Delta t > 0$, $|G| > 1$ so that this scheme; forward in time centered in space is always <u>unstable</u> for the advection equation.

Using centered difference in time and space in the advection equation, the amplification factor can be found to be (you can do it as an exercise)

$$G = ia \sin(k\Delta x) \pm (-a^2 \sin^2(k\Delta x) + 1)^{1/2}$$

if $a = \frac{A\Delta t}{\Delta x} \leq 1$ the radical is real and

$|G| = 1$, the scheme is neutral

$\frac{A\Delta t}{\Delta x} \leq 1$ is called the CFL condition.

Physically it states that information must propagate less than one Δx in one Δt for the scheme to be stable. It usually places the strongest limit on Δt; $\Delta t \leq \frac{\Delta x}{A}$.

If $\frac{A\Delta t}{\Delta x} > 1$, the most unstable wave is $4\Delta x$, the one that makes G larger [i.e. $\sin(k\Delta x) = 1$] or when $k\Delta x = \frac{\pi}{2}$, $k = \frac{2\pi}{4\Delta x}$. If the CFL condition is violated the wave that is going to grow faster is the one with wavelength $4\Delta x$.

the instability starts as numerical noise of size $4\Delta x$.

For the diffusion equation

$$\frac{\partial \phi}{\partial t} = K \frac{\partial^2 \phi}{\partial x^2}$$

using centered in time and space we get the scheme (using 6):

$$\frac{\phi_m^{n+1} - \phi_m^{n-1}}{2\Delta t} = K \left[\frac{\phi_{m+1}^n + \phi_{m-1}^n - 2\phi_m^n}{(\Delta x)^2} \right]$$

looking at the behavior of a single wave as before $\phi_j^n = \Phi_n e^{ikj\Delta x}$

after division by $e^{ikj\Delta x}$ we get

$$\frac{\Phi_{n+1} - \Phi_{n-1}}{2\Delta t} = \frac{K}{(\Delta x)^2} \left[e^{ik\Delta x} + e^{-ik\Delta x} - 2 \right] \Phi_n$$

or

$$\Phi_{n+1} = \Phi_{n-1} + \frac{4K\Delta t}{(\Delta x)^2} \left[\cos(k\Delta x) - 1 \right] \Phi_n$$

defining $\tilde{K} = \frac{K\Delta t}{(\Delta x)^2}$ and the amplification factor as $\Phi_{n+1} = G\Phi_n$, the equation for G becomes, after division by Φ_n

$$G - G^{-1} = 4\tilde{K} \left[\cos(k\Delta x) - 1 \right]$$

or

$$G^2 - 4\tilde{K}(\cos(\alpha)-1)G - 1 = 0 \qquad ; \alpha = k\Delta x$$

with roots $$G = 2\tilde{K}(\cos\alpha - 1) \pm \sqrt{4K^2(\cos\alpha-1)^2 + 1}$$

using $$\lambda = 2\tilde{K}(\cos\alpha - 1)$$

$$G = \lambda \pm \sqrt{\lambda^2 + 1}$$

So that $|G| > 1$ ∴ this scheme is <u>unconditionally unstable</u>

Using forward in time and centered in space for the diffusion equation, i.e.

$$\frac{\phi_m^{n+1} - \phi_m^n}{\Delta T} = K\left[\frac{\phi_{m+1}^n + \phi_{m-1}^n - 2\phi_m^n}{(\Delta x)^2}\right]$$

one can find that the equation for the amplification factor is:

$$G = 1 + \frac{2K\Delta T}{(\Delta x)^2}\left[\cos(k\Delta x) - 1\right]$$

so that the stability condition requires that

$$\frac{4K\Delta T}{(\Delta x)^2} \leq 2 \quad \text{or} \quad \Delta T \leq \frac{(\Delta x)^2}{2K}$$

and if this condition is not met, the most unstable wave is $k = \frac{2\pi}{2\Delta x}$ or the wave with wave length $2\Delta x$.

a summary of the above results is:

	$O(\Delta T)$ forward in time centered in space	$O(\Delta T^2)$ centered in time centered in space
Diffusion problems (friction)	stable (conditionally) $\Delta T < \frac{(\Delta x)^2}{2K}$ $MUW = 2\Delta x$	unstable
Advection problems (oscillatory)	unstable	stable (conditionally) $\Delta T < \frac{\Delta x}{A}$ $MUW = 4\Delta x$

One conclusion drawn from these results is that there is not such thing as the best scheme, it depends on the problem. Accuracy is not enough, the scheme has to be stable (or the other way around). Although a priori it looks like a scheme with an error of $O(\Delta T^2)$ is better than one with error of order $O(\Delta T)$, in the case of diffusion, for example, it is not, simply because it is not stable.

Ofcourse these two schemes are not the only ones possible. In fact it is easy to deduce that there are an infinite number of possibilities. Two other stable schemes of order $(\Delta T)^2$ that have been used for the diffusion problems are the so called lagged diffusion and the Dufort-Frankel method.

In the lagged diffusion the diffusion term is evaluated not at the "present" time (n) but at the previous time step (n-1), i.e.

$$\frac{\phi_m^{n+1} - \phi_m^{n-1}}{2\Delta t} = k\left[\frac{\phi_{m+1}^{n-1} + \phi_{m-1}^{n-1} - 2\phi_m^{n-1}}{(\Delta x)^2}\right]$$

it can be shown that this scheme is stable provided that $\Delta t \leq \frac{(\Delta x)^2}{4k}$.

If any other terms are involved in the equation, only the diffusion term is lagged in time, for example, for the equation:

$$\frac{\partial \phi}{\partial t} = f(\phi) + K\frac{\partial^2 \phi}{\partial x^2}$$

the scheme would be

$$\frac{\phi^{n+1} - \phi^{n-1}}{2\Delta t} = f\left[\phi^n\right] + k\left[\frac{\partial^2 \phi}{\partial x^2}\right]^{n-1}$$

For the Dufort-Frankel method the term in the middle of the space derivative is evaluated not at the time n but a an average between the previous and future time, i.e. instead of using

$$\frac{\phi_m^{n+1} - \phi_m^{n-1}}{2\Delta t} = K\left[\frac{\phi_{m+1}^{n} + \phi_{m-1}^{n} - 2\phi_m^{n}}{(\Delta x)^2}\right]$$

which is unstable, the term ϕ_m^n is substituted by $\frac{\phi_m^{n+1} + \phi^{n-1}}{2}$ to get

$$\frac{\phi^{n+1}_m - \phi^{n-1}_m}{2\Delta t} = K\left[\frac{\phi^n_{m+1} + \phi^n_{m-1} - 2\left[\frac{\phi^{n+1}_m - \phi^{n-1}_m}{2}\right]}{(\Delta x)^2}\right]$$

This is an implicit method that is allways stable, the ϕ^{n+1}_m Term in the RHS may be brought To the left to yield an explicit method. this method is widely used in Oceanography.

Computer exercise #1
Vertical diffusion in the sea

Solve numerically the following problem:

$$\frac{\partial \phi}{\partial t} = K \frac{\partial^2 \phi}{\partial z^2}$$

$$\phi = T_s \quad \text{at} \quad z = 0$$

$$\frac{\partial \phi}{\partial z} = 0 \quad \text{at} \quad z = D$$

$$\phi(x, 0) = T_o$$

The column of water has an initial Temperature (or concentration of a pollutant) of To, The Temperature at the surface is brought To Ts and maintained at That Temperature, there is no flux at the bottom.

the analytical solution for this problem is

$$\phi(x,t) = T_s - \frac{4(T_s - T_0)}{\pi} \sum_{n\geq 0} \frac{1}{(2n+1)} \exp(-k\lambda_n^2 t) \sin\left[(2n+1)\frac{\pi}{2}\frac{z}{D}\right]$$

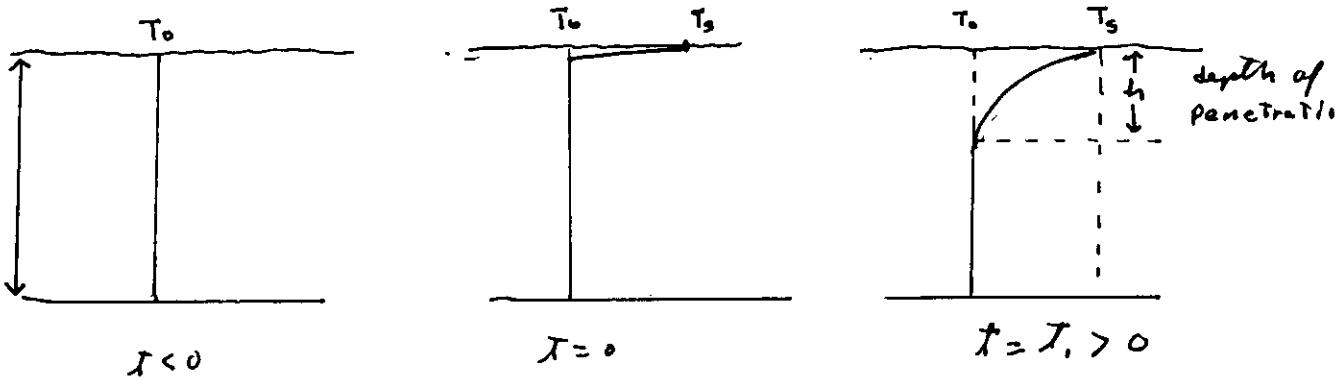

the program vertdif.f solves this problem by implementing the lagged scheme. i.e. centered difference for the time derivative and the diffusion term evaluated at time (n-1).

$$\frac{\phi_m^{n+1} - \phi_m^{n-1}}{2\Delta t} = K \frac{\left[\phi_{m+1}^{n-1} + \phi_{m-1}^{n-1} - 2\phi_m^{n-1}\right]}{(\Delta z)^2}$$

Note that the main loop is only one line, the rest is for reading in the parameters of the model (Δz, Δt, K, etc), initializing constants and variables and writting the results. One important point is that we do not keep ϕ for every time step. we keep only three levels; present, past and future. At the end of the program these levels are shuffled every time step.

Compile and run the program with the parameters given (in vertdif.in). Plot the evolution of the vertical profile.

1- Suppose the water depth is 20 m and $K_z = 0.001\ m^2/s$, use $\Delta z = 2$ m and run the model with the following time steps

a) $\Delta t = 90$ s b) $\Delta t = 900$ s c) $\Delta t = 1200$ s

Plot the vertical temperature profile for $T = 1, 2, 4, 12$. Compare with the analytical solution.

An important concept in this problem is the speed at which a tracer diffuses down from the surface. Suppose that h (the depth of penetration) can be written as

$$h \propto (Kt)^{1/2} \qquad (\text{or } h \propto K^a t^b)$$

so that $t = c_1 h^2/K$.

2- use the model to find c_1 by first finding the time it takes the signal to reach some depth h, do this for several depths ($h = 2\Delta z, 4\Delta z, 8\Delta z$) and find the slope of the graph t vs h^2/K. Choose some concentration to define when the signal has reached some depth, for example when it has increased 10% of the difference.

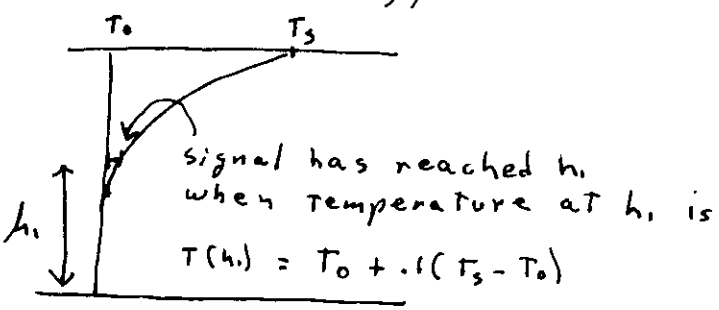

Compute the time it takes for complete vertical mixing; say the bottom concentration is 95% of the final (surface) concentration T_s.

3: At a site of a proposed coastal outfall, a dye experiment produces the following results

a) Dye released at the surface reached the bottom (depth of 15 m) after one hour.

b) The dye was completly mixed between the surface and the bottom after 12 hours

what is your best estimate of the vertical diffusivity (m^2/s).

```
      program vertdif
      dimension past(50),present(50),future(50)
      real kz,k1,k2
      integer out,out2
c
      in=20
      out=21
      out2=22
c     open input and output files
      open(unit=in, file='vertdif.in')
      open(unit=out,file='vertdif.out')
      open(unit=out2,file='vertdif.out2',form='unformatted')
c     read data
      read(in,*) dz
      read(in,*) depth
      read(in,*) dt
      read(in,*) kz
      read(in,*) nstep
      read(in,*) nans
      read(in,*) nevery
c
      np=int(depth/dz)
c
c     read initial temperature profile
c     and initialize temperature array
      do 100 i=1,np
      read(in,*) tinit
      past(i)=tinit
      present(i)=tinit
      future(i)=0.
  100 continue
c
      time=0.0
      c=2.*kz*dt/(dz*dz)
      k1=1.-c
      k2=1.+c
      print *,np,nevery
c     print out the model parameters
      write(out,900) dz,depth,dt,kz
  900 format(1x,'VERTICAL DIFFUSION:',//,'DZ (M) =',f5.2,/,
     1  ' DEPTH (M) =',f5.2,/,' DT (s) =',f6.1,/,
     1  ' KZ (M**2/s)=',f7.4,//)
c
c     print out the depths for wich temperatures are tabulated
      write (out,902) (0.5*dz+(i-1)*dz, i=1,np,nevery)
  902 format(1x,' DEPTHS (M):',//,1x,25f6.2,/)
c
c  start the main loop
c
      do 1000 l=1,nstep
      time=float(l-1)*dt
c
c    check for output
      if(mod(l,nans).eq.0) then
      write(out,910) time,time/3600.
  910 format(/,1x,'Time =',f9.1,' (s)',2x,f9.2,'  (hours)')
      write(out,920) (present(i),i=1,np,nevery)
  920 format(1x,25f6.2)
      write(out2) l,present
      endif
c
c     update temperatures
c     at the surface
      do 200 i=1,1
  200 future(i)=present(i)
c
c     interior point
      do 210 i=2,np-1
  210 future(i)=(k1/k2)*past(i)+ (c/k2)*(present(i+1)+present(i-1))
c
c     at the bottom
      do 220 i=np,np
  220 future(i)=present(i-1)
c
c   shuffle the time levels
      do 300 i=1,np
      past(i)=present(i)
  300 present(i)=future(i)
 1000 continue
      stop
      end
```

vertdif.in Mon Apr

```
1.0     dz
20.0    depth
20.0    dt
0.001   kz
21600   nstep
60      nans
1       nevery
15      initial profile
10
10
10
10
10
10
10
10
10
10
10
10
10
10
10
10
10
10
10
10
```

Computer exercise #2

A one-dimensional tidal model

Consider the simplest form of the equations: sectionally-averaged system with quadratic friction. The continuity and momentum equations can be written as:

$$\frac{\partial \eta}{\partial t} = -\frac{1}{B}\frac{\partial}{\partial x}(Au)$$

$$\frac{\partial u}{\partial t} = -g\frac{\partial \eta}{\partial x} - \frac{k\,u|u|}{(D+\eta)^{4/3}}$$

where $A = B(D+\eta)$

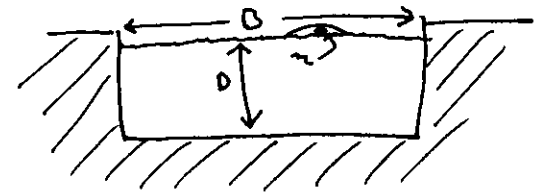

Program Tide.f implements this problem. The numerical scheme is centered in time with the friction term lagged. In space the variables are placed in a staggered grid of N elevation points and $N-1$ velocity points

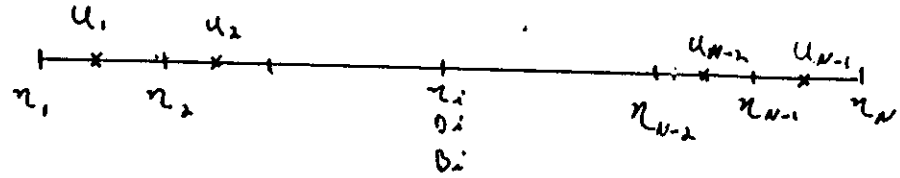

Staggered grid usually simplified the coding of a model and will introduce less numerical dissipation. The finite difference equations are

$$\frac{\eta_i^{n+1} - \eta_i^{n-1}}{2\Delta t} = -\frac{1}{B_i}\left\{\left[\frac{B_i(D_i+\eta_i^n) + B_{i+1}(D_{i+1}+\eta_{i+1}^n)}{2}\right]u_i - \left[\frac{B_{i-1}(D_{i-1}+\eta_{i-1}^n) + B_i(D_i+\eta_i^n)}{2}\right]u_{i-1}\right\}/\Delta x$$

$$\frac{u_i^{n+1} - u_i^{n-1}}{2\Delta T} = -g\left(\frac{\eta_{i+1}^{n} - \eta_i^{n}}{\Delta x}\right) \qquad (\text{at } T = n)$$

$$- \frac{K\, u_i^{n-1} |u_i^{n-1}|}{\left[\frac{(D_i + \eta_i^{n-1}) + (D_{i+1} + \eta_{i+1}^{n-1})}{2}\right]^{4/3}} \qquad (\text{at } T = n-1)$$

The following data, in Tide.dat, is required To run this model:

N	number of elevation points, points in x
Dx	grid size (m)
ΔT	Time step (s)
CD	bottom drag coefficient (K) $O(5\times10^{-3})$
H1, G1	amplitude (m) and phase (deg) of the
H2, G2	surface elevation at the end points of the model region.
D(I) $I=1,N$	water depth (m) at the elevation points.
B(I)	widths (m) at elevation points.

Run the model for five tidal cycles with the parameters given in tide.dat. Plot the elevation and velocities for the final cycle.

- where do you find the maximum speeds and why?
- Suppose that current measurements showed that The maximum current is 2.0 m/s, what would be a good estimate for the friction coefficient for The channel?
- Suppose a pollutant is Thrown into the middle of the channel. Write a numerical scheme

To predict the spreading of this pollutant ($c_z[\frac{mg}{m^3}]$), under the effect of diffusion and advection by the channel tidal velocities. i.e.

$$\frac{\partial c}{\partial t} = -u\frac{\partial c}{\partial x} + K_x\frac{\partial^2 c}{\partial x^2} + q$$

- Incorporate this equation into the tidal model.
- Suppose a constant inflow of pollutant of

$$q = \frac{.01}{\Delta t}\ \frac{m_3}{m^2 s}$$

is added at the middle of the channel. Use the model to estimate the time it takes for the concentration to reach, say $50\ \frac{mg}{m^3}$ at the left end of the channel if the diffusion coefficient $K_x = 300\ m^2/s$. (use the same parameter given in tide.dat, eg. $\Delta x = 950m$, $N = 100$, etc)

- Program tide.f is written so that both ends of the channel are forced by external functions derived from observations [H1, G1, H2, G2]. Suppose that the channel is closed at the right end. Change the program to represent this condition, i.e no flux at the right boundary.

```
c
c       simple tidal model
c
      common /c1/ eta(100,3), u(100,3), d(100), b(100)
      common /c2/ n, nm1, dt, dx, cd, ntc, tc, tim, h1,
     1  g1, hn, gn, pi, g, iout,iout2
      open (unit=20, file='tide.dat2')
      read (20, *) iout
      read (20, *) iout2
      print *,iout,iout2
      open (unit=iout, file='tide.out')
      open (unit=iout2, file='tide.nft',form='unformatted')
      read (20, *) n
      read (20, *) dx
      read (20, *) dt
      read (20, *) nloop
      read (20, *) nans
      read (20, *) start
      read (20, *) cd
      read (20, *) h1, g1
      read (20, *) hn, gn
      read (20, *) (d (i), i=1, n)
      read (20, *) (b (i), i=1, n)
      print *,iout,n,dx,dt,nloop,nans,start,cd
      print *,h1,g1,hn,gn
      print *,d
      print *,b
      g=9.81
      pi=4.*atan(1.)
      ntc=int (12.4224*3600./dt+0.00001)
      nm1=n-1
      call init
c
      do 100 ll=1, nloop
      t=float (ll) *dt
      tim=t/3600.
      tc=tim/12.4224
      call bc
      call elv
      call vel
      call asselin
      call shuffle
      if (tc.ge.start .and. mod(ll,nans) .eq.0) call output
100   continue
c
      stop
      end
      subroutine init
      common /c1/ eta(100,3), u(100,3), d(100), b(100)
      common /c2/ n, nm1, dt, dx, cd, ntc, tc, tim, h1,
     1   g1, hn, gn, pi, g, iout,iout2
      e1=h1*cos(-g1*pi/180.)
      en=hn*cos(-gn*pi/180.)
      do 100 i=2, nm1
      do 100 j=1, 2
100   eta(i,j)=e1+(en-e1)*float(i-1)/float (nm1)
      do 200 i=1, nm1
      do 200 j=1, 2
200   u(i,j)=0.
      return
      end
      subroutine bc
      common /c1/ eta(100,3), u(100,3), d(100), b(100)
      common /c2/ n, nm1, dt, dx, cd, ntc, tc, tim, h1,
     1   g1, hn, gn, pi, g, iout,iout2
      eta(1,3)=h1*cos(2.*pi*tc-g1*pi/180.)
      eta(n,3)=hn*cos(2.*pi*tc-gn*pi/180.)
      return
      end
      subroutine elv
      common /c1/ eta(100,3), u(100,3), d(100), b(100)
      common /c2/ n, nm1, dt, dx, cd, ntc, tc, tim, h1,
     1   g1, hn, gn, pi, g, iout,iout2
      c=dt/dx
      do 100 i=2, nm1
100   eta(i,3)=eta(i,1)-c*((b(i)*(d(i)+eta(i,2))+b(i+1)*
     $(d(i+1)+eta(i+1,2)))*u(i,2)-(b(i-1)*(d(i-1)+eta(i-1,2))
     $+b(i)*(d(i)+eta(i,2)))*u(i-1,2))/b(i)
      return
      end
      subroutine vel
      common /c1/ eta(100,3), u(100,3), d(100), b(100)
      common /c2/ n, nm1, dt, dx, cd, ntc, tc, tim, h1,
     1  g1, hn, gn, pi, g, iout,iout2
      do 100 i=1, nm1
      db1=-g*(eta(i+1,2)-eta(i,2))/dx
      db2=-cd*(u(i,1)*abs(u(i,1)))/
     $  ((0.5*(d(i)+eta(i,1)+d(i+1)+eta(i+1,1)))**(4./3.))
100   u(i,3)=u(i,1)+2.*dt*(db1+db2)
      return
      end
      subroutine asselin
      common /c1/ eta(100,3), u(100,3), d(100), b(100)
      common /c2/ n, nm1, dt, dx, cd, ntc, tc, tim, h1,
     1 g1, hn, gn, pi, g, iout,iout2
      r=0.05
      do 100 i=1,n
100   eta (i,2)=eta(i,2)+0.5*r*(eta(i,1)-2.*eta(i,2)+eta(i,3))
      do 200 i=1,nm1
200   u(i,2)=u(i,2)+0.5*r*(u(i,1)-2.*u(i,2)+u(i,3))
      return
      end
      subroutine shuffle
      common /c1/ eta(100,3), u(100,3), d(100), b(100)
      common /c2/ n, nm1, dt, dx, cd, ntc, tc, tim, h1,
     1  g1, hn, gn, pi, g, iout,iout2
      do 100 i=1,n
      eta (i,1)=eta(i,2)
100   eta (i,2)=eta(i,3)
      do 200 i=1,nm1
      u(i,1)=u(i,2)
200   u(i,2)=u(i,3)
      return
      end
      subroutine output
      common /c1/ eta(100,3), u(100,3), d(100), b(100)
      common /c2/ n, nm1, dt, dx, cd, ntc, tc, tim, h1,
     1   g1, hn, gn, pi, g, iout,iout2
      write(iout,900) tim,tc
900   format(1x,'time =',f7.2,'(hours)',10x,f7.2,'(t.c.)')
      write(iout,910) (eta(i,2),i=1,n)
      write(iout,920) (u(i,2),i=1,nm1)
      write(iout2) tim,(u(i,2),i=1,nm1)
      write(iout2) tim,(eta(i,2),i=1,n)
910   format(1x,20f6.2)
920   format(4x,20f6.2)
      return
      end
```

tide.dat2 **Mon Apr 14 11:01:43 1997**

```
21              iout  (formatted output)
22              iout2 (unformatted output)
100             n
950             dx
29.81376        dt (s) T/1500
33000           nloop
300             nans
1.              start
0.005           cd
1.61,292        h1,g1 (m,deg)
1.71,302        hn,gn
9.5   9.8 10.1 10.4 10.7 11.0 11.3 11.6 11.9 12.2
12.5  12.75 13.0 13.25 13.5 13.75 14.0 14.25 14.5 14.75
15  14. 13. 12. 11. 10. 9. 8. 7. 6.
5  5.4 5.8 6.2 6.6 7.0 7.4 7.8 8.2 8.6
9   9 9 9 9 9 9 9 9
9   9.6 10.2 10.8 11.4 12.0 12.6 13.2 13.8 14.4
15  14.8 14.6 14.4 14.2 14.0 13.8 13.6 13.4 13.2
13  12.9 12.8 12.7 12.6 12.5 12.4 12.3 12.2 12.1
12  11.9 11.8 11.7 11.6 11.5 11.4 11.3 11.2 11.1
11  10.9 10.8 10.7 10.6 10.5 10.4 10.3 10.2 10.1
1200 1200 1200 1200 1200 1200 1200 1200 1200 1200
1200 1170 1140 1110 1080 1050 1020 990 960 930
900 900 900 900 900 900 900 900 900 900
900 890 880 870 860 850 840 830 820 810
800 810 820 830 840 850 860 870 880 890
900 885 870 855 840 825 810 795 780 765
750 725 700 675 650 625 600 575 550 525
500 480 460 440 420 400 380 360 340 320
300 300 300 300 300 300 300 300 300 300
300 300 300 300 300 300 300 300 300 300
```

Computer exercise #3

Topographic waves

Small bottom irregularities can turn an otherwise steady geostrophic flow into slowly moving waves. Let's look at the dynamics of an ocean with bottom slope. For simplicity let's look at an homogeneous ocean and let's the domain be a channel with periodic boundaries in y, and a weak and uniform bottom slope in the x direction as shown in the figure.

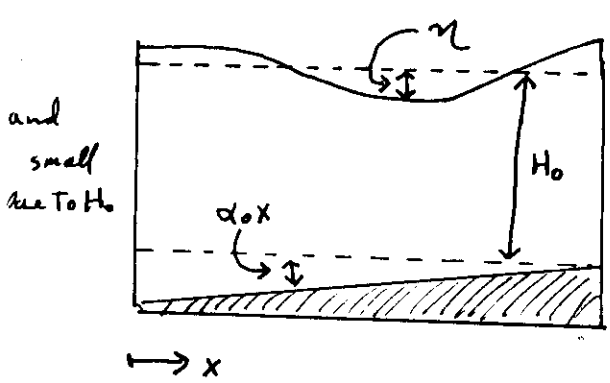

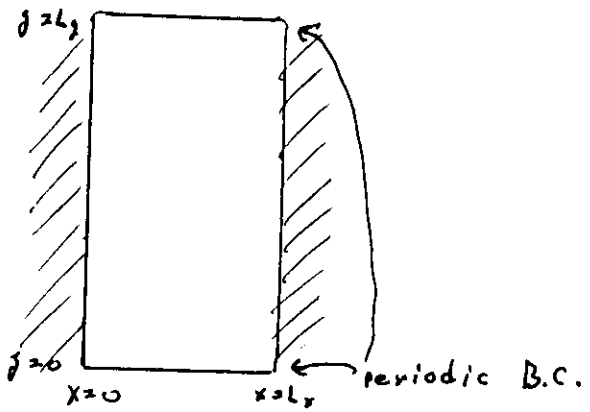

starting with the vertically integrated continuity equation

$$\frac{\partial h}{\partial t} + \frac{\partial}{\partial x}(hu) + \frac{\partial}{\partial y}(hv) = 0 \qquad (14)$$

Substitution of $h(x,y,t) = H_0 - \alpha x + \eta(x,y,t)$ in (14) gives

$$\frac{\partial \eta}{\partial t} + \left(u\frac{\partial \eta}{\partial x} + v\frac{\partial \eta}{\partial y}\right) + (H_0 - \alpha x + \eta)\left[\frac{\partial u}{\partial x} + \frac{\partial v}{\partial y}\right] - \alpha_0 u = 0$$

for linear theory and requiring a gentle slope

allows us to write the continuity equation as

$$\frac{\partial \eta}{\partial t} + H_0\left[\frac{\partial u}{\partial x} + \frac{\partial v}{\partial y}\right] - \alpha_0 u = 0 \qquad (15)$$

the corresponding linear, vertically integrated momentum equations are:

$$\frac{\partial u}{\partial t} - fv = -g\frac{\partial \eta}{\partial x} \qquad (16)$$

$$\frac{\partial v}{\partial t} + fu = -g\frac{\partial \eta}{\partial y} \qquad (17)$$

The extra term $\alpha_0 u$ in the continuity equation, related to the bottom slope will allow the existence of slow waves similar to the planetary waves due to the variation of the coriolis parameter.

This system contains both small and large terms. The large ones (Terms including f, g and H_0) comprise the otherwise steady geostrophic dynamics. In the presence of the small Term $\alpha_0 u$ the time derivatives came into play, but are still expected to be small. Capitalizing in this smallness we can take as a first approximation the geostrophic balance

$$u \approx -\left(\frac{g}{f}\right)\frac{\partial \eta}{\partial y} \quad ; \quad v \approx \left(\frac{g}{f}\right)\frac{\partial \eta}{\partial x} \qquad (18)$$

Substitution of (18) in the small time derivatives of (16)-(17), yields to the next level of approximation

$$u = -\frac{g}{f}\frac{\partial \eta}{\partial y} - \frac{g}{f^2}\frac{\partial^2 \eta}{\partial x \partial t}$$

$$v = +\frac{g}{f}\frac{\partial \eta}{\partial x} - \frac{g}{f^2}\frac{\partial^2 \eta}{\partial x \partial t}$$

replacement of the component in the continuity equation (15), provides a single equation for η, which to the leading order is:

$$\frac{\partial \eta}{\partial t} - R^2 \frac{\partial}{\partial t} \nabla^2 \eta + \frac{\alpha_0 g}{f} \frac{\partial \eta}{\partial y} = 0 \qquad (19)$$

where $R = \frac{\sqrt{g H_0}}{f}$.

A wave solution of the type $\cos(lx + my - \omega t)$ provides a dispersion relation:

$$\omega = \frac{\alpha_0 g}{f} \frac{m}{(1 + R^2(l^2 + m^2))} \qquad (20)$$

we note that if the additional ingredient, the bottom slope α_0, had not been present the flow would be steady and geostrophic. Because this waves own their existence to the bottom slope, These waves are called Topographic waves.

Program Topo.f implements the system (15)-(17) in a channel with periodic boundaries in $y = 0$ and $y = L_y$.

the numerical scheme is leap frog in time placed in a 2-D staggered grid (Arakawa C-grid) as follows

$v_{j,k+1}$

$u_{j-1,k}$ h_{jk} u_{jk}

v_{jk}

the complete scheme is as follows:

for the u equation (centered at $u_{j,k}$)

$$\frac{u_{j,k}^{n+1} - u_{j,k}^{n-1}}{2\Delta T} = f\left[\frac{v_{j,k+1}^{n} + v_{j+1,k+1}^{n} + v_{j,k}^{n} + v_{j+1,k}^{n}}{4}\right]$$

$$- g\left[\frac{\eta_{j+1,k} - \eta_{j-1,k}}{2\Delta x}\right]$$

for the v equation (centered at $v_{j,k}$)

$$\frac{v_{j,k}^{n+1} - v_{j,k}^{n-1}}{2\Delta T} = -f\left[\frac{u_{j-1,k}^{n} + u_{j,k}^{n} + u_{j-1,k-1}^{n} + u_{j,k-1}^{n}}{4}\right]$$

$$- g\left[\frac{\eta_{j,k}^{n} - \eta_{j,k-1}^{n}}{2\Delta y}\right]$$

for the η equation (centered at $\eta_{j,k}$).

the boundary conditions are periodic at $y = 0$ and $y = L_y$, and non-slip condition at the walls $x = 0$ and $x = L_y$. these latter is implemented by updating at every time step the tangential velocities inside the boundaries to a value equal to the negative of the velocity at the point immediatly outside the boundary

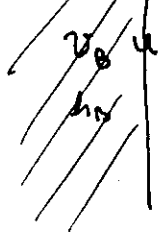

$u_B = 0$

$v_B = -v_{B+1}$

The shuffling of the time levels is done by changing the indices not the variables it solves, ie.

```
nsave= nT1
nT1  = nT2
nT2  = nsave
```

The equations in the program include a forcing term (wind) to start the currents. The wind is shut down after one day.

Compile and run the program topo.f with the parameters given. Some of the parameters of the model are as follows:

$\Delta T = 30$ (s)

$imax = 40$

$jmax = 20$

$\frac{\Delta X}{2} = \frac{\Delta Y}{2} = 5$ km ($L_y = 400$ km, $L_x = 200$ km)

$H_0 = 100$ m

$\tau = 0.0001$

$N^2 = 2$

$\tau^x = 0$

$$\tau^y = \begin{cases} \tau \sin\left(\frac{2\pi t}{N^2 y}\right) & T \le 1 \text{ day} \\ 0 & T > 1 \text{ day} \end{cases}$$

"$\alpha = 0$"

Run the model for a few days (5-10) and make contour plots of u, v and η for the last couple of days (every 1/4 days say). Describe the results.

Now change the bottom slope to $\alpha = 1 \times 10^{-3}$ and run the same as before. Describe the results. Make a x-y plot (Hoffmüller diagram) to estimate the speed of propagation. Compare to the analytical speed given by (20)

Change N^3 to 4 keeping the same α and repeat the experiment. Does the speed of propagation change? How?

```
c    barotropic model
c
      parameter(jjmax=20,kkmax=40)
c
      dimension h1(jjmax,kkmax,2),u1(jjmax,kkmax,2),v1(jjmax,kkmax,2)
      dimension tx(jjmax,kkmax),ty(jjmax,kkmax)
      dimension tem5(jjmax,kkmax)
c
c    open files
c
      open(43,file='utopo',form='unformatted')
      open(45,file='vtopo',form='unformatted')
      open(47,file='htopo',form='unformatted')
c
c    all quantities are in mks units
c  time step:
      delt=30.0
c  mesh spacing x  direction:
      delx= 5000.0
c  mesh spacing in y direction:
      dely= 5000.0
c  seconds per day
      secday=86400.0
c  # intervals in one day
      ndt1dy=secday/delt
c  day 2
      iday1=1*ndt1dy
      iday2=2*ndt1dy
      iday3=3*ndt1dy
c  last day of integration:
      daymax=15.
c   first day for writing results
      ndayini=1.
      nndyini=ndayini*ndt1dy
c  number of time steps between forward differences
      nstep=99
      pi=4.*atan(1.)
c
c  initialize all parameters
c  beginning iteration level:
      nnow=1
      nt1=1
      nt2=2
c
c  initialize internal parameters
c
c  value of gravity:
      g=10.0
c  earth's rotation rate:
      f=1.0e-4
c  number of time steps between writes:
      nwrite=.25*float(ndt1dy)
c  coefficient of bottom friccion
      r=.0003
      r=.0000
c   topography
      alfa=1.e-3
      alfa=0.0
c  wind
      tau=.0001
c   mean depth
      h0=100.
c
      jmax=jjmax
      kmax=kkmax
      kmaxm1=kmax-1
      jmaxm1=jmax-1
      kmaxm2=kmax-2
      jmaxm2=jmax-2
      jmaxm3=jmax-3
c  initialize u,v,h arrays:
      do k=1,kmax
      do j=1,jmax
      u1(j,k,1)=0.0
      v1(j,k,1)=0.0
      h1(j,k,1)=0.0
      u1(j,k,2)=0.0
      v1(j,k,2)=0.0
      h1(j,k,2)=0.0
      enddo
      enddo
c
c initialize constants outside n (time) loop
c
c  maximum iteration number:
      nmax=daymax*secday/delt +1
c
      w3=f/4.
      w6=g/(2.*delx)
      w9=f/4.
      w12=g/(2.*dely)
      w13=h0/(2.*delx)
      w14=h0/(2.*dely)
      w15=alfa*.5
      rr=r*2.
c
c  begin time loop
c
      do 400 n=nnow,nmax
c
c                toggle relevant descriptors each time step to
c                point to 1st or 2nd planes of u, v and h
c                also set up forward differences on the first and
c                every nstep-th time step thereafter else set up
c                centered differences
c
c flip time indices
c
      if(mod(n,ndt1dy).eq.1) print *,n
      nsave=nt1
      nt1=nt2
      nt2=nsave
c
c for start-up and for every nstep-th time step use forward difference
c
      if (mod(n,nstep).eq.1) then
         nt=nt2
         z5=delt
      else
c use centered time differences
         nt=nt1
         z5=2.*delt
      end if
c
c                 lhs of equations on plane nt1
c                 and rhs terms mostly on plane nt2
c                choose  centered or forward differences
c                 reflect boundary points at plane nt1
```

```
c
c
c
      if(n.gt.iday1) tau=0.0
      do k=1,kmax
      do j=1,jmax
         ty(j,k)=0.0
c        ty(j,k)=tau
         tx(j,k)=tau*sin((2.*pi*float(k))/(0.5*float(kmax)) )
      enddo
      enddo

c
c
c        ul equation
c
      do k=2,kmaxm1
      do j=3,jmaxm3
        ul(j,k,nt1)=ul(j,k,nt)+z5*(
c
     3       tx(j,k)

     2  + w3*(v1(j,k+1,nt2)+v1(j+1,k+1,nt2)
     2       +v1(j,k,nt2)  +v1(j+1,k  ,nt2))

     4  -rr*ul(j,k,nt2)

     5    -w6*(h1(j+1,k,nt2)-h1(j  ,k,nt2))
     9   )
      enddo
      enddo
c
c  implement periodic boundary condition for u at k=1
c
      do j=3,jmaxm3
            ul(j,1,nt1)=ul(j,1,nt)+z5*(
     3      tx(j,1)

     2  + w3*(v1(j,2,nt2)+v1(j+1,2,nt2)
     2       +v1(j,1,nt2)+v1(j+1,1,nt2))

     4  -rr*ul(j,1,nt2)

     5    -w6*(h1(j+1,1,nt2)-h1(j,1,nt2))
     9  )
      enddo
c
c  implement periodic boundary condition at for u k=kmax
c
      do j=3,jmaxm3
            ul(j,kmax,nt1)=ul(j,kmax,nt)+z5*(
     3      tx(j,kmax)

     2  + w3*(v1(j,1    ,nt2)+v1(j+1  ,1    ,nt2)
     2       +v1(j,kmax,nt2)  +v1(j+1,kmax,nt2))

     4  -rr*ul(j,kmax,nt2)

     5    -w6*(h1(j+1,kmax,nt2)-h1(j,kmax,nt2))
     9   )
      enddo
c
c           v1 equation
c
      do k=2,kmaxm1
      do j=3,jmaxm2
       v1(j,k,nt1)=v1(j,k,nt)+z5*(
c
     3  ty(j,k)

     2   -w9    *(u1(j   ,k,nt2)+u1(j   ,k-1,nt2)
     2           +u1(j-1,k,nt2)+u1(j-1,k-1,nt2))

     4  -rr*v1(j,k,nt2)

     5       -w12*(h1(j,k,nt2)-h1(j,k-1,nt2))

     9    )
      enddo
      enddo
c implement periodic boundary condition for v at k=1
c
      do j=3,jmaxm2
        v1(j,1,nt1)=v1(j,1,nt)+z5*(
     3       ty(j,1)

     2   -w9    *(u1(j   ,1,nt2)+u1(j   ,kmax,nt2)
     2           +u1(j-1,1,nt2)+u1(j-1,kmax,nt2))

     4  -rr*v1(j,1,nt2)

     5    -w12*(h1(j,1,nt2)-h1(j,kmax,nt2))
     9   )
      enddo
c  implement periodic boundary condition for v at k=kmax
c
      do j=3,jmaxm2
       v1(j,kmax,nt1)=v1(j,kmax,nt)+z5*(
c
     3      ty(j,kmax)

     2   -w9    *(u1(j   ,kmax,nt2)+u1(j   ,kmaxm1,nt2)
     2           +u1(j-1,kmax,nt2)+u1(j-1,kmaxm1,nt2))

     4  -rr*v1(j,kmax,nt2)

     5    -w12*(h1(j,kmax,nt2)-h1(j,kmaxm1,nt2))

     9   )
      enddo
c
c      h1 equation
c
      do k=2,kmaxm1
      do j=3,jmaxm2
       h1(j,k,nt1)= h1(j,k,nt)+z5*(
c
     1   -w13*(u1(j,k  ,nt2)-u1(j-1,k,nt2))
     1   -w14*(v1(j,k+1,nt2)-v1(j,k  ,nt2))

     2   +w15*(u1(j-1,k,nt2)+u1(j,k,nt2))
     9  )
      enddo
      enddo
c  implement periodic boundary for h at k=1
      do j=3,jmaxm2
       h1(j,1,nt1)= h1(j,1,nt)+z5*(
```

```
c
     1   -w13*(u1(j,1  ,nt2)-u1(j-1,1,nt2))
     1   -w14*(v1(j,2,nt2)-v1(j,1  ,nt2))

     2   +w15*(u1(j-1,1,nt2)+u1(j,1,nt2))
     9  )
      enddo
c  implement periodic boundary for h at k=kmax
      do j=3,jmaxm2
       h1(j,kmax,nt1)= h1(j,kmax,nt)+z5*(
c
     1   -w13*(u1(j,kmax  ,nt2)-u1(j-1,kmax,nt2))
     1   -w14*(v1(j,1,nt2)-v1(j,kmax  ,nt2))

     2   +w15*(u1(j-1,kmax,nt2)+u1(j,kmax,nt2))
     9  )
      enddo
c
c  boundary conditions at the walls
      do k=1,kmax
c      v1(2,k,nt1)=-v1(3,k,nt1)
c      v1(jmaxm1,k,nt1)=-v1(jmaxm2,k,nt1)
       v1(2,k,nt1)= v1(3,k,nt1)
       v1(jmaxm1,k,nt1)= v1(jmaxm2,k,nt1)
      enddo
c


c
c if "saving" this level, write out one level
c
c     if(n.ge.nndyini) then
      if (mod(n,nwrite).eq.0) then
      tim=float(n)/float(ndtldy)
      grad=h1(15,20,nt1)-h1(5,20,nt1)
      print *,'va a escribir',n,tim,
     1   u1(10,20,nt1),v1(10,20,nt1),grad
      nprint=nt1
c
      do k=1,kmax
      do j=1,jmax
      tem5(j,k)=u1(j,k,nprint)
      enddo
      enddo
      write(43) n,((tem5(j,k),j=1,jmax),k=1,kmax)


      do k=1,kmax
      do j=1,jmax
      tem5(j,k)=v1(j,k,nprint)
      enddo
      enddo
      write(45) n,((tem5(j,k),j=1,jmax),k=1,kmax)

      do k=1,kmax
      do j=1,jmax
      tem5(j,k)=h1(j,k,nprint)
      enddo
      enddo
      write(47) n,((tem5(j,k),j=1,jmax),k=1,kmax)
c
      end if
c     endif
c
c advance timestep
c
  400 continue
c
      stop 'after end'
      end
```

Computer exercise # 4

This is a variant of exercise #3. The domain of the model is the same, but changes in the topography are not small. The equations solved in program bumps.f are the following:

$$\frac{\partial U}{\partial t} + \frac{\partial}{\partial x}\left(\frac{U^2}{H}\right) + \frac{\partial}{\partial y}\left(\frac{UV}{H}\right) - fV = -gH\frac{\partial \eta}{\partial x} + \tau^x - \frac{rU}{H} + A\nabla^2 U$$

$$\frac{\partial V}{\partial t} + \frac{\partial}{\partial y}\left(\frac{UV}{H}\right) + \frac{\partial}{\partial y}\left(\frac{V^2}{H}\right) + fU = -gH\frac{\partial \eta}{\partial y} + \tau^y - \frac{rV}{H} + A\nabla^2 V$$

$$\frac{\partial \eta}{\partial t} + \frac{\partial U}{\partial x} + \frac{\partial V}{\partial y} = 0$$

where U and V are the integrated transports. The topography decays exponentially with -x and can have small bumps in y, the equation for the topography is:

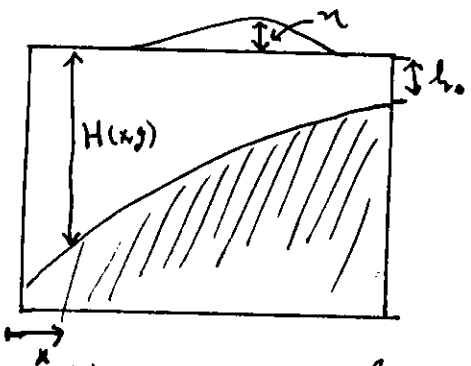

$$H(x,y) = h_0 \exp\left[\alpha x + \gamma \operatorname{sen}\left(\frac{\pi x}{L^x}\right) \operatorname{sen}\left(\frac{2\pi y}{N^y L^y}\right)\right]$$

The numerical scheme is the same as before, i.e. leap-frog with the friction and diffusion terms lagged in time. In order to simplify the results and for faster running the non-linear and friction terms have been commented out of the program (you can de-comment them latter to check their influence).

Topographic waves can also be generated by the y variation in topography. To check first that everything is set up correctly set the parameter that controls the "y" variation of topography (γ) equal to zero and run the program with an homogeneous wind of the form $\begin{cases} \tau^x = 0 \\ \tau^y = \tau \end{cases}$ with $\tau = \begin{cases} 0.002 & t < 1\,\text{day} \\ 0 & t > 1\,\text{day} \end{cases}$

this is done in the line "if (n.GT.ndT1dy) $\tau = 0^N$.
plot the u, v and h fields after a few days. You should get an eternal (no friction, $r=0$) current to the north in geostrophic balance.

Repeat experiment #3, i.e. run the model for a few days (5-10) with a wind that shuts down after one day and has a y-variation of two or four waves. You should get, just as in example #3, a topographic wave that propagates toward positive y (with the shallow water to its right).

Now setting the "bumps" parameter γ to $\gamma = .130$, $N^2 = 2$ (make a contour plot of H to check that the bathymetry is correct) force the model with a wind that shuts down after one day but homogeneous in space, i.e.

$$\tau^y = 0 \quad ; \quad \tau^x = \begin{cases} \tau & t \le 1\,\text{day} \\ 0 & t > 1\,\text{day} \end{cases}$$

this setting of parameters are implemented in the program bumps2.f (hopefully).

Plot the cotour plots of u, v and h fields and current (arrows) for a few days, every 1/4 of a day, say.

Describe the results. How do they differ with respect to experiment #3? Is it there an increase in velocity toward the "coast"? why? How do these results change if you include the non-linear terms? bottom friction? viscosity?

I suppose you can analyse with this model the effect of topographic drag on the current. For example, forcing the bump-less model with a time varying wind of the form $\tau^y = A \sin(\frac{2\pi t}{T})$ with a period of a few days probably produces no net residual circulation (when averaged over one period). The prefered direction of propagation of the topographic waves produced by the bumps, with the non-linear terms and bottom friction included (with the right parameters; size of bumps, friction and strength of currents) should produce a net residual circulation due to the bottom drag. Try playing with these parameters. For real fun try (or at least think about it) To incorporate an advection diffusion equation for a contaminant in the model.

```
c    barotropic model
c
      parameter(jjmax=20,kkmax=40)
      dimension h1(jjmax,kkmax,2),u1(jjmax,kkmax,2),v1(jjmax,kkmax,2),
     + hh(jjmax,kkmax)
      dimension tx(jjmax,kkmax),ty(jjmax,kkmax)
      dimension tem5(jjmax,kkmax)
c
c    open files
c
      open(43,file='ubumpc',form='unformatted')
      open(45,file='vbumpc',form='unformatted')
      open(47,file='hbumpc',form='unformatted')
      open(53,file='hh',form='unformatted')
c
c    all quantities are in mks units
c  time step:
      delt=30.0
c  mesh spacing x  direction:
      delx= 10000.0
c  mesh spacing in y direction:
      dely= 10000.0
c  seconds per day
      secday=86400.0
c  # intervals in one day
      ndt1dy=secday/delt
c  day 1
      iday1=1*ndt1dy
c  last day of integration:
      daymax=15.
c   first day for writing results
      ndayini=1.
      nndyini=ndayini*ndt1dy
c  number of time steps between forward differences
      nstep=99
      pi=4.*atan(1.)
c
c  initialize all parameters
c  beginning iteration level:
      nnow=1
      nt1=1
      nt2=2
c
c  initialize internal parameters
c
c  value of gravity:
      g=10.0
c  Coriolis parameter:
      f=1.0e-4
c  number of time steps between writes:
      nwrite=.25*float(ndt1dy)
c  coefficient of eddy viscocity:
      avisc=300.
c  coefficient of bottom friccion
c     r=.0001
      r=.000
c    bump size (topography in y)
c     gama=.130
      gama=0.0
c  e-folding for topography
      alfa=1.9e-5
c     alfa=0.0
      tau=.002
c
      jmax=jjmax
      kmax=kkmax
      jmaxs2=jjmax/2
      kmaxs2=kkmax/2
      kmaxm1=kmax-1
      jmaxm1=jmax-1
      kmaxm2=kmax-2
      jmaxm2=jmax-2
      jmaxm3=jmax-3
c  initialize u,v,h arrays:
      do k=1,kmax
      do j=1,jmax
      u1(j,k,1)=0.0
      v1(j,k,1)=0.0
      h1(j,k,1)=0.0
      u1(j,k,1)=0.0
      v1(j,k,1)=0.0
      h1(j,k,1)=0.0
      enddo
      enddo
cc
cc
      do k=1,kmax
      do j=1,jmax
       hh(j,k)=20.*exp((alfa*float(jmax-j)*delx)+
     1 sin(2.*pi*float(j)/(2.*float(jmax)))*
     1 sin(2.*pi*float(j)/(2.*float(jmax)))*
     2  gama*sin(2.*pi*float(k)/(.5*float(kmax))))
      enddo
      enddo
      write(53) 1,hh
      close(53)

c
c initialize constants outside n (time) loop
c
c  maximum iteration number:
      nmax=daymax*secday/delt +1
c
      w1=1./(8.*delx)
      w2=1./(2.*dely)
      w3=f/4.
      w4=avisc/(delx*delx)
      w5=avisc/(dely*dely)
      w6=g/(4*delx)
      w7=1./(8.*dely)
      w8=1./(2.*delx)
      w9=f/4.
      w10=avisc/(delx*delx)
      w11=avisc/(dely*dely)
      w12=g/(4.*dely)
      w13=1./(2.*delx)
      w14=1./(2.*dely)
      rr=r*2.
c load wind values (tx,ty)
c      do k=1,kmax
c      do j=1,jmax
c      tx(j,k)=.0
c      ty(j,k)=tau
c      enddo
c      enddo
c
c  begin time loop
c
```

```
      do 400 n=nnow,nmax
c
c                 toggle relevant descriptors each time step to
c                 point to 1st or 2nd planes of u, v and h
c                 also set up forward differences on the first and
c                 every nstep-th time step thereafter else set up
c                 centered differences
c
c flip time indices
c
      if(mod(n,ndtldy).eq.1) print *,n
      nsave=nt1
      nt1=nt2
      nt2=nsave
c
c for start-up and for every nstep-th time step use forward difference
c
      if (mod(n,nstep).eq.1) then
         nt=nt2
         z5=delt
      else
c use centered time differences
         nt=nt1
         z5=2.*delt
      end if
c
c                  lhs of equations on plane nt1
c                  and rhs terms mostly on plane nt2
c                 choose  centered or forward differences
c                  reflect boundary points at plane nt1
c
c
      if(n.gt.iday1) tau=0.0
      do k=1,kmax
      do j=1,jmax
         tx(j,k)=0.0
c        ty(j,k)=tau
         tx(j,k)=tau*sin(2*pi*float(k)/(.5*float(kmax)) )
      enddo
      enddo
c
c
c
c        ul equation
c
      do k=2,kmaxm1
      do j=3,jmaxm3
        ul(j,k,nt1)=ul(j,k,nt)+z5*(
c
     3       tx(j,k)
     -    -wl*( ((ul(j+1,k,nt2)+ul(j,k,nt2))*
     1          (ul(j+1,k,nt2)+ul(j,k,nt2))/hh(j+1,k))-
     1          ((ul(j-1,k,nt2)+ul(j,k,nt2))*
     1           (ul(j-1,k,nt2)+ul(j,k,nt2))/hh(j,k  )))

     8       -w2  *( (ul(j  ,k+1,nt2)+ul(j  ,k  ,nt2))*
     8                (vl(j  ,k+1,nt2)+vl(j+1,k+1,nt2))/
     8                (hh(j+1,k  )+hh(j  ,k  )+
     8                 hh(j+1,k+1)+hh(j  ,k+1))

     8               - (ul(j  ,k  ,nt2)+ul(j  ,k-1,nt2))*
     8                 (vl(j  ,k  ,nt2)+vl(j+1,k  ,nt2))/
     8                 (hh(j+1,k-1)+hh(j  ,k-1)
     8                 +hh(j+1,k  )+hh(j  ,k  )))
     2  + w3*(vl(j,k+1,nt2)+vl(j+1,k+1,nt2)
     2       +vl(j,k,nt2)  +vl(j+1,k  ,nt2))

c    4  -w4*(ul(j+1,k,nt2)+ul(j-1,k,nt2)-2.0*ul(j,k,nt2))
c    4  -w5*(ul(j,k+1,nt2)+ul(j,k-1,nt2)-2.0*ul(j,k,nt2))

     4  -rr*ul(j,k,nt2)/(hh(j,k)+hh(j+1,k))

     5    -w6*(hh(j+1,k)+hh(j,k))*
     5        (hl(j+1,k,nt2)-hl(j  ,k,nt2))
     9   )
      enddo
      enddo
c
c  implement periodic boundary condition for u at k=1
c
      do j=3,jmaxm3
           ul(j,1,nt1)=ul(j,1,nt)+z5*(
     3       tx(j,1)
     -       -wl*(((ul(j+1,1,nt2)+ul(j,1,nt2))*
     1             (ul(j+1,1,nt2)+ul(j,1,nt2))/hh(j+1,1))-
     1            ((ul(j-1,1,nt2)+ul(j,1,nt2))*
     1             (ul(j-1,1,nt2)+ul(j,1,nt2))/hh(j,1  )))

     8       -w2  *( (ul(j  ,2,nt2)+ul(j  ,1,nt2))*
     8                (vl(j  ,2,nt2)+vl(j+1,2,nt2))/
     8                (hh(j+1,1)+hh(j,1)+
     8                 hh(j+1,2)+hh(j,2))

     8               - (ul(j  ,1  ,nt2)+ul(j  ,kmax,nt2))*
     8                 (vl(j  ,1  ,nt2)+vl(j+1,1  ,nt2))/
     8                 (hh(j+1,kmax)+hh(j  ,kmax)
     8                 +hh(j+1,1  )+hh(j  ,1  )))

     2  + w3*(vl(j,2,nt2)+vl(j+1,2,nt2)
     2       +vl(j,1,nt2)+vl(j+1,1,nt2))

c    4  -w4*(ul(j+1,1,nt2)+ul(j-1,1,nt2)-2.0*ul(j,1,nt2))
c    4  -w5*(ul(j,2,nt2)+ul(j,kmax,nt2)-2.0*ul(j,1,nt2))

     4  -rr*ul(j,1,nt2)/(hh(j,1)+hh(j+1,1))

     5    -w6*(hh(j+1,1)+hh(j,1))*
     5        (hl(j+1,1,nt2)-hl(j,1,nt2))
     9  )
      enddo
c
c  implement periodic boundary condition at for u k=kmax
c
      do j=3,jmaxm3
           ul(j,kmax,nt1)=ul(j,kmax,nt)+z5*(
     3       tx(j,kmax)
     -       -wl*(((ul(j+1,kmax,nt2)+ul(j,kmax,nt2))*
     1             (ul(j+1,kmax,nt2)+ul(j,kmax,nt2))/hh(j+1,kmax))-
     1            ((ul(j-1,kmax,nt2)+ul(j,kmax,nt2))*
     1             (ul(j-1,kmax,nt2)+ul(j,kmax,nt2))/hh(j,kmax  )))

     8       -w2  *( (ul(j  ,1,nt2)+ul(j  ,kmax  ,nt2))*
     8                (vl(j  ,1,nt2)+vl(j+1,1,nt2))/
     8                (hh(j+1,kmax  )+hh(j  ,kmax  )+
     8                 hh(j+1,1)+hh(j  ,1))

     8               - (ul(j  ,kmax  ,nt2)+ul(j  ,kmaxm1,nt2))*
     8                 (vl(j  ,kmax  ,nt2)+vl(j+1,kmax  ,nt2))/
```

```
c     8                (hh(j+1,kmaxm1)+hh(j  ,kmaxm1)
c     8                +hh(j+1,kmax  )+hh(j  ,kmax  )))

      2  + w3*(v1(j,1    ,nt2)+v1(j+1  ,1    ,nt2)
      2       +v1(j,kmax,nt2)  +v1(j+1,kmax,nt2))

c     4  -w4*(u1(j+1,kmax,nt2)+u1(j-1,kmax  ,nt2)-2.0*u1(j,kmax,nt2))
c     4  -w5*(u1(j  ,1    ,nt2)+u1(j  ,kmaxm1,nt2)-2.0*u1(j,kmax,nt2))

      4  -rr*u1(j,kmax,nt2)/(hh(j,kmax)+hh(j+1,kmax))

      5    -w6*(hh(j+1,kmax)+hh(j,kmax))*
      5        (h1(j+1,kmax,nt2)-h1(j,kmax,nt2))
      9   )
       enddo
c
c
c           v1 equation
c
       do k=2,kmaxm1
       do j=3,jmaxm2
        v1(j,k,nt1)=v1(j,k,nt)+z5*(
c
      3  ty(j,k)
c     1   -w7*(((v1(j,k+1,nt2)+v1(j,k,nt2))*
c     1         (v1(j,k+1,nt2)+v1(j,k,nt2))/hh(j,k))-
c     1        ((v1(j,k,nt2)+v1(j,k-1,nt2))*
c     1         (v1(j,k,nt2)+v1(j,k-1,nt2))/hh(j,k-1)))

c     8 -w8   *( (u1(j  ,k  ,nt2)+u1(j  ,k-1,nt2))*
c     8          (v1(j  ,k  ,nt2)+v1(j+1,k  ,nt2))
c     8         /(hh(j  ,k)+hh(j+1,k)
c     8          +hh(j  ,k-1)+hh(j+1,k-1))
c     8       -  (u1(j-1,k  ,nt2)+u1(j-1,k-1,nt2))*
c     8          (v1(j  ,k  ,nt2)+v1(j-1,k  ,nt2))
c     8         /(hh(j-1,k)+hh(j  ,k)
c     8          +hh(j-1,k-1)+hh(j  ,k-1)) )


      2   -w9   *(u1(j  ,k,nt2)+u1(j  ,k-1,nt2)
      2          +u1(j-1,k,nt2)+u1(j-1,k-1,nt2))

c     4   -w10*(v1(j+1,k,nt2)+v1(j-1,k,nt2)-2.0*v1(j,k,nt2))
c     4   -w11*(v1(j,k+1,nt2)+v1(j,k-1,nt2)-2.0*v1(j,k,nt2))

      4  -rr*v1(j,k,nt2)/(hh(j,k)+hh(j,k-1))

      5      -w12*(hh(j,k    )+hh(j,k-1))
      5          *(h1(j,k,nt2)-h1(j,k-1,nt2))


      9    )
       enddo
       enddo
c implement periodic boundary condition for v at k=1
c
       do j=3,jmaxm2
         v1(j,1,nt1)=v1(j,1,nt)+z5*(
      3      ty(j,1)
c     1   -w7*(((v1(j,2,nt2)+v1(j,1,nt2))*
c     1         (v1(j,2,nt2)+v1(j,1,nt2))/hh(j,1))-
c     1        ((v1(j,1,nt2)+v1(j,kmax,nt2))*
c     1         (v1(j,1,nt2)+v1(j,kmax,nt2))/hh(j,kmax)))

c     8 -w8   *( (u1(j  ,1    ,nt2)+u1(j  ,kmax,nt2))*
c     8          (v1(j  ,1    ,nt2)+v1(j+1,1    ,nt2))
c     8         /(hh(j  ,1        )+hh(j+1,1        )
c     8          +hh(j  ,kmax    )+hh(j+1,kmax    ))
c     8       -  (u1(j-1,1    ,nt2)+u1(j-1,kmax,nt2))*
c     8          (v1(j  ,1    ,nt2)+v1(j-1,1    ,nt2))
c     8         /(hh(j-1,1        )+hh(j  ,1        )
c     8          +hh(j-1,kmax    )+hh(j  ,kmax    )) )


      2   -w9   *(u1(j  ,1,nt2)+u1(j  ,kmax,nt2)
      2          +u1(j-1,1,nt2)+u1(j-1,kmax,nt2))

c     4   -w10*(v1(j+1,1,nt2)+v1(j-1,1    ,nt2)-2.0*v1(j,1,nt2))
c     4   -w11*(v1(j  ,2,nt2)+v1(j  ,kmax,nt2)-2.0*v1(j,1,nt2))

      4  -rr*v1(j,1,nt2)/(hh(j,1)+hh(j,kmax))

      5    -w12*(hh(j,1    )+hh(j,kmax))
      5        *(h1(j,1,nt2)-h1(j,kmax,nt2))

      9   )
       enddo
c implement periodic boundary condition for v at k=kmax
c
       do j=3,jmaxm2
        v1(j,kmax,nt1)=v1(j,kmax,nt)+z5*(
c
      3     ty(j,kmax)
c     1   -w7*(((v1(j,1,nt2)+v1(j,kmax,nt2))*
c     1         (v1(j,1,nt2)+v1(j,kmax,nt2))/hh(j,kmax))-
c     1        ((v1(j,kmax,nt2)+v1(j,kmaxm1,nt2))*
c     1         (v1(j,kmax,nt2)+v1(j,kmaxm1,nt2))/hh(j,kmaxm1)))

c     8 -w8   *( (u1(j  ,kmax  ,nt2)+u1(j  ,kmaxm1,nt2))*
c     8          (v1(j  ,kmax  ,nt2)+v1(j+1,kmax  ,nt2))
c     8         /(hh(j  ,kmax )+hh(j+1,kmax )
c     8          +hh(j  ,kmaxm1)+hh(j+1,kmaxm1))
c     8       -  (u1(j-1,kmax  ,nt2)+u1(j-1,kmaxm1,nt2))*
c     8          (v1(j  ,kmax  ,nt2)+v1(j-1,kmax  ,nt2))
c     8         /(hh(j-1,kmax )+hh(j  ,kmax  )
c     8          +hh(j-1,kmaxm1)+hh(j  ,kmaxm1)) )


      2   -w9   *(u1(j  ,kmax,nt2)+u1(j  ,kmaxm1,nt2)
      2          +u1(j-1,kmax,nt2)+u1(j-1,kmaxm1,nt2))

c     4   -w10*(v1(j+1,kmax,nt2)+v1(j-1,kmax,nt2)-2.0*v1(j,kmax,nt2))
c     4   -w11*(v1(j,1,nt2)+v1(j,kmaxm1,nt2)-2.0*v1(j,kmax,nt2))

      4  -rr*v1(j,kmax,nt2)/(hh(j,kmax)+hh(j,kmaxm1))

      5    -w12*(hh(j,kmax    )+hh(j,kmaxm1))
      5        *(h1(j,kmax,nt2)-h1(j,kmaxm1,nt2))

      9   )
       enddo
c
c
c      h1 equation
c
       do k=2,kmaxm1
       do j=3,jmaxm2
        h1(j,k,nt1)= h1(j,k,nt)+z5*(
c
```

```
     1   -w13*(u1(j,k  ,nt2)-u1(j-1,k,nt2))
     1   -w14*(v1(j,k+1,nt2)-v1(j,k  ,nt2))
     9  )
      enddo
      enddo
c
c  implement periodic boundary for h at k=1
      do j=3,jmaxm2
       h1(j,1,nt1)= h1(j,1,nt)+z5*(
c
     1   -w13*(u1(j,1  ,nt2)-u1(j-1,1,nt2))
     1   -w14*(v1(j,2,nt2)-v1(j,1  ,nt2))
     9  )
      enddo
c
c; implement periodic boundary for h at k=kmax
      do j=3,jmaxm2
       h1(j,kmax,nt1)= h1(j,kmax,nt)+z5*(
c
     1   -w13*(u1(j,kmax  ,nt2)-u1(j-1,kmax,nt2))
     1   -w14*(v1(j,1,nt2)-v1(j,kmax  ,nt2))
     9  )
      enddo
c
c  boundary conditions at the walls
      do k=1,kmax
c      v1(2,k,nt1)=-v1(3,k,nt1)
c      v1(jmaxm1,k,nt1)=-v1(jmaxm2,k,nt1)
       v1(2,k,nt1)= v1(3,k,nt1)
       v1(jmaxm1,k,nt1)= v1(jmaxm2,k,nt1)
      enddo
c
c if "saving" this level, write out one level
c
c     if(n.ge.nndyini) then

      if (mod(n,nwrite).eq.0) then
      htan=h1(15,20,nt1)-h1(5,20,nt1)
      tim=float(n)/float(ndt1dy)
      print *,'va a escribir',n,tim,
     1   u1(10,20,nt1),v1(10,20,nt1),htan
      nprint=nt1
c
      do k=1,kmax
      do j=1,jmax
      tem5(j,k)=u1(j,k,nprint)
      enddo
      enddo
      write(43) n,((tem5(j,k),j=1,jmax),k=1,kmax)


      do k=1,kmax
      do j=1,jmax
      tem5(j,k)=v1(j,k,nprint)
      enddo
      enddo
      write(45) n,((tem5(j,k),j=1,jmax),k=1,kmax)

      do k=1,kmax
      do j=1,jmax
      tem5(j,k)=h1(j,k,nprint)
      enddo
      enddo
      write(47) n,((tem5(j,k),j=1,jmax),k=1,kmax)
c
      end if
c     endif
c
c advance timestep
c
  400 continue
c
      stop 'after end'
      end
```

Computer exercise #5

Kelvin waves

To simplify the analysis and extract the basic physics of the Kelvin waves we start with the equation for an homogeneous flow for which the shallow-water linear model is adequate. the equations are:

$$\frac{\partial u}{\partial t} - fv = -g\frac{\partial \eta}{\partial x} \qquad (21)$$

$$\frac{\partial v}{\partial t} + fu = -g\frac{\partial \eta}{\partial y} \qquad (22)$$

$$\frac{\partial \eta}{\partial t} + H\left(\frac{\partial u}{\partial x} + \frac{\partial v}{\partial y}\right) = 0 \qquad (23)$$

To simplify the model further let's imagine a seminfinite ocean bounded by a horizontal bottom above a free surface, and on one side by a vertical wall.

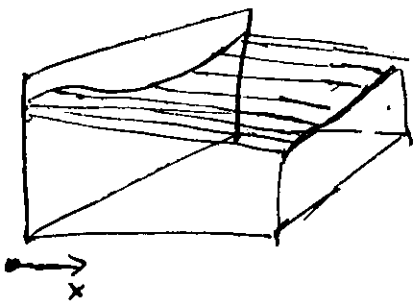

Since the normal velocity at the wall (u) should vanish, a suggested possible mode of oscillation is with the normal velocity equal zero everywhere.

So using as an apriory condition

$u = 0$ in 21, 22, 23

from equation ② an ③ with $u=0$, it is easy to get an equation for v:

$$\frac{\partial^2 v}{\partial t^2} = \sqrt{gH}\,\frac{\partial^2 v}{\partial y^2}$$

this defines a wave that propagates in the positive and negative direction

$$v = F(x, y+ct) + G(x, y-ct)$$

where $c = \sqrt{gH}$.

Returning To 2, 3 an equation for η can be found

$$\eta = -\sqrt{\frac{H}{g}}\,F(x,y+ct) + \sqrt{\frac{H}{g}}\,G(x,y-ct)$$

and the structure of the function F and G is determined by the use of (21)

$$\frac{\partial F}{\partial x} = -\frac{f}{\sqrt{gH}}F \;;\; \frac{\partial G}{\partial x} = +\frac{f}{\sqrt{gH}}G$$

or

$$F = \mathcal{F}(y+ct)\,e^{-x/R} \;;\; G = \mathcal{G}(y-ct)\,e^{x/R}$$

where $R = \frac{\sqrt{gH}}{f}$, the second solution increases exponentially with x so it is precluded from the problem. Combining these results one gets the solution:

$$u = 0$$

$$v = \sqrt{gH}\, \mathcal{F}(y + ct)\, e^{-x/R}$$

$$\eta = -H\, \mathcal{F}(y + ct)\, e^{-x/R}$$

where $\mathcal{F}$ is any function of its argument. Because the exponential decay away from the boundary the Kelvin wave is said to be trapped. For positive f the wave travels with the coast to its right.

In some instances, mainly in the investigation of upper-ocean processes, the ocean can be imagined as made up of two layers, an upper dynamically active layer and a lower layer that is infinitely deep and at rest. The system of equations appropriate for this problem is the so called reduced gravity equation. For the linear case the transport equations are:

$$\frac{\partial U}{\partial t} - fV = -\frac{g'}{2}\frac{\partial h^2}{\partial x} \qquad (24)$$

$$\frac{\partial V}{\partial t} + fU = -\frac{g'}{2}\frac{\partial h^2}{\partial y} \qquad (25)$$

$$\frac{\partial h}{\partial t} + \frac{\partial U}{\partial x} + \frac{\partial V}{\partial y} = 0 \qquad (26)$$

where $g' = g\frac{\Delta\rho}{\rho}$ is the reduced gravity which includes the density difference between the upper active and bottom inert layers.

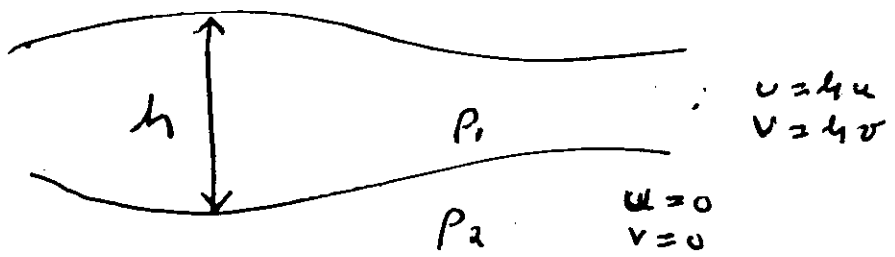

These equations have the same form that the shallow water equations with the only difference that g is substituded by the usually much smaller g'. This has the effect of reducing both, the radius of deformation $R = \frac{\sqrt{g'H}}{f}$ and the propagation speed $c = \sqrt{g'H}$. It is very fortunate in terms of numerical modeling, since smaller c means that for the same size of grid the time interval (Δt) can be much larger before numerical instability sets in. Also with smaller R the decay of the waves can be clearly observed in a smaller domain.

Model redgrav.f implements equation 24-26. Some of the parameters in the program are:

$g' = .03$ m/s^2
$h_0 = 50$ m
$f = 6.6 \times 10^{-5}$ (s^{-1})

$\frac{\Delta x}{2} = \frac{\Delta y}{2} = 5000$ m
$\Delta t = 20$ min
imax = 100
jmax = 25

First compile and run the program Crearedgra.f To make the mask needed to run this program (see boundary conditions below). Compile and run the program redgrav.f with the parameters given. Make contour plots of v and h for 10 or 15 days (every 1/4 day, say). Describe the results. Estimate the propagation speed and offshore decaying factor. Compare to the analytical solution. Why don't you see these waves in the in exercise #3. Is the speed of propagation of the waves going in the positive y direction equal to the one going in the negative y direction? why? Is the solution for u similar to that for v and h? why?

Due to the way the initial forcing is, the initial anomaly in the right side of the Channel is a downwelling signal and the one in the left side an upwelling signal. How is the velocity associated to these signals? Why do you think the "northward" wave is better resolved than the "southward" wave? Try changing the forcing so that you have downwelling signals in both sides, and check that the two waves are equally resolved.

In the previous paragraph we mention southward and northward moving waves, this is only because of the geometry of the domain (the same as in the previous exercises). In reality these waves have nothing to do with north and south, they owe their existence to the presence of a wall. This model has the coding to implement any reasonable geometry. The position of the boundary is specified in the u, v and h fields created by the program creatbdgrd and read into the program as the initial fields (Read(52)).

The first thing that the program does is to decide if an h, u and v point are inside the domain. It does that by checking that it and its neighbors are not especial values (9999.0 For example, h_{jk} is inside the domain, i.e. hatsea(j,k) = .true., if none of the following points are especial values;

$h_{j-1,k+1}$ $h_{j,k+1}$ $h_{j+1,k+1}$

$h_{j-1,k}$ h_{jk} $h_{j+1,k}$

$h_{j-1,k-1}$ $h_{j,k-1}$ $h_{j+1,k-1}$

then it checks if the u points are southern or northern boundary points. For example $U_{j,k}$ is a northern boundary point if $U_{j,k}$ and its neighbors to the south are not especial values but its neighbor to the north is, i.e.

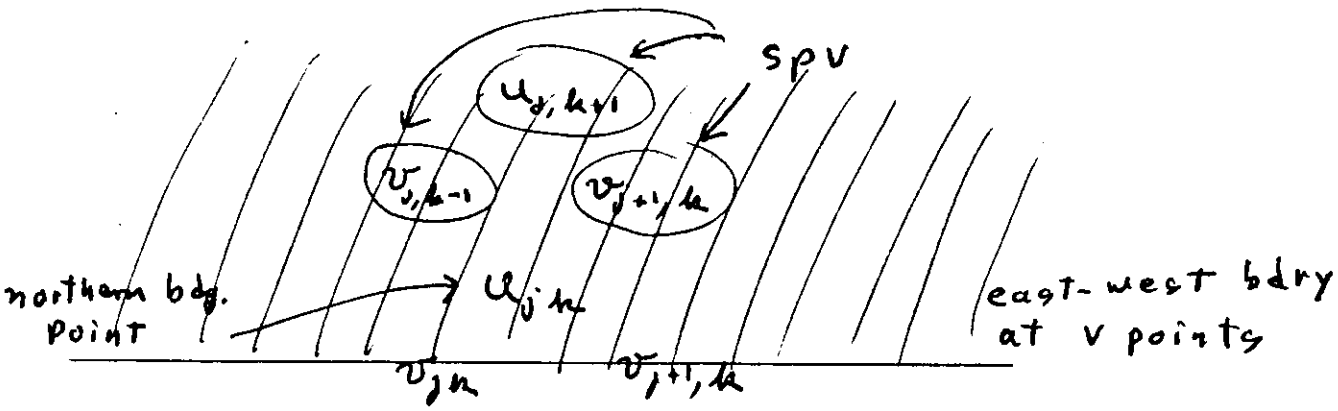

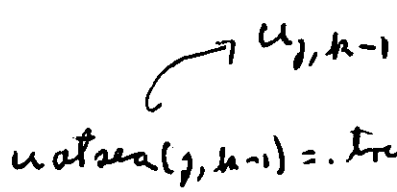

then in a similar way checks for v eastern or western boundary points. After running the main loop for the "atsea" points, the boundary points are updated by changing its value to the value of the negative of its neighbor to the sea. For example a northern boundary point U_B would be updated as $-U_{B-1}$.

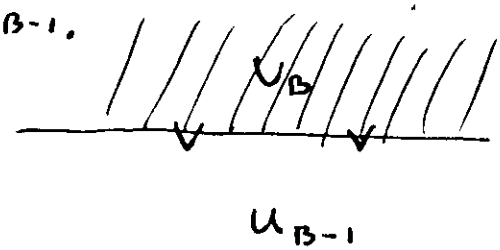

this ensures that the tangential velocity is zero right at the boundary. this is the non-slip boundary condition. If we want to implement the no-gradient B.C., for example, we would use the condition $v_B = v_{B-1}$ after the main loop is run.

Change the program Crearedgra.f so that the domain of the model changes as shown in the figure (or in any other way). Just de comment the commented lines in crearedgra.f.

Make the same run as before, and plot a few contours of v or h. Does the west-east wall slow the wave? I don't think so...!

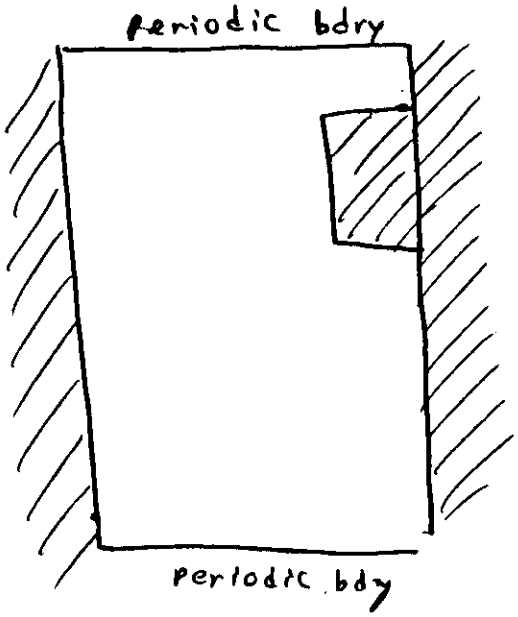

```
c    reduced gravity model
c
      parameter(jjmax=25,kkmax=100)
c
      logical*2 hatsea(jjmax,kkmax),uatsea(jjmax,kkmax)
     1 ,vatsea(jjmax,kkmax)
c
      integer  jjeas(200),kkeas(200),jjwes(200),kkwes(200)
     1        ,jjnor(200),kknor(200),jjsou(200),kksou(200)
c
      dimension h1(jjmax,kkmax,2),u1(jjmax,kkmax,2),v1(jjmax,kkmax,2)
      dimension tx(jjmax,kkmax),ty(jjmax,kkmax)
      dimension tem5(jjmax,kkmax)
c
c    open files
c
      open(43,file='uredg',form='unformatted')
      open(45,file='vredg',form='unformatted')
      open(47,file='hredg',form='unformatted')
      open(52,file='uvhr',form='unformatted')
c
c    all quantities are in mks units
c  time step:
      delt=20.*60.0
c  mesh spacing x  direction:
      delx= 5000.0
c  mesh spacing in y direction:
      dely= 5000.0
c  seconds per day
      secday=86400.0
c  # intervals in one day
      ndt1dy=secday/delt
c  day 1
      iday1=1*ndt1dy
c  last day of integration:
      daymax=30.
c  number of time steps between forward differences
      nstep=99
c  special value for points over land
      spv=9999.0
      pi=4.*atan(1.)
c  initial layer depth
      h0=50.0
c   wind stress coef.
      tau=.0001
c
c  initialize all parameters
c  beginning iteration level:
      nnow=1
      nt1=1
      nt2=2
c
c  initialize internal parameters
c
c  value of gravity:
      g=0.030
c  Coriolis parameter :
      f=6.6e-5
c  number of time steps between writes:
c        (twice per day)
c     nwrite=secday/delt
      nwrite=ndt1dy
      print *,'nwrite?'
      read(*,*) xnwr
      nwrite=xnwr*float(ndt1dy)

c num. of time steps between writes to time series data
      ntimse=ndt1dy*6
c  coefficient of eddy viscocity:
      avisc=100.00
c
      jmax=jjmax
      kmax=kkmax
      jmaxs2=jjmax/2
      kmaxs2=kkmax/2
      kmaxm1=kmax-1
      jmaxm1=jmax-1
      kmaxm2=kmax-2
      jmaxm2=jmax-2
      jmaxm3=jmax-3
c  initialize u,v,h arrays:
      read(52) u1
      read(52) v1
      read(52) h1
      do k=1,kmax
      do j=1,jmax
      if(h1(j,k,1).ne.spv) then
      h1(j,k,1)=h0
      h1(j,k,2)=h1(j,k,1)
      endif
      enddo
      enddo
cc
cc
c
c initialize constants outside n (time) loop
c
c  maximum iteration number:
      nmax=daymax*secday/delt
c
      w1=1./(8.*delx)
      w2=1./(2.*dely)
      w3=f/4.
      w4=avisc/(delx*delx)
      w5=avisc/(dely*dely)
      w6=g/(2.*4.*delx)
      w7=1./(8.*dely)
      w8=1./(2.*delx)
      w9=f/4.
      w10=avisc/(delx*delx)
      w11=avisc/(dely*dely)
      w12=g/(2.*4.*dely)
      w13=1./(2.*delx)
      w14=1./(2.*dely)
      rr=r*2.
c load wind values (tx,ty)
c  una funcion del viento

       kmaxs2=kmax/2
       do k=1,kmax
       do j=1,jmax
       tx(j,k)=0.0
       ty(j,k)=0.0
       enddo
       enddo

c    set up logical*1 vectors for interior loop
c
```

```
c                hatsea true for each point s.t. it and
c                its 8 neighbors are all sea points
c
      iieas=0
      iiwes=0
      iinor=0
      iisou=0
c
      do k=2,kmaxm1
      do j=2,jmaxm1
c
      hatsea(j,k)=((h1(j,k,1).ne.spv) .and.
     1             (h1(j-1,k-1,1).ne.spv) .and.
     1             (h1(j-1,k,1).ne.spv) .and.
     1             (h1(j-1,k+1,1).ne.spv) .and.
     1             (h1(j,k-1,1).ne.spv) .and.
     5             (h1(j,k+1,1).ne.spv) .and.
     6             (h1(j+1,k-1,1).ne.spv) .and.
     7             (h1(j+1,k,1).ne.spv) .and.
     8             (h1(j+1,k+1,1).ne.spv))
c
c                uatsea true for each point s.t. it and
c                its 8 neighbors are all sea points
c
c
      uatsea(j,k)=((u1(j,k,1).ne.spv) .and.
     1             (u1(j-1,k-1,1).ne.spv) .and.
     1             (u1(j-1,k,1).ne.spv) .and.
     1             (u1(j-1,k+1,1).ne.spv) .and.
     1             (u1(j,k-1,1).ne.spv) .and.
     5             (u1(j,k+1,1).ne.spv) .and.
     6             (u1(j+1,k-1,1).ne.spv) .and.
     7             (u1(j+1,k,1).ne.spv) .and.
     8             (u1(j+1,k+1,1).ne.spv))
c                vatsea true for each point s.t. it and
c                its 8 neighbors are all sea points
c
c
      vatsea(j,k)=((v1(j,k,1).ne.spv) .and.
     1             (v1(j-1,k-1,1).ne.spv) .and.
     1             (v1(j-1,k,1).ne.spv) .and.
     1             (v1(j-1,k+1,1).ne.spv) .and.
     1             (v1(j,k-1,1).ne.spv) .and.
     5             (v1(j,k+1,1).ne.spv) .and.
     6             (v1(j+1,k-1,1).ne.spv) .and.
     7             (v1(j+1,k,1).ne.spv) .and.
     8             (v1(j+1,k+1,1).ne.spv))
c
c
      enddo
      enddo
c
c     boundary point for u and v
c
      do k=2,kmaxm1
      do j=2,jmaxm1
c
c                northern true for northern boundary points
c
      if(           (u1(j,k,1).ne.spv) .and.
     1              (u1(j-1,k,1).ne.spv) .and.
     2              (u1(j+1,k,1).ne.spv) .and.
     2              (u1(j,k-1,1).ne.spv) .and.
     3              (u1(j,k+1,1).eq.spv) )       then
        iinor=iinor+1
        jjnor(iinor)=j
        kknor(iinor)=k
      endif
      enddo
      enddo
c
      do k=2,kmaxm1
      do j=2,jmaxm1
c                southern true for southern boundary points
c
      if(           (u1(j,k,1).ne.spv) .and.
     1              (u1(j-1,k,1).ne.spv) .and.
     2              (u1(j+1,k,1).ne.spv) .and.
     2              (u1(j,k+1,1).ne.spv) .and.
     3              (u1(j,k-1,1).eq.spv) )       then
        iisou=iisou+1
        jjsou(iisou)=j
        kksou(iisou)=k
      endif
      enddo
      enddo
c
      do k=2,kmaxm1
      do j=2,jmaxm1
c                eastern true for eastern boundary points
      if(           (v1(j,k,1).ne.spv) .and.
     1              (v1(j,k-1,1).ne.spv) .and.
     2              (v1(j,k+1,1).ne.spv) .and.
     2              (v1(j-1,k,1).ne.spv) .and.
     3             (v1(j+1,k,1).eq.spv) )       then
        iieas=iieas+1
        jjeas(iieas)=j
        kkeas(iieas)=k
      endif
      enddo
      enddo
c
c
c                western true for western boundary points
c
      do k=2,kmaxm1
      do j=2,jmaxm1
      if  (         (v1(j,k,1).ne.spv) .and.
     1              (v1(j,k-1,1).ne.spv) .and.
     2              (v1(j,k+1,1).ne.spv) .and.
     2              (v1(j+1,k,1).ne.spv) .and.
     3              (v1(j-1,k,1).eq.spv))       then
        iiwes=iiwes+1
        jjwes(iiwes)=j
        kkwes(iiwes)=k
      endif
      enddo
      enddo
c
      print *,'iwes=',iiwes
      print *,'ieas=',iieas
      print *,'iinor=',iinor
      print *,'iisou=',iisou
c
c     drag coefficient (including a 2 missing in the eq.  )
c
c
c  begin time loop
c
      do 400 n=nnow,nmax
```

```
c
c                toggle relevant descriptors each time step to
c                point to 1st or 2nd planes of u, v and h
c                also set up forward differences on the first and
c                every nstep-th time step thereafter else set up
c                centered differences
c
c flip time indices
c
      nsave=nt1
      nt1=nt2
      nt2=nsave
c
c for start-up and for every nstep-th time step use forward difference
c
      if (mod(n,nstep).eq.1) then
         nt=nt2
         z5=delt
      else
c use centered time differences
         nt=nt1
         z5=2.*delt
      end if
c
c                 lhs of equations on plane nt1
c                 and rhs terms mostly on plane nt2
c                choose  centered or forward differences
c                 reflect boundary points at plane nt1
c
c
c
      if(n.gt.iday1) tau=0.0
      do k=1,kmax
      do j=1,jmax
         tx(j,k)=0.0
         ty(j,k)=0.0
        if(k.gt.46.and.k.lt.54) ty(j,k)=tau
      enddo
      enddo
c
c
c
c        u1 equation
c
      do k=2,kmaxm1
      do j=2,jmaxm1
      if(uatsea(j,k).eq..true.) then
        u1(j,k,nt1)=u1(j,k,nt)+z5*(
c
     3       tx(j,k)

     2  + w3*(v1(j,k+1,nt2)+v1(j+1,k+1,nt2)
     2       +v1(j,k,nt2)  +v1(j+1,k  ,nt2))


     5    -w6*(h1(j+1,k,nt2)*h1(j+1,k,nt2)-
     5         h1(j  ,k,nt2)*h1(j  ,k,nt2))
     9   )
      endif
      enddo
      enddo
c
c  implement periodic boundary condition for u at k=1
c
      do j=3,jmaxm3
            u1(j,1,nt1)=u1(j,1,nt)+z5*(
     3      tx(j,1)

     2  + w3*(v1(j,2,nt2)+v1(j+1,2,nt2)
     2       +v1(j,1,nt2)+v1(j+1,1,nt2))


     5    -w6*(h1(j+1,1,nt2)*h1(j+1,1,nt2)-
     5         h1(j  ,1,nt2)*h1(j  ,1,nt2))
     9  )
      enddo
c
c  implement periodic boundary condition at for u k=kmax
c
      do j=3,jmaxm3
            u1(j,kmax,nt1)=u1(j,kmax,nt)+z5*(
     3      tx(j,kmax)

     2  + w3*(v1(j,1   ,nt2)+v1(j+1  ,1   ,nt2)
     2       +v1(j,kmax,nt2)  +v1(j+1,kmax,nt2))


     5    -w6*(h1(j+1,kmax,nt2)*h1(j+1,kmax,nt2)
     5         -h1(j  ,kmax,nt2)*h1(j  ,kmax,nt2))
     9   )
      enddo
c
      do iii=1,iinor
         j=jjnor(iii)
         k=kknor(iii)
         u1(j,k,nt1)=-u1(j,k-1,nt1)
         u1(j,k,nt1)=u1(j,k-1,nt1)
      enddo
c
      do iii=1,iisou
         j=jjsou(iii)
         k=kksou(iii)
         u1(j,k,nt1)=-u1(j,k+1,nt1)
         u1(j,k,nt1)=u1(j,k+1,nt1)
      enddo
c
c             v1 equation
c
      do k=2,kmaxm1
      do j=2,jmaxm1
      if(vatsea(j,k).eq..true.) then
       v1(j,k,nt1)=v1(j,k,nt)+z5*(
c
     3  ty(j,k)

     2   -w9   *(u1(j  ,k,nt2)+u1(j  ,k-1,nt2)
     2          +u1(j-1,k,nt2)+u1(j-1,k-1,nt2))


     5      -w12*(h1(j,k  ,nt2)*h1(j,k  ,nt2)-
     5            h1(j,k-1,nt2)*h1(j,k-1,nt2))

     9    )
      endif
      enddo
      enddo
c implement periodic boundary condition for v at k=1
c
```

```
      do j=3,jmaxm2
        v1(j,1,nt1)=v1(j,1,nt)+z5*(
     3      ty(j,1)

     2   -w9    *(u1(j   ,1,nt2)+u1(j   ,kmax,nt2)
     2           +u1(j-1,1,nt2)+u1(j-1,kmax,nt2))


     5    -w12*(h1(j,1    ,nt2)*h1(j,1    ,nt2)-
     5          h1(j,kmax,nt2)*h1(j,kmax,nt2))

     9   )
      enddo
c  implement periodic boundary condition for v at k=kmax
c
      do j=3,jmaxm2
       v1(j,kmax,nt1)=v1(j,kmax,nt)+z5*(
c
     3      ty(j,kmax)

     2   -w9    *(u1(j   ,kmax,nt2)+u1(j   ,kmaxm1,nt2)
     2           +u1(j-1,kmax,nt2)+u1(j-1,kmaxm1,nt2))


     5    -w12*(h1(j,kmax   ,nt2)*h1(j,kmax   ,nt2)-
     5          h1(j,kmaxm1,nt2)*h1(j,kmaxm1,nt2))

     9   )
      enddo
c
      do iii=1,iieas
         j=jjeas(iii)
         k=kkeas(iii)
         v1(j,k,nt1)=-v1(j-1,k,nt1)
         v1(j,k,nt1)=v1(j-1,k,nt1)
      enddo

         v1(jmaxm1,1,nt1)=    -v1(jmaxm2,1,nt1)
         v1(jmaxm1,kmax,nt1)=-v1(jmaxm2,kmax,nt1)
         v1(jmaxm1,1,nt1)=    v1(jmaxm2,1,nt1)
         v1(jmaxm1,kmax,nt1)=v1(jmaxm2,kmax,nt1)
c
c
      do iii=1,iiwes
         j=jjwes(iii)
         k=kkwes(iii)
         v1(j,k,nt1)=-v1(j+1,k,nt1)
         v1(j,k,nt1)=v1(j+1,k,nt1)
      enddo

         v1(2,1,nt1)=-v1(3,1,nt1)
         v1(2,kmax,nt1)=-v1(3,kmax,nt1)
         v1(2,1,nt1)=v1(3,1,nt1)
         v1(2,kmax,nt1)=v1(3,kmax,nt1)
c
c


c      h1 equation
c
      do k=2,kmaxm1
      do j=2,jmaxm1
       if (hatsea(j,k).eq..true.) then
       h1(j,k,nt1)= h1(j,k,nt)+z5*(
c
     1    -w13*(u1(j,k   ,nt2)-u1(j-1,k,nt2))
     1    -w14*(v1(j,k+1,nt2)-v1(j,k   ,nt2))
     9   )
       endif
       enddo
       enddo
c  implement periodic boundary for h at k=1
       do j=3,jmaxm2
        h1(j,1,nt1)= h1(j,1,nt)+z5*(
c
     1    -w13*(u1(j,1   ,nt2)-u1(j-1,1,nt2))
     1    -w14*(v1(j,2,nt2)-v1(j,1   ,nt2))
     9   )
      enddo
c  implement periodic boundary for h at k=kmax
       do j=3,jmaxm2
        h1(j,kmax,nt1)= h1(j,kmax,nt)+z5*(
c
     1    -w13*(u1(j,kmax   ,nt2)-u1(j-1,kmax,nt2))
     1    -w14*(v1(j,1,nt2)-v1(j,kmax   ,nt2))
     9   )
      enddo
99    continue
c
c if "saving" this level, write out one level
c
      if (mod(n,nwrite).eq.0) then
      tim=float(n)/float(ndt1dy)
      print *,'va a escribir, time= ',tim, 'days'
      nprint=nt1
c
      do k=1,kmax
      do j=1,jmax
      tem5(j,k)=u1(j,k,nprint)
      enddo
      enddo
      write(43) n,((tem5(j,k),j=1,jmax),k=1,kmax)


      do k=1,kmax
      do j=1,jmax
      tem5(j,k)=v1(j,k,nprint)
      enddo
      enddo
      write(45) n,((tem5(j,k),j=1,jmax),k=1,kmax)

      do k=1,kmax
      do j=1,jmax
      tem5(j,k)=h1(j,k,nprint)
      enddo
      enddo
      write(47) n,((tem5(j,k),j=1,jmax),k=1,kmax)
c
      end if
c
c advance timestep
c
  400 continue
c
      stop 'after end'
      end
```

JOURNAL OF GEOPHYSICAL RESEARCH, VOL. 94, NO. C3, PAGES 3159–3180, MARCH 15, 1989

The Seasonal and Interannual Variability of the California Current System: A Numerical Model

ALEJANDRO PARES-SIERRA[1] AND JAMES J. O'BRIEN

Mesoscale Air-Sea Interaction Group, Florida State University, Tallahassee

A reduced gravity model that incorporates the geometry of western North America has been used to study the dynamics of the California Current system. Three experiments were performed: first the model was run using 19 years of wind stress from the Comprehensive Ocean-Atmosphere Data Set (local model); a second experiment (remote model) consisted of forcing the model through its southern boundary using the results of a similar reduced gravity equatorial model; in a third experiment, both forcings were used simultaneously (local plus remote model). The main objective of this work was to analyze the low-frequency variability on the California Current system in terms of its contributions from remote and local forcing. Away from the coast, the basic (steady) state of the model is determined by the predominantly negative wind curl through a Sverdrup balance. The general seasonal cycle is in agreement with what has been described by other authors. Through cross-correlation and cross-spectral analysis between the model results and observed sea level data, it was established that most of the interannual variability in sea level height at the coast is due to disturbances of equatorial origin that propagate into the region in the form of coastally trapped Kelvin waves. For the annual frequency variability, on the other hand, it was found that both local and remotely forced variability contribute to the total variance.

1. INTRODUCTION

1.1. *Motivation and Objectives*

During the 1982–1983 El Niño event, waters several degrees warmer than normal were observed in the northeastern Pacific Ocean. The biological and economic implications of this phenomenon are enormous. The distribution and abundance of fish and invertebrates changed remarkably in the coastal waters of the northeastern Pacific Ocean [*Wooster and Fluharty*, 1985]. *Pearcy and Schoener* [1987], for example, report the appearance in the waters of Oregon and Alaska of 13 marine species that had never before been reported north of California. *Simpson* [1984*a*] showed that the anomalous warm waters in the California Current during August 1982 were accompanied by negative salinity anomalies as well as oxygen anomalies. Although it is accepted that the 1982–1983 episode was an exceptionally strong El Niño [e.g., *Pearcy and Schoener*, 1987], it certainly was not an isolated phenomenon. Other anomalous warm events have been observed (for example in 1940–1941, 1957–1958, 1969, and 1972 [*Enfield and Allen*, 1980; *Quinn et al.*, 1984]) and linked to tropical El Niño–Southern Oscillation (ENSO) phenomenon.

In recent years a great amount of research relevant to the interannual oceanic variability in the northeastern Pacific has been done (e.g., *Enfield and Allen* [1980], *Chelton and Davis* [1982], *Christensen et al.* [1983], and *Simpson* [1984*a*, *b*], among others). In spite of all this work, fundamental questions about the generation of this variability still remain unanswered in the literature.

Emery and Hamilton [1985] cite two basic ways to explain the connection between the anomalous warming of the northeastern Pacific Ocean and the tropical El Niño phenomenon, one oceanic and the other atmospheric.

For the first, poleward propagating waves generated in the tropics during an ENSO episode carry the information to the extratopical regions. *McCreary* [1976] first suggested that the California coast might be remotely affected in this form. Theoretical works of *Moore* [1968], *Anderson and Rowlands* [1976], and *Clarke* [1983] have demonstrated that an equatorial wave can generate, upon reflecting on an eastern boundary, a poleward propagating water disturbance in the form of coastal Kelvin waves. Observational evidence [e.g., *Enfield and Allen*, 1980; *Chelton and Davis*, 1982] suggests that much of the oceanic low-frequency variability along the western coast of North America can be accounted for by this mechanism.

A second, nonexclusive explanation for the co-occurrence between equatorial and mid-latitude anomalies invokes an atmospheric teleconnection [*Emery and Hamilton*, 1985]. Under this hypothesis, first presented by *Bjerkness* [1966], an atmospheric link is achieved between the tropical Pacific sea surface temperature (SST) anomalies and the mid-latitude Pacific anomalies via a momentum transfer from a variable Hadley cell. A number of observations and theoretical studies support the importance of such an interaction [e.g., *Namias*, 1976; *Emery and Hamilton*, 1985; *Simpson*, 1983, 1984*a*, *b*]. For the California Current region in particular, *Simpson* [1983, 1984*a*, *b*] concluded that the intensification and expansion of the Aleutian low and the decrease in strength of the Pacific high directly produced, through an enhanced basin wide atmospheric circulation, some of the Californian El Niños, especially those of 1940–1941 and 1982–1983.

The main objective of this research is to investigate the dynamics of the California Current system and its oceanic connection with the equatorial region, not only its anomalous El Niño state, but also the regular average circulation. This research helps to answer questions such as, how much of the interannual variability in the northeastern Pacific Ocean is due to variability in the local forcing (either in the wind stress or its curl) and how much is due to equatorial variability propagated to the region as equatorial-coastal Kelvin waves? In other words, is the observed coherence in the interannual

[1]Now at Scripps Institution of Oceanography, La Jolla, California.

Copyright 1989 by the American Geophysical Union.

Paper number 88JC03932.
0148-0227/89/88JC-03932$05.00

52

frequency band between the northeastern Pacific Ocean and the equatorial ENSO events due to atmospheric or oceanic teleconnections or both?

This paper is divided into five sections. A brief review of the climatology of the California Current is given in section 1.1. The model and its numerical implementation, boundary conditions, and characteristics of the forcing are explained in the section 2. In section 3, general results of the numerical model are presented, and large-scale mean maps of upper layer thickness and current are given. Comparison of model results with observations in the annual and interannual frequency range are also given in section 3. A summary of the results is presented in section 4, while in section 5 the results are discussed and the conclusions are presented.

1.2. *The California Current System*

The California Current (CC) is a wide and slow current that flows in a general northeast to southwest direction following the coast of northwestern America. Its average speed is typically less than 25 cm/s [*Reid and Schwartzlose*, 1962]. Early descriptions of the CC system were given by *Sverdrup et al.* [1942] and *Reid et al.* [1958]. A more recent and detailed description of its characteristics is that of *Hickey* [1979]; since then, reviews of different aspects and time scales have been made by numerous authors. *Lynn and Simpson* [1987] examined the seasonal variability of the CC system using 23 years of California Cooperative Ocean Fisheries Investigations (CalCOFI) data. *McCreary et al.* [1987] studied the dynamics of the CC system using two ocean models, one with shelf and one without.

The CC (an equatorward flow), together with the Davidson Current (a poleward countercurrent that occurs near the coast) and the California undercurrent (a poleward underflow over the continental slope) form the CC system [*Hickey*, 1979]. *Hickey* [1979], shows that the strongest equatorward flow appears in spring and summer, whereas the strongest poleward coastal counterflow appears in fall and winter. During spring and early summer the prevailing winds near the North American coast are north-northwesterly, giving rise to upwelling events that on the average (and with characteristic spatial variability) last from March to July [*Sverdrup et al.*, 1942].

Toward the end of the summer, owing to changing wind directions, the upwelling gradually ceases. Some theoretical studies suggest that the mechanism for the relaxation of the cold upwelling region is in the form of westward radiation of Rossby waves [e.g., *McCreary*, 1976; *Mysak*, 1983]. By fall, a surface layer countercurrent develops (the Davidson Current) which in November, December, and January runs north along the coast to at least latitude 48°N [*Sverdrup et al.*, 1942]. *Lynn and Simpson* [1987], in a modern description of the countercurrent, point out its spatial discontinuities which often give the appearance of inshore cyclonic eddies.

In addition to this annual cycle, an interannual variability of anomalous cold or warm years occurs, an example of which is the record-breaking event of 1982–1983. Although there are several possible causes for the interannual variability in an eastern boundary current [e.g., *Gill*, 1982, pp. 425–428] two mechanisms seem the most important: local anomalous Ekman pumping and remotely forced equatorial-coastal Kelvin waves.

2. THE MODEL

2.1. *Model Description*

We used a nonlinear, reduced gravity model in spherical coordinates to model the California Current system. The model consists of one dynamically active layer of density ρ and depth H on top of an infinitely deep layer of slightly higher density $\rho + \Delta\rho$, the interface between these two layers being a proxy of the ocean pycnocline. The equations were used in the transport mode to facilitate some of the numerical implementation. It was more convenient to use spherical coordinates owing to the large latitudinal extent of the model and because the forcing function as well as the coordinates defining the boundaries were given in degrees of latitude and longitude. The equations defining the model are

$$\frac{\partial U}{\partial t} + \frac{1}{a\cos\theta}\frac{\partial}{\partial\phi}\left(\frac{U^2}{H}\right) + \frac{1}{a}\frac{\partial}{\partial\theta}\left(\frac{UV}{H}\right) - (2\Omega\sin\theta)V = \frac{-g'}{2a\cos\theta}\frac{\partial H^2}{\partial\phi} + \frac{\tau^{\phi}}{\rho} + A\nabla^2 U \tag{1a}$$

$$\frac{\partial V}{\partial t} + \frac{1}{a\cos\theta}\frac{\partial}{\partial\phi}\left(\frac{UV}{H}\right) + \frac{1}{a}\frac{\partial}{\partial\theta}\left(\frac{V^2}{H}\right) + (2\Omega\sin\theta)U = \frac{-g'}{2a}\frac{\partial H^2}{\partial\theta} + \frac{\tau^{(\theta)}}{\rho} + A\nabla^2 V \tag{1b}$$

$$\frac{\partial H}{\partial t} + \frac{1}{a\cos\theta}\left\{\frac{\partial U}{\partial\phi} + \frac{\partial}{\partial\theta}(V\cos\theta)\right\} = 0 \tag{1c}$$

where θ and ϕ are the latitude and longitude, respectively; U and V are the transport (i.e., $(U, V) = H(u, v)$) in the east-west and north-south directions, respectively; H is the depth of the upper layer; $g' = (\Delta\rho/\rho)\,g$ is the reduced gravity; $(\tau^{\theta}, \tau^{\phi})$ are the wind stresses applied throughout the upper layer as a body force; A is an eddy viscosity coefficient; a is the radius of the Earth; and Ω is the angular velocity of rotation of the Earth. The values used for each coefficient are given in Table 1. This model had been used before to simulate the wind-driven circulation in the Indian Ocean [*Luther and O'Brien*, 1985] and the equtorial Pacific [*Kubota and O'Brien*, 1988]. Equations (1) were solved numerically on a 301 × 220 grid covering the northeastern Pacific Ocean from 18°N to 50°N and from 155°W to the American west coast (see Figure 1). The equations were discretized into a staggered grid (Arakawa C-grid). A one twelfth of a degree resolution was used in both zonal and meridional directions (defined as the U to V distance in the staggered grid).

TABLE 1. Values of Parameters Used in the Model

Parameter	Symbol	Value
Radius of Earth	a	6.3784×10^6 m
Coefficient of eddy viscosity	A	350 m²/s
Drag coefficient	C_D	1.5×10^{-3}
Reduced gravity	g'	0.03 m/s²
Upper layer depth	H	200 m
Time step	Δt	20 min
Grid size (latitude and longitude)	$\Delta\theta$, $\Delta\phi$	1/12°
Density of seawater	ρ	1.025×10^3 kg/m³
Density of air	ρ_A	1.2 kg/m³
Earth's rotation	Ω	0.729×10^{-4} s⁻¹

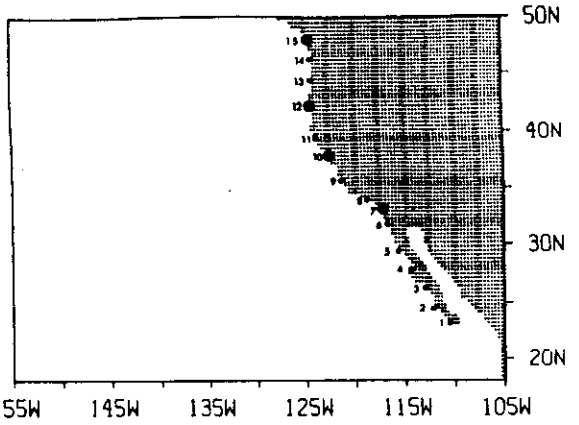

Fig. 1. Model domain. The western, northern, and southern boundaries are open. The stations used by the alongshore variation analysis are shown by dots and identified in Table 2. Larger dots mark the stations used in the westward propagation analysis.

A leapfrog scheme was used for the time integration with 20-min time steps. Every ninety-ninth time step, a forward time differencing was employed to avoid the computational mode. The viscous terms were treated using a DuFort-Frankel scheme. The nonlinear and the Coriolis terms were averaged using adjacent points to get values at the required mesh points prior to computing standard second-order centered finite differences. This procedure helps supress the nonlinear growth of numerical noise in the model [*Luther and O'Brien*, 1985].

Along the eastern boundary of the model, which follows the geometry of the North American coast, a no-slip boundary condition was imposed. The northern, southern, and western boundaries are open boundaries. A variation of the Sommerfeld radiation condition implemented numerically, as described by *Camerlengo and O'Brien* [1980], was imposed on the open boundaries. It is recognized that this model is very simple and cannot account for all the processes in the coastal region. In particular, it is an inviscid model, and hence it is not expected to get the short-scale high-frequency characteristics of the coastal currents correct. However, the model contains the essential physics to tackle the main question of this work, namely, Is there an oceanic or an atmospheric teleconnection between the equatorial and the northeastern Pacific regions? A discussion of the limitations of the model is given in section 5.

2.2. *The Forcing*

Three experiments were run: first, the model was forced by monthly averaged wind stress data from the Comprehensive Ocean-Atmosphere Data Set (COADS). A second experiment was done in which the wind stress was set to zero and the model was forced only through the southern boundary by imposing the results of a similar wind-forced equatorial model. In a third experiment, both forcings were imposed simultaneously. In the three cases, the same parameters (time step, viscosity coefficient, etc.) and time of integration were used so that the results were directly comparable. All experiments were initiated from a state of rest and with an initial upper layer of 200 m.

For the wind-forced model and the combined wind- and boundary-forced model, an initial 4-year spin-up period was run using the long-time monthly wind average. This time is enough for the coastal region to reach its average upper layer thickness and current values. After the initial spin-up period, the three models were integrated in time with a time step of 20 min from January 1, 1961, to December 30, 1979.

A description of the forcing follows.

2.2.1. *The wind.* Nineteen years of wind stress data from the COADS were used. This data for wind stress consist of ship of opportunity observations averaged in time and space every month and every 2° × 2° longitude-latitude squares. The values are in units of pseudo wind stress, i.e.,

$$\frac{\vec{\tau}}{\rho_0 C_D} = \frac{\text{wind stress}}{\rho_0 C_D} = \vec{v}|\vec{v}|$$

where ρ_0 and C_D are the density of the air and drag coefficient respectively. A value of 1.5×10^{-3} was used for C_D. Fortunately, the area of interest has been well covered by commercial ship lines, and the data present few holes. These were filled by linearly interpolating each gap from its eight neighbors. After filling up the gaps for each month, the data was smoothed using a 1-2-1 Hanning filter in both directions. Finally, an IMSL two-dimensional spline was used to interpolate to the resolution of the model. In time the wind was linearly interpolated to a 20-min resolution.

The large-scale winds over the California Current region are driven primarily by two synoptic scale, semipermanent atmospheric pressure systems: the north Pacific high and the continental thermal low over California [*Reid et al.*, 1958].

During the summer, northwesterly winds strengthen owing to a stronger pressure gradient brought by a deepening of the continental low [*Hickey*, 1979]. The winds are mostly parallel to the coast and northwesterly at all latitudes. This is a strongly favorable upwelling condition. Figure 2*a* shows the 19-year averaged July winds used in this study. In the winter season the low weakens, the north Pacific high moves closer to the coast, and the pressure gradient is reduced, weakening the northwesterly wind south of about 40°N and reversing the direction north of that latitude. During this season, the winds are typically southwesterlies off Oregon and Washington [*Hickey*, 1979]. This is a favorable downwelling situation. Figure 2*b* shows the 19-year averaged January winds.

A dominant feature of the winds along the coast is that the maximum magnitude and variance occur near Cape Mendocino (40°N). The standard deviation at Cape Mendocino is 4 to 5 times larger than it is along the coast of northern Baja California, southern California, or Washington [*Halliwell and Allen*, 1984]. The curl of the wind stress is characteristically negative offshore of the California Current region. This is associated with the large-scale anticyclonic atmospheric circulation over the mid-Pacific Ocean. The weakening of the equatorward winds toward the coast creates a typically positive wind curl near the coast. *Nelson* [1977], using 122 years of wind data, compiled an annual cycle of wind stress curl. He shows that positive wind curl occurs along the coast throughout most of the year [*Nelson*, 1977]. This band of positive wind curl has been associated with upwelling events at the coast and with the onset and sustainment of the Davidson Current [e.g., *Munk*, 1950; *McCreary et al.*, 1987] and the California undercurrent [e.g., *Pedlosky*, 1974]. A recent discussion of the mean and seasonal variability of the wind stress curl in the North Pacific was given by *Rienecker and Ehret* [1988].

2.2.2. *Equatorial model.* The relevance of poleward prop-

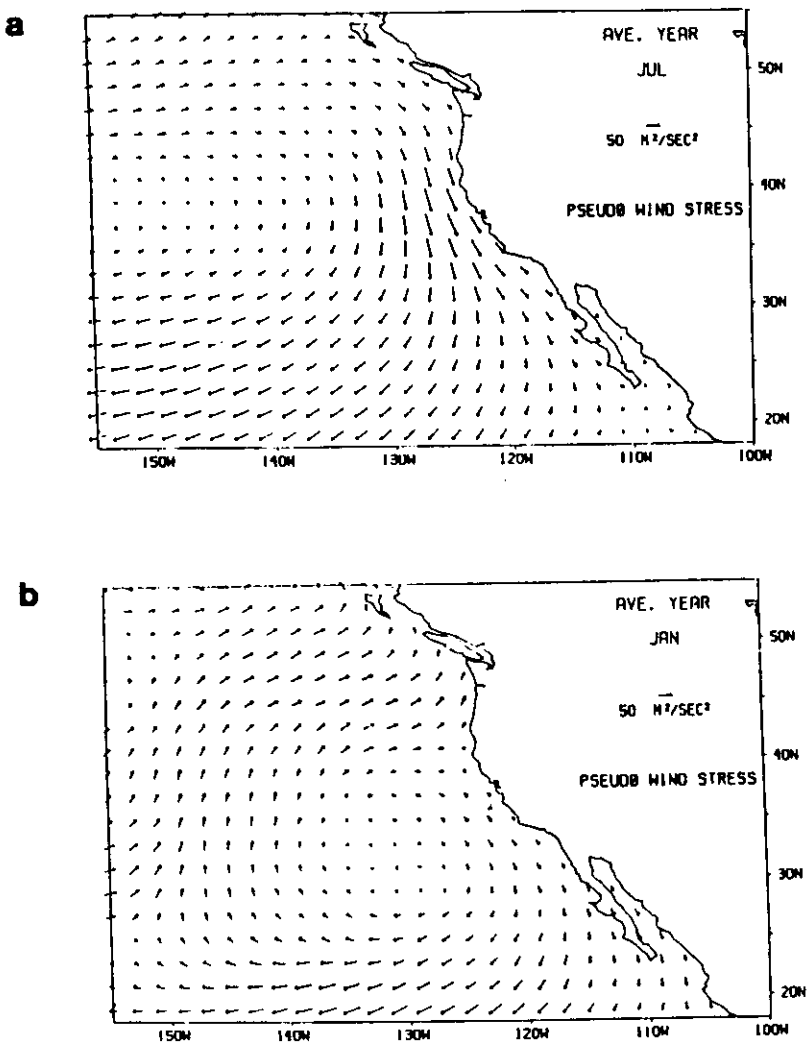

Fig. 2. Long-term averaged pseudo wind stress for (*a*) July and (*b*) January.

agating disturbances in the sea level variability along the western coast of North America has been made evident by the works of *Enfield and Allen* [1980] and *Chelton and Davis* [1982]. As was argued by *Moore and Philander* [1977] and *Clarke* [1983], some of this energy can be accounted for by coastal Kelvin waves generated when an easterly propagating equatorial Kelvin wave reaches the coast. In order to include this mechanism, our model was forced through its southern boundary near the coast by imposing the results of a wind-forced, reduced gravity equatorial model [*Kubota and O'Brien*, 1988]. Kubota and O'Brien's model domain includes the equatorial Pacific from 20°S to 20°N and was run from January 1961 through December 1984. Values of U, V, and H were taken from this model along a band of 15° of longitude at latitude 18°N every 6 days. A forced boundary effectively behaves as a closed boundary for incoming waves; i.e., waves reflect on it. To minimize the contamination of the interior by possible reflections on the southern boundary (for example, from β-refracting Rossby waves propagating to the southwest), it was decided to keep most of the southern boundary open and force through only a small portion of the boundary. The band had to be wide enough, however, to allow the propagation of coastally trapped waves, i.e., a small portion of the boundary but wider than the Rossby radius of deformation; 15° seemed a good compromise (Figure 3). The data were linearly interpolated in space (from one fourth to one sixth of a degree) and in time (from 30 to 20 min) to the resolution of our model.

3. Results

3.1. *Locally Wind-Forced Model*

3.1.1. *General overview of model results.* Figure 4 shows a typical result from our locally forced model, it corresponds to a snapshot at day June 21, 1965. The most conspicuous feature away from the coast is the general decrease of upper layer thickness (ULT) from west to east and its associated equatorward current. This of course is an expression of the dominating Sverdrup balance that determines the mean currents. Typical model currents are about 10–20 cm/s. Near the coast and to the north of 45°N, the ULT is shallower than the initial depth (20 m). At the coast this is an indication of the prevailing equatorward wind stress and associated large-scale coastal upwelling. In the northern region, this upwelling is most probably due to Ekman pumping due to a positive wind stress curl. Figure 4 corresponds to a typical summer situation, i.e., upwelling favorable winds. It shows that along the coast, the strongest upwelling occurs from 40°N to 50°N. A strong feature of our model is the splitting of the equatorward current at

Fig. 3
model u
from a
boundar

about 3
rent. U
rent co
the bou
nia cou
separat
to yea
change
The
are sho
domina
Deepes
where
the eas
sure gr
140°N
pressur
geostro
cific gy

Fig. 4
locity (a
represen
tour inte
Note the
in the no

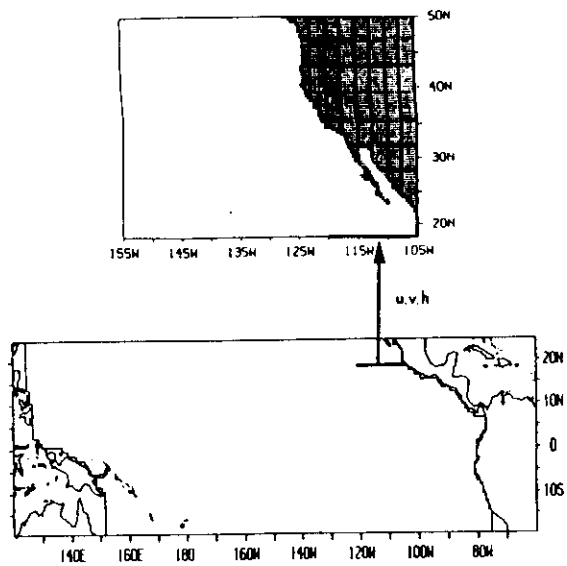

Fig. 3. Domain of the *Kubota and O'Brien* [1988] equatorial model used to force the remote model. U, V, and H values were taken from a 15° transect at 18°N and imposed into our model southern boundary (heavy line).

about 30°N to 125°W into a southward and an eastward current. Upon reaching the boundary, most of the eastward current continues south, but some turns north and flows along the boundary at the California bight, reinforcing the California countercurrent (see also Figure 6). The position and axis of separation change somehow through the year and from year to year, but the fact that the main equatorward current changes direction around 30°–35°N is a very consistent result.

The large-scale characteristics of the locally forced model are shown in Figure 5: the 19-year long-term mean ULT. The dominant wind curl–driven mechanism is evident in Figure 5. Deepest ULT occurs west of 140°W and from 20° to 35°N, where the curl of the wind is most negative. ULT decreases to the east and north of this region, creating an east-west pressure gradient south of about 45°N and east of 140°W. West of 140°N and north of about 25°N there is a general north-south pressure gradient. It is this pressure gradient pattern which geostrophically drives the main gyre in our model (North Pacific gyre).

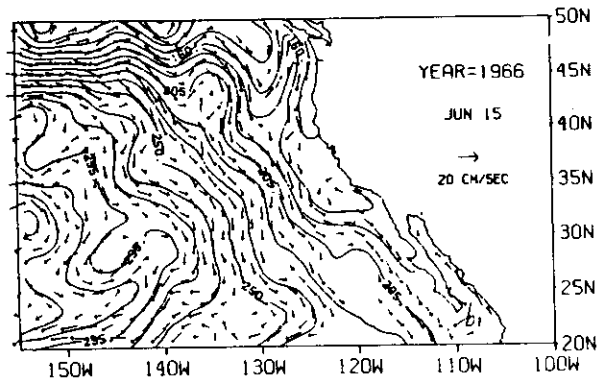

Fig. 4. Upper layer thickness ULT (contours, in meters) and velocity (arrows). Typical output from the wind-forced model. Arrows represent currents scaled according to the key in the figure. The contour interval is 15 m. Currents slower than 1 cm/s are not plotted. Note the area of ULT less than the initial 200 m along the coast and in the northern region.

The ULT is shallower than the initial depth north of about 45°N, where the curl of the wind is prevalently positive, and along the coast. Maximum upwelling occurs at 40°N consistently with the latitude of maximum northwesterly winds in summer. Conspicuously, the region of maximum upwelling is not right at the coast but a few degrees from it. This is an indication of the persistence of a negative pressure gradient just at the coast which drives the coastal interior countercurrent.

3.1.2. *Seasonal variability.* We use 1966 as a typical year to describe the seasonal variability in our model. Four months, representative of the four seasons are shown in Figure 6. Figure 6*a* shows the ULT and velocity for March 1966. In this season, the northwesterly winds at the coast strengthen and the regions of upwelling begin to develop all along the coast with a maximum at about 45°N. The eastward sweep of the southwesterly currents is evident at 30°N, 121°W, but most of the easterly current turns south along the coast without forming a gyre. The current along the coast is equatorward. There is a large gyre circulation near the coast from 40°N to 50°N due to the presence of an elongated region of relatively higher ULT. This is due to a downwelling event from the previous year. By June (Figure 6*b*), northwesterly winds are strong around 45°N, and strong upwelling and equatorial currents have developed in the north. Near the southern California bight, the upwelling is already relaxing, and some countercurrent is beginning to develop. The splitting point for the equatorward current has moved some degrees to the west. By September (Figure 6*c*), the strong upwelling has ceased and the ULT minimum advected away from the coast. There is a well-developed negative pressure gradient near the coast, and the interior countercurrent is also well established from southern Baja California to the northern part of the domain with strong poleward current around 41°N where the negative pressure gradient is strongest. The December results (Figure 6*d*) show that the poleward countercurrent persists only north of 30°N where the southern section of the California eddy marks the southern reach and the eastern turning of the equatorward current. The initial split of the equatorward current is now further west at about 128°–129°W, and a new splitting region is developing where the southern section of the California eddy is forming. A strong low-ULT area persists at around 40°N, but it has propagated westward some degrees. An interesting large eddy has formed at the tip of Baja California and is detaching from it and propagating westward.

There are two areas of preferential eddy formation, at the mouth of the Gulf of California (20°N) and at the region of

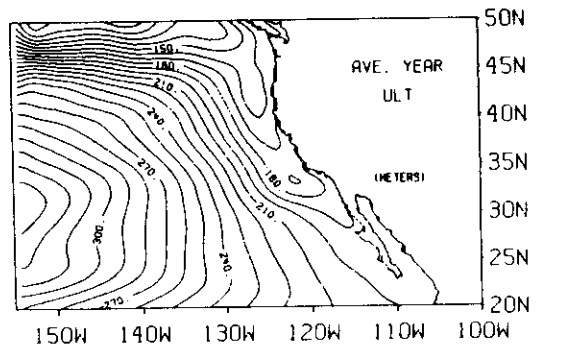

Fig. 5. Long-term averaged ULT (in meters) from the local wind driven model. The contour interval is 10 m.

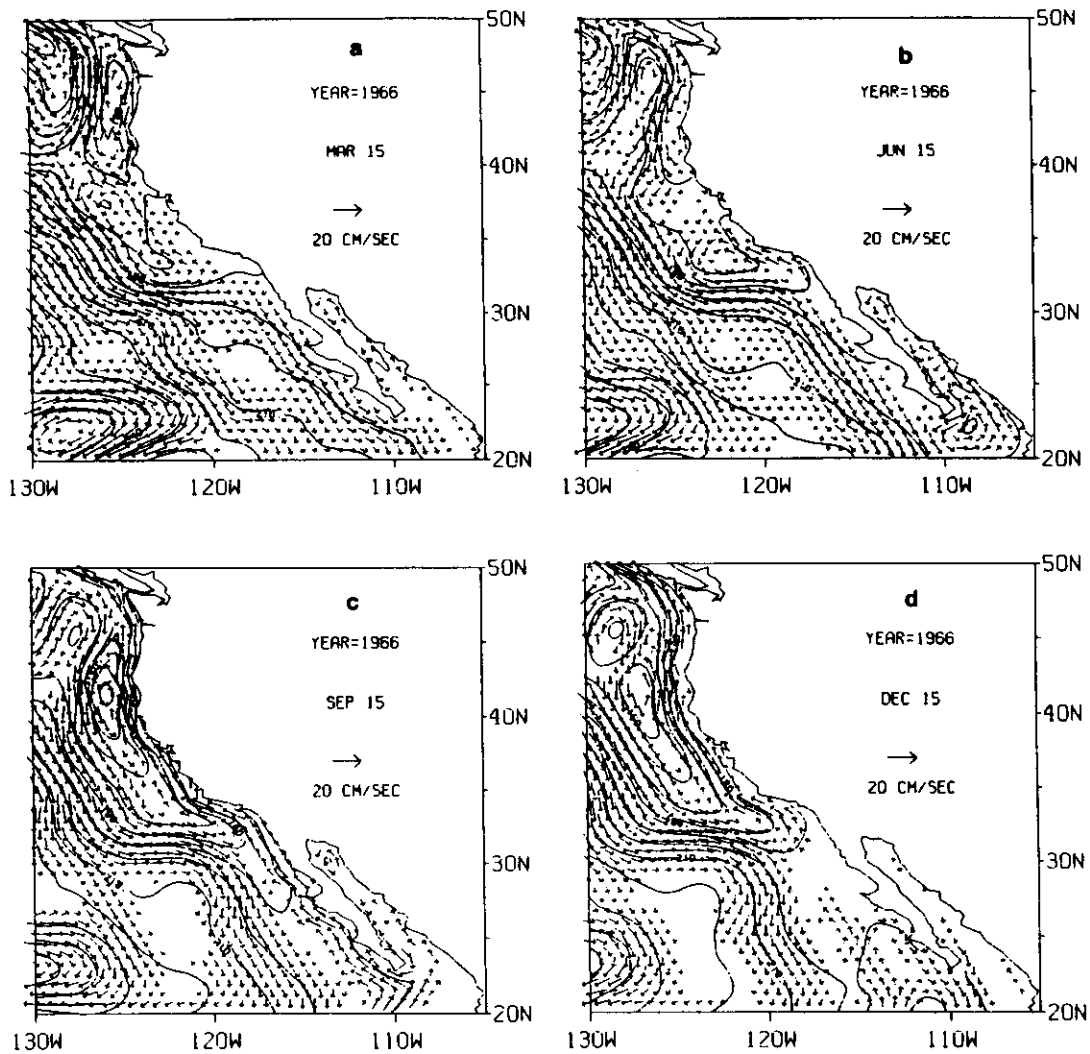

Fig. 6. Upper layer thickness (contours, in meters) and velocity (arrows) from local model for March 15, 1966. Only the western 25° are plotted. Note the eastward sweep of the southeasterly currents at around 32°N, 120°W. The contour interval is 10 m. Arrows are scaled as key in figure. (*b*) Same as Figure 6*a* but for June 15, 1966. Maximum equatorward current has moved westward compared with that in Figure 6*a*. (*c*) Same as Figure 6*b* but for September 15, 1966. The countercurrent is well developed all along the coast. Note that the splitting of the southerly current has propagated westward. (*d*) Like Figure 6*a* but for December 15, 1966. The bifurcation that was near the coast in March has propagated to about 130°W, and a new splitting has developed. The countercurrent has retreated to north of the California bight. Note that a large eddy has developed and is detaching from the tip of Baja California.

strong wind reversal (40°N). To analyze this point, long-term-averaged monthly anomalies of ULT with respect to the long-term annual mean are plotted in Figure 7 (only every other month is shown).

Positive anomalies along the coast occur from October to March, while negative anomalies occur from April through August or September. The larger negative anomaly is in June; ULT starts increasing until it reaches the maximum in January. From January to June, the ULT decreases. It is clear from Figure 7 that this relaxation is not in the way of a standing wave at the coast but by westward relaxations of the disturbance. Although this process happens all along the coast, as was mentioned before, two regions seem dominant. Figure 7 clearly shows most of the annual energy emanating from 40°–45°N and from around 20°–25°N. The 20°–25°N waves are due to the effect of the gulf. These two source regions coincide with what has been identified by other authors (e.g., *Cummins et al.*, 1986; *White and Saur*, 1981]. An interesting feature is the absence of waves of significant amplitude emanating from the latitude band 30°–35°N. This later characteristic has been noted before [*Cummins et al.*, 1986]. Figure 7 also makes evident the existence of a critical latitude, south of which waves can propagate westward in the form of free Rossby waves but north of which they present a westward decaying component (see, for example, *McCreary and Kundu* [1985]; *McCreary et al.*, 1987]. The theoretical critical latitude ($\theta_c = \tan^{-1}[(g'H)^{1/2}/2\sigma a]$ [*McCreary et al.*, 1987]) for an annual frequency ($\sigma = 2\pi/1$ year) is around 40°N. *Grimshaw and Allen* [1988] found that when the boundary is sloping, the critical latitude moves closer to the equator. Apparently, this is the case in our model, as the critical latitude seems to be around 35°N (Figure 7). This probably is the reason why north of 35°N there is not a clear wave activity west of 130°N as there is south of this latitude.

3.1.3
the co
structe
The wi

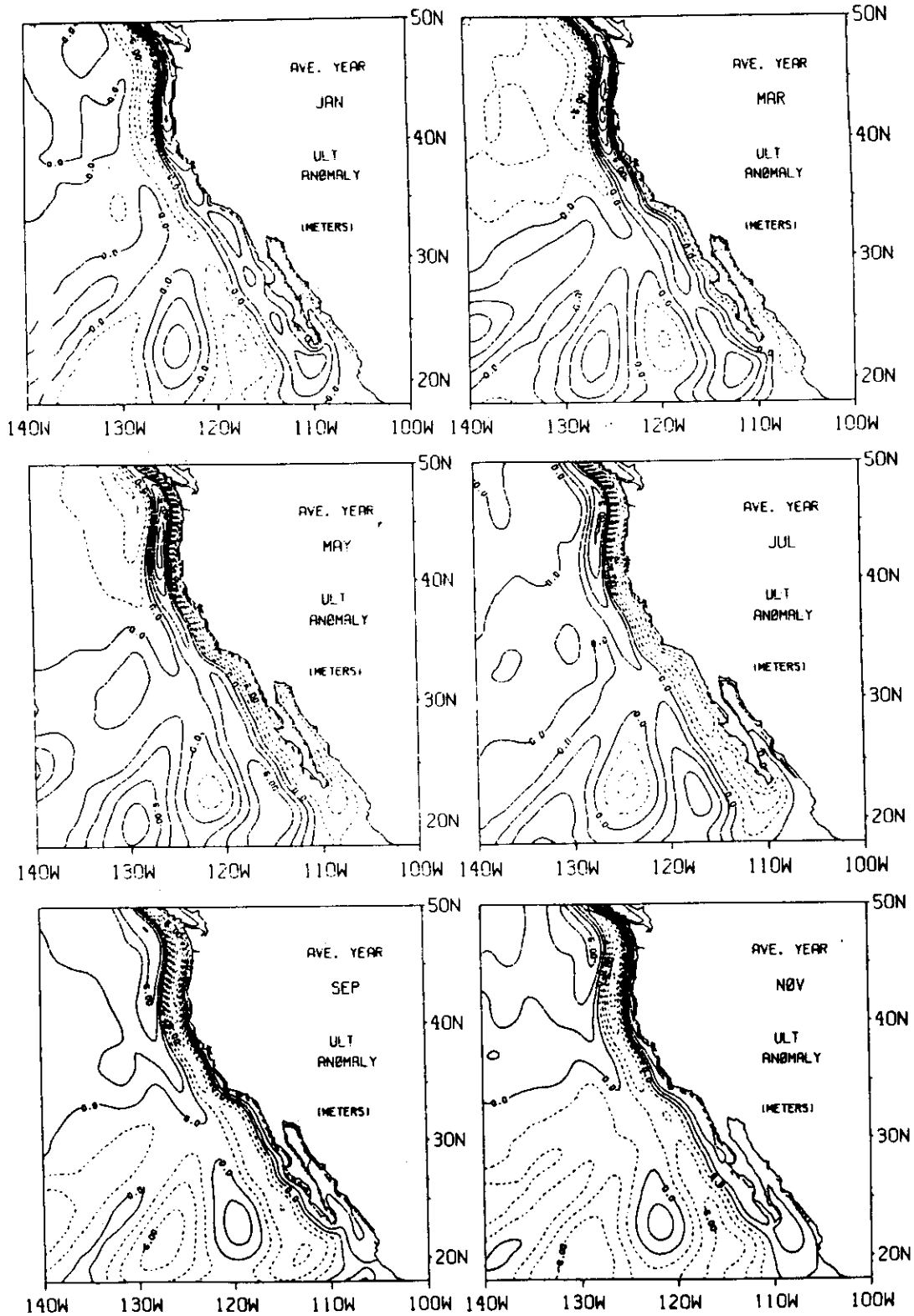

Fig. 7. Long-term monthly ULT anomaly from the local model. The long-term average was subtracted from the long-term monthly means. The contour interval is 2 m. Strongest anomalies were generated near 40°N and from the mouth of the Gulf of California. Note the westward propagation of anomalies through the year.

3.1.3. *Large-scale variability of ULT and wind stress along the coast.* Time series of ULT and wind stress were constructed for the 15 stations shown in Table 2 (see Figure 1). The wind series are of the alongshore component parallel to the general direction of the coast at each station (Table 2). Figures 8*a* and 8*b* show the monthly averaged time-latitude plots for winds and ULT, respectively. The dominance of an annual cycle is evident. There are strong equatorward winds

TABLE 2. Stations Used in the Alongshore ULT Variation Analysis

Station Number	Station Name	Key	Latitude, °N	Distance From CSL, km	Direction of Coast, deg
1	Cape San Lucas	CSL	23.0	0	0
2	San Carlos	SC	24.1	249	36
3			26.1	537	43
4	Sevastian Viscaino Bay	SVB	27.6	797	90
5			29.3	995	34
6	Ensenada	EN	31.5	1224	62
7	San Diego	SD	32.7	1397	62
8	Long Beach	LB	33.6	1566	24
9	Avila Beach	AB	35.2	1878	56
10	San Francisco	SF	37.8	2234	40
11			39.3	2468	70
12	Crescent City	CS	41.8	2727	73
13	South Beach	SB	44.1	3003	90
14	Astoria	AS	46.1	3208	90
15	Neah Bay	NB	48.4	3481	69

*Directions are in degrees clockwise from east.

during summer and weak equatorward or (in the north) even poleward winds in winter. The strongest equatorward winds occur between 35°N and 40°N, and the strongest poleward winds occur at 48°N. The long-term mean wind strength versus latitude (Figure 9*a*) shows a net annual poleward wind (≈ 2 m^2/s^2) only for the two northern most stations. The variability represented by the average deviation from the mean [i.e., $1/N \sum |X_i - \bar{X}|$] in Figure 9*b*, increases from 16 m^2/s^2 at 48°N to a maximum of 22 m^2/s^2 at 40°N and drops sharply to about 6 m^2/s^2 at 35°N. The variability stays more or less constant from 35°N (the California bight) to the south.

Direct wind-driven Ekman drift and associated upwelling are manifest in the ULT time series (Figure 8*b*). The ULT is at all times and latitudes less than the initial depth of 200 m, which is indicative of the prevalence of equatorward winds along the coast. During summer the strong southerly winds in the north produce a maximum north-south ULT gradient with a difference of almost 50 between the northern and southernmost stations. In winter the difference is reduced to about 15–20 m owing to the relaxation and reversal of the winds. In contrast to the winds, variability of ULT (Figure 9*b*) increases monotonically from south to north, although there is a change in its gradient at the latitudes where the wind stress variability increases (i.e., 35°N). This fact is in accordance with the existence of poleward propagating waves. ULT variability generated at a given latitude contributes to that latitude's energy budget and to that of all stations to the north. The form of the long-term mean coastal ULT as function of latitude (Figure 9*a*) is consistent with the mean annual sea elevation determined by steric height as presented by *Reid and Mantyla* [1976].

There is some interannual variation in the winds and ULT series. For example, for the winters of 1968–1969, 1969–1970, and 1977–1978 the positive wind anomalies extend further

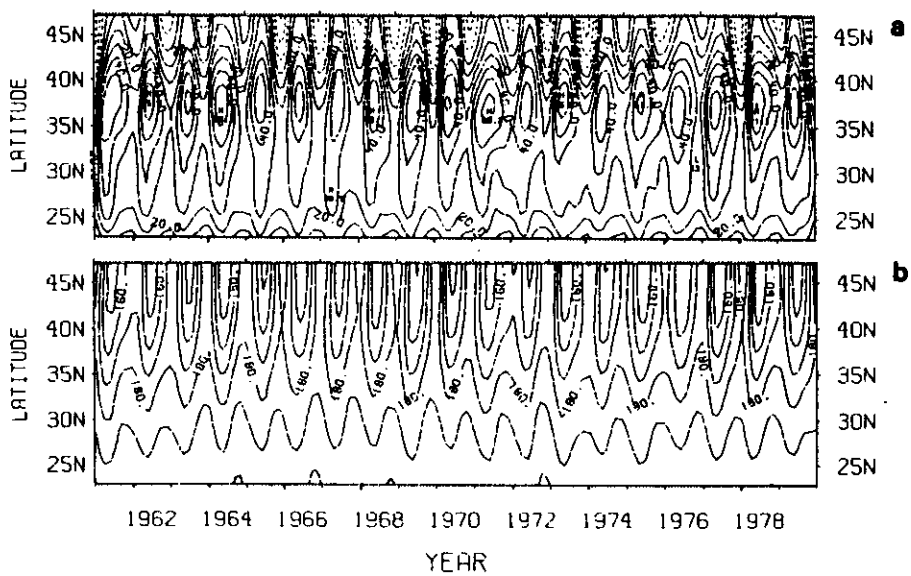

Fig. 8. (*a*) Time-latitude (alongshore) plot of the projection of the pseudo wind stress vector to the general direction of the coast. Units are m^2/s^2; contour intervals are 10 m^2/s^2. Continuous line (positive) contours represent equatorward winds, (*b*) Time-latitude plot of ULT from the local model, Units are meters; the contour interval is 10 m. These plots were constructed from the time series at the stations indicated in Table 2 and marked in Figure 1.

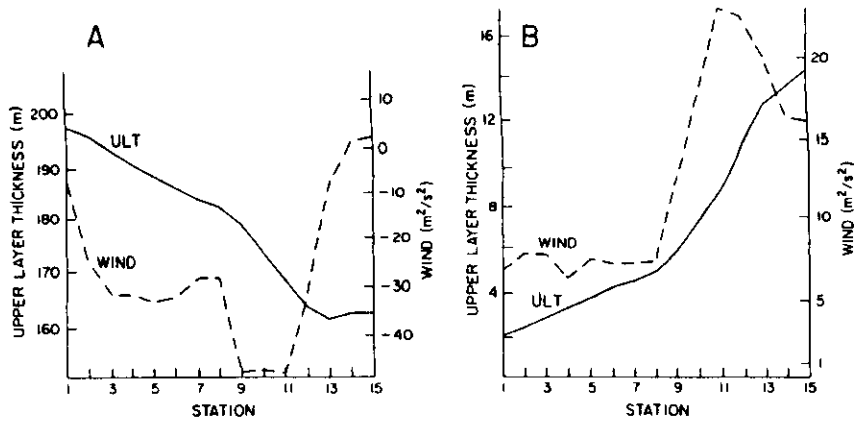

Fig. 9. (*a*) Long-term mean ULT (solid line) and alongshore wind magnitude (dotted line) on the alongshore transect from stations 1 to 15. Numbers identify the stations along the coast according to Table 2. Units are meters for ULT and m^2/s^2 for wind. (*b*) Same as Figure 9*a*, but for the averaged deviation (i.e., $1/N \sum_{i=1}^{N} |X_i - \bar{X}|$).

south than the average, and for 1973–1974 the duration of positive wind is longer than average. The ULT and wind interannual variation are plotted in Figures 10*a* and 10*b*. These long-term variations were calculated using a 13-month running mean filter in the time series. Positive anomalous wind events (i.e., weaker equatorward winds or stronger than average poleward winds) are present mainly at 1965–1969, 1974, and 1978. All these years are characterized by positive anomalies of ULT (i.e., deeper than average). The occurrence of several continuous years of positive anomalies in the winds (1965–1969) produces a relatively strong positive ULT anomaly at the coast. On average, the ULT is deeper for the 1970s than for the 1960s. The positive anomalous event in this wind-driven model ULT does not seem to be particularly well correlated to identified El Niño events.

To investigate the form of the ULT response to the applied winds, we calculated cross-correlation matrices from the latitude-time series. Figure 11 shows the cross-correlation matrix between station 1 (Cape San Lucas) versus all other stations to the north for ULT (Figure 11*a*) and winds (Figure 11*b*). From Figure 11*a* it is evident that there is high correlation at all latitudes. The maximum correlation shifts to negative values (i.e., events happening first in the south then in the north) as the station separation increases. The orientation of the ridge of maximum correlation indicates a propagation of the ULT signal to the north; however, the implied speed (average approximately 3200 km in about 2 months) is too slow to represent coastal wave propagation. When the ULT cross-correlation matrix is compared with that of the wind (Figure 11*b*), it is clear that the propagation implied in Figure 11*a* is due to a direct local response of ULT to slowly propagating wind patterns. Indeed, both correlation matrices are qualitatively very similar, with the actual values smaller for the winds than for the ULT series owing to a shorter decorrelation scale for the former. The structure of the wind correlation matrix (and that of ULT) indicates a slow propagation of events from south to north. Figure 11*a* represents the overall (all year) correlation matrix. *Halliwell and Allen* [1987],

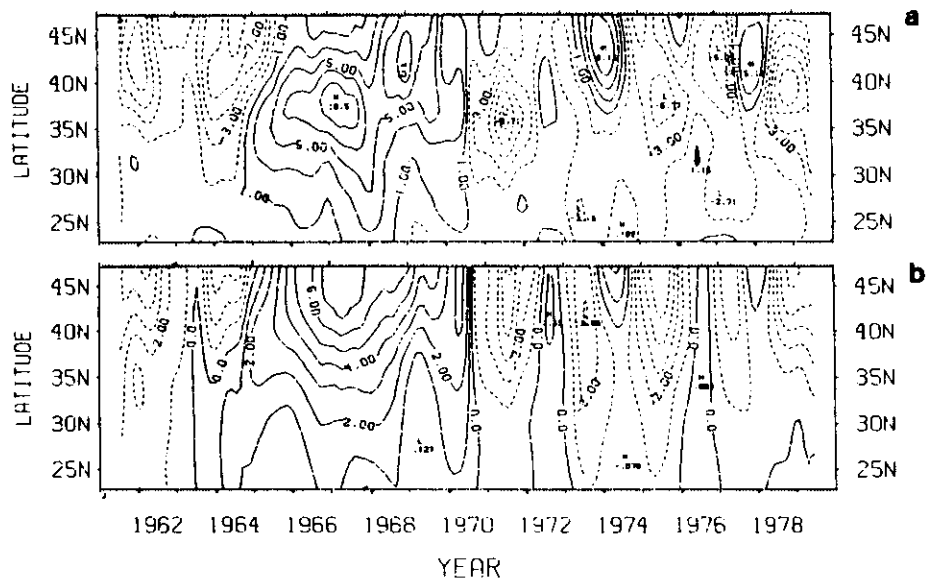

Fig. 10. Latitude-time plot of interannual variability for (*a*) wind stress and (*b*) ULT from the local model. Positive contours indicate stronger than average poleward winds and deeper than average ULT. Units are m^2/s^2 for winds and m for ULT. Contour intervals are 2 m^2/s^2 and 1 m for the wind and ULT, respectively.

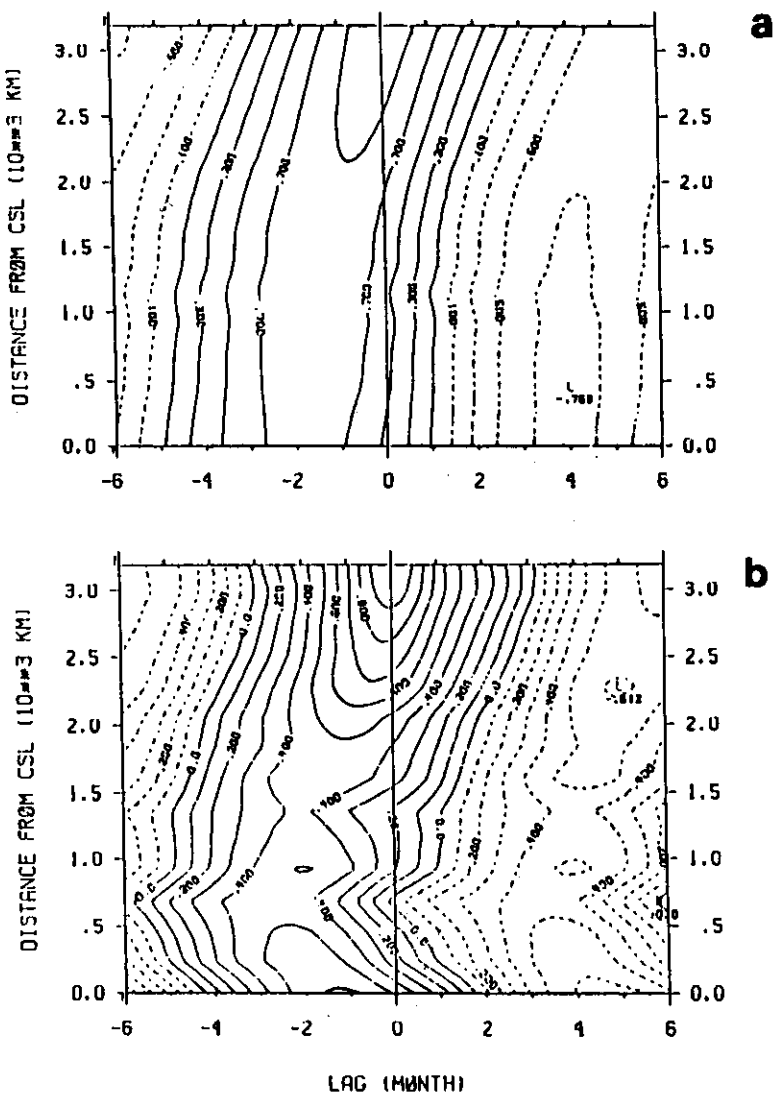

Fig. 11. Cross-correlation matrix of (*a*) ULT and (*b*) winds between time series at station 15 and all other stations (Table 2). The scale at left is the distance in thousands of kilometers from Cape San Lucas, southern Baja California (station 1). Postive lag means station 15 leading.

from an analysis of wind series (higher frequencies) along the western North American coast, concluded that there is poleward propagation of wind events only during the summer months, with equatorward propagation for the winter. The fact that the overall correlation indicates poleward propagation is probably due to the dominance of the more energetic summer events. *Brink* [1987] acknowledges the difficulty of discriminating between observed locally forced variability and that due to remote forcing. Because of the large scales of the wind patterns, a high correlation between local wind and sea level (SL), for example, does not necessarily mean that the SL is locally driven; rather it could be due to a SL forced by winds at a remote station, which in turn is coherent with the local winds [*Brink*, 1987].

The correlation matrix between ULT time series at station 15 versus the time series of the winds at all other stations (Figure 12) demonstrates the fact that the ULT is best correlated with the winds earlier in time (at negative lags) and with stations further south of it. In particular the maximum at about 2500 km from Cape Sun Lucas shows that station 15 ULT series is best correlated with the wind at about 500 km to the south and earlier in time. In Figure 13 we plotted the maximum correlation matrix (regardless of the lag) between the ULT time series at all the stations and the time series of the winds. For example, ULT of station 15 (3200 km from Cape San Lucas) shows a correlation of about 0.8 with the time series of the wind at the same station (value at right top corner of plot), but it has a stronger correlation (0.9) with the winds about 500 km to the south of it. A maximum along the 45° line would indicate a direct ULT response to local wind with no propagation. The presence of a ridge below and mostly parallel to the 45° line indicates that ULT correlation to the winds further south, at a fixed distance, occurs at all the stations. This characteristic is again just the result of waves spreading information only in the poleward direction, i.e., the direction of free wave propagation. Wind stress variability leading coastal sea level variability in time and space has been found by several authors [e.g., *Halliwell and Allen*, 1987; *Allen and Denbo*, 1984]. *Halliwell and Allen* [1987] showed the sea level response at a given location along the western North American coast to be most highly correlated with the winds at lag distances 300 to 400 km equatorward of that location.

C1

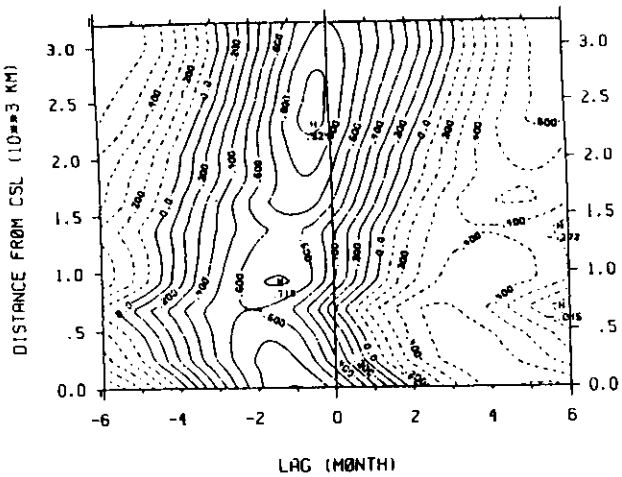

Fig. 12. Cross-correlation matrix between time series of ULT at station 15 versus time series of wind at all other stations. Positive lag means that the ULT series leads the wind. Note the the maximum correlation of ULT at station 15 is with the time series of the wind a few days earlier and about 500–600 km to the south.

3.2. *Remotely Forced Model*

As explained in section 2, a second model was run in which the easternmost 15° of the southern boundary were forced by imposing values of U, V, and H taken from an equatorial model. The results, described in this section, are qualitatively different from those of the locally forced model. The most conspicuous difference between the long-term mean of the remote model and the local model is the absence of an east-west ULT gradient. This of course is not surprising, since the remotely forced model lacks the mechanism for its generation, i.e., the large-scale negative wind curl. The basic mechanism driving this second model is graphically illustrated in Figure 14. This figure shows snapshots of ULT and currents at 6-day intervals, from January 15 to February 3. The figure presents the results for 1962, the second year of integration. An upwelling event has entered the domain through the southern boundary, and by January 15 the southernmost edge of this event has reached 27°N. Six days later, at January 21, the low-ULT signal has propagated north to about 35°N (Figure 14*b*); it reaches 43°N by January 27 (Figure 14*c*) and 50°N by February 3 (Figure 14*d*). At the same time, a downwelling event that was inside the gulf in its western side at January 15 propagates around it and north along the coast, reaching 35°N in the 24-day interval. The offshore decaying scale and speed of propagation indicate that this propagation corresponds to first baroclinic mode coastal Kelvin waves. The theoretical offshore scale, given by the baroclinic Rossby radius of deformation $(g'H)^{1/2}/f$ is approximately 30 km and 10 km for latitudes 24° and 40°N, respectively, and the speed of propagation $(g'H)^{1/2}$ is about 2.5 m/s. Also shown in Figure 14 are the upwelling- and downwelling-associated geostropic currents. An upwelling event (negative pressure gradient at the coast) drives an equatorward current, while poleward currents are associated with downwelling events.

The succession of annual upwelling and downwelling events, appearing at the southern boundary and propagating along the coast, constitutes most of the response of the remotely forced model as proven by the ULT cross-correlation matrix (Figure 15). The slope of the maximum correlation ridge, in contrast to that of the locally forced model (Figure 14), does indicate a fast propagation in agreement with the theoretical Kelvin wave speed.

In the annual and interannual time scale sense, the coastal

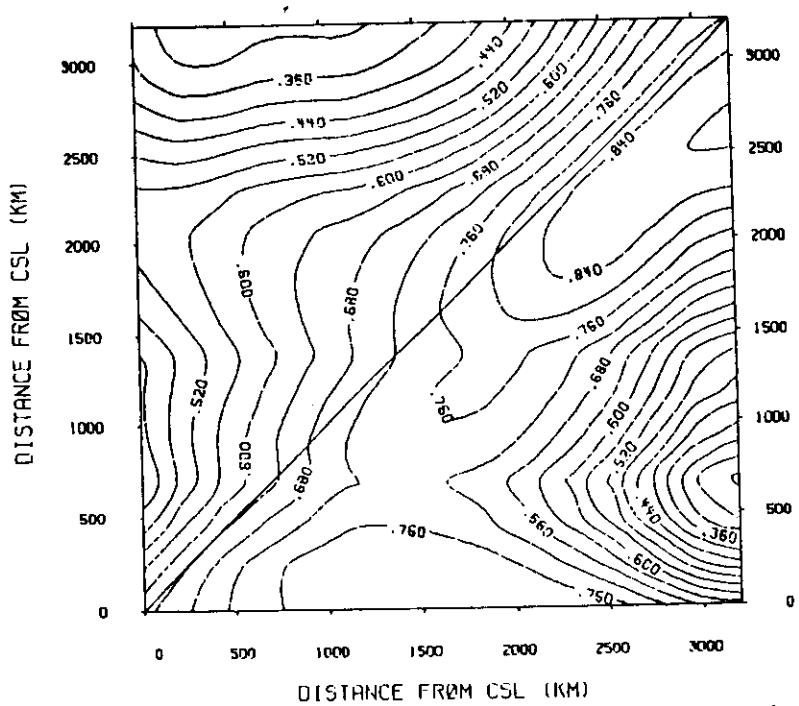

Fig. 13. Maximum correlation matrix between ULT and wind time series. The figure displays the maximum correlation, regardless of time lag, occurring between time series of ULT (abscissas) and the wind (ordinates). The 45° line marks the maximum correlation between time series of ULT and the wind at the same station. For example, station 15 (northernmost) shows a correlation of about 0.8 with the time series of the wind at the same station (value at the top right corner of plot) but a maximum correlation of 0.9 with the wind about 500 km to the south of it.

62

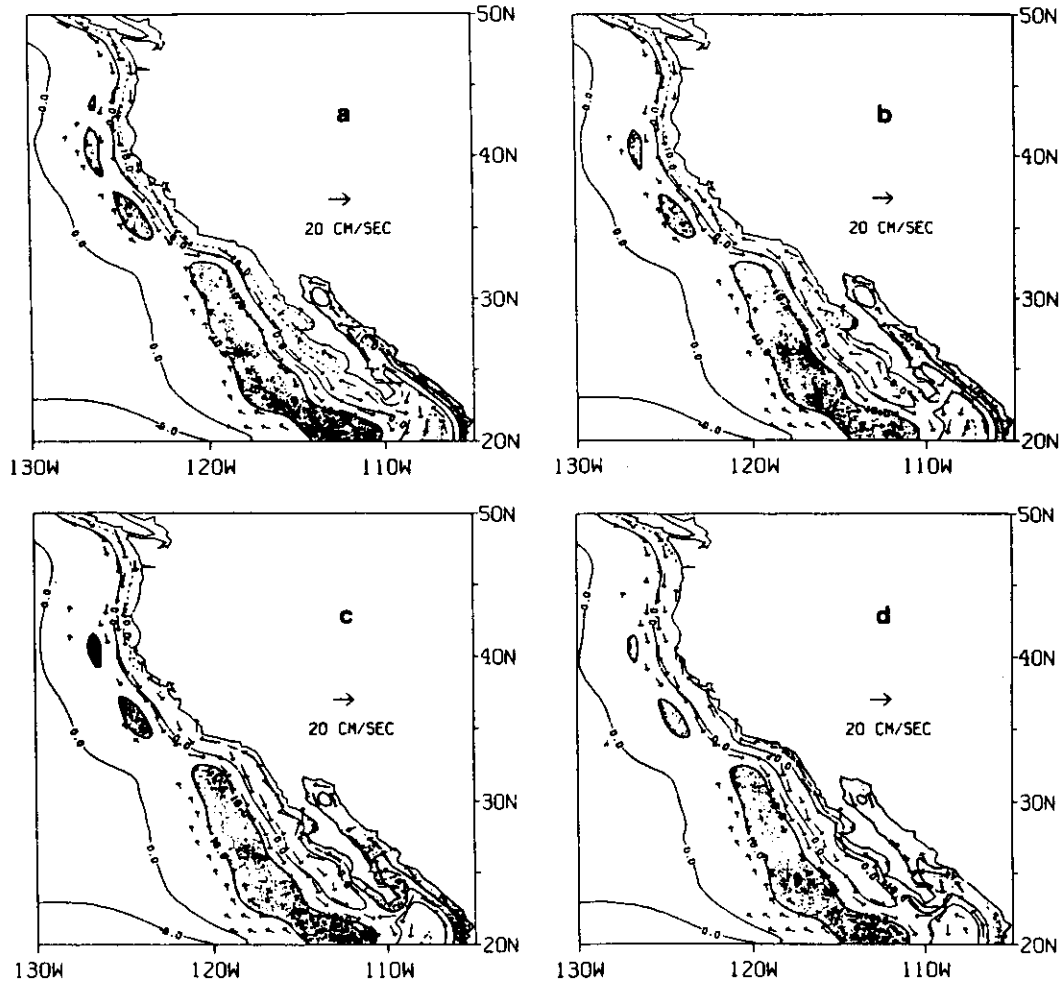

Fig. 14. Upper layer thickness minus 200 m (contours) and velocity (arrows) from the remotely forced model. Figure shows four snapshots of the results 6 days apart; (*a*) January 15, (*b*) January 21, (*c*) January 27, and (*d*) February 3. Arrows are scaled according to the key in the figure. Areas of ULT deeper than 10 m and shallower than −10 m are shaded dark and light, respectively.

propagation is very fast. The difference in speed of propagation between coastal Kelvin waves and westward annual and interannual Rossby waves is such that from the point of view of the latter, upwelling and downwelling disturbances appear almost simultaneously all along the coast. Figure 14 shows a downwelling band a few degrees west of the coast. This event was at the coast the previous year. The time interval represented in Figure 14 is not large enough to show any propagation of this band, but by the latitudinal variation in the position and form of the disturbance, it can be identified as a westward propagating Rossby wave. Note the decrease in separation between the downwelling pattern and the coast from south to north. Once separated from the coast, the anomalies continue westward propagating in the form of free waves. Figures 16*a* and 16*b* show two representative results from the remotely forced model. Both figures represent snapshots of ULT anomalies for February 9; Figure 16*a* is for 1968, and Figure 16*b* is for 1975. The patterns are very similar: meridional bands of positive and negative anomalies extending over the whole domain with its magnitude decreasing to the north and west. In both figures, for 1968 and 1975, there is a large positive anomaly more or less at the center of the domain that corresponds to the large positive anomalies occurring at the coast in 1965 and 1972, respectively (i.e., El Niño events). The different speed of propagation with latitude is again evidenced by the sloping of the latitudinal bands. In Figure 16*a* a strong negative anomaly is observed at about 120°–130°W; this corresponds to the strong downwelling event (anti–El Niño) occurring at the coast in 1973. The weak positive anomaly in the western region, starting at the western boundary at around 30°N and 40°N in Figure 16*a* and 16*b*, respectively, corresponds to anomalies that were at the coast in 1963 and 1969, respectively.

All the information contained in these plots and in the remote model in general comes through only 500 km of the southern boundary, and this information (at least its low frequency) in turn is primarily of equatorial origin and more specifically generated at the western equatorial region by relaxation of the westerly winds. These results show a possible dynamic mechanism for the connection of equatorial El Niño events with north Pacific El Niños, i.e., an oceanic teleconnection.

The degree of correlation between our results and observed time series along the coast is analyzed in the next section.

63

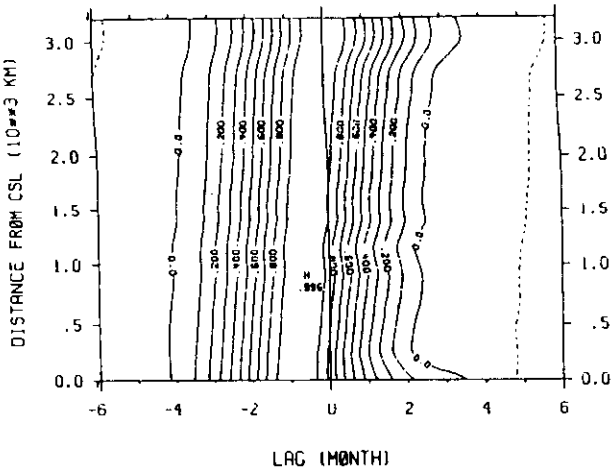

Fig. 15. Cross-correlation matrix of ULT time series at station 15 versus all other stations along the coast, from the remote model (see Table 2).

3.3. *Intercomparison of Model and Observations*

Time series of monthly observed sea surface elevation at several stations along the coast were obtained (K. Wrytki, personal communication, 1986). Four stations were used for the analysis: Crescent City, Neah Bay, San Francisco, and San Diego (see Figure 1). These stations were chosen because they have the longest records and represent the latitudinal variation of the area of interest. Lack of a long enough series prevents us from using other stations south of San Diego.

For comparison with observations, model ULT anomaly data were transformed to sea level anomalies by multiplying by the density gradient between the two layers of the model. As an example of the resulting series, Crescent City's observed and model (wind and equatorially forced) calculated SL are shown in Figure 17. The overall visual correlation in phase and amplitude is good in most years. Particularly good agreement of the amplitude and timing of the negative anomalies is evident. For example, the anomalous lows (more than 120 cm) in 1964, 1968, 1970, 1973, 1977, and 1978 coincide in both observations and model.

For a more effective visual comparison, the time series were divided into three parts: (1) the composite long-term monthly means; (2) the low-frequency series, in which the series is low-pass filtered using a spectral filter with a stop frequency of 1 cycle/year and a pass frequency of 0.5 cycles/year; and (3) the high-frequency series, obtained by subtracting the low-frequency series from the total series.

Strong similarities between modeled and observed seasonal patterns are revealed. For San Diego, both model and observed SL composite mean show a minimum in April–May and an increase to a maximum in August–September (Figure 18*a*); the observed SL decreases monotonically from August to the April minimum, while the model SL stays more or less constant until January and then decreases until April. The amplitudes are similar in both cases. For San Francisco and Crescent City, model and observed SL annual cycle (Figures 18*b* and 18*c*) are remarkably similar both in phase and amplitude. There is a minimum of about 8–9 cm in April–May, an increase to a maximum in August–September, and a second maximum in January. The Crescent City secondary peak is stronger than that in San Francisco, and it is well represented by the model. For Neah Bay (Figure 18*d*) the amplitude is bigger, and the minimum and zero crossing are shifted to the right (occur later in the year) both in the observation and the model. The model misses the large peak in December shown in the observed data.

Using steric height anomalies, *Reid and Mantyla* [1976] described the seasonal characteristics of sea surface elevation along the California coast. They showed that contrary to the eastern coast of the United States and further south along the west coast of North America, the SL annual cycle is out of phase with the heating-cooling cycle (i.e., maximum elevation in late summer or early fall and a minimum elevation in winter [*Reid and Mantyla*, 1976]). *Simpson* [1983] showed that the seasonal temperature anomalies in the California Current, which follows the SL seasonal cycle, were produced dynamically (i.e., by upwelling) rather than thermodynamically.

The model seasonal pattern is completely due to dynamical mechanisms. The fact that the model reproduces the annual cycle so well supports the theory that the seasonal cycle of SL along the western part of North America is due mostly to dynamical causes (rather than thermodynamics). This is true even for San Diego, where the seasonal cycle "resembles the annual heating and cooling cycle" [*Reid and Mantyla*, 1976].

For most of the period, there is a high visual correlation between the model and observed high-pass-filtered SL series at the four stations compared (Figure 19). Especially well simulated are the upwelling events in the northern stations (Figures 19*c* and 19*d*). This points to the importance of the equator-

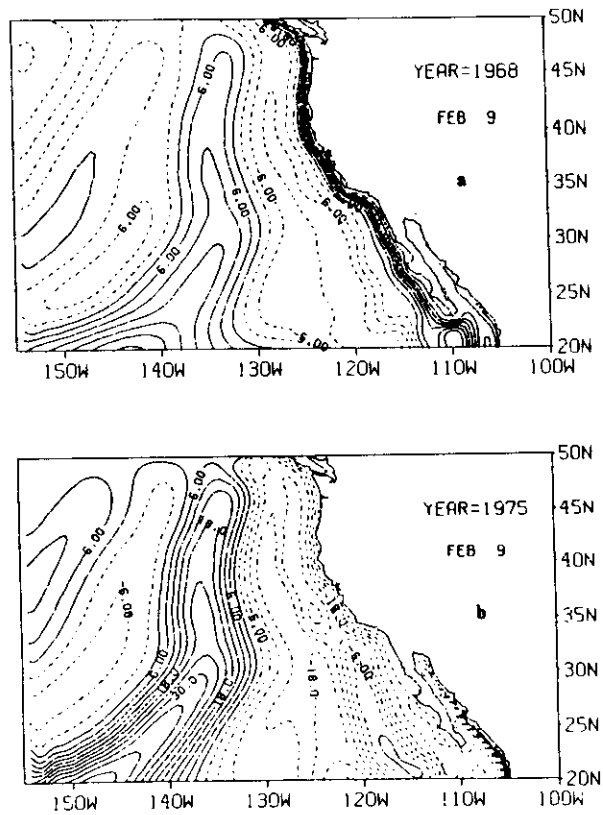

Fig. 16. Typical ULT contours from the remote model. (*a*) Snapshot for February 9, 1968. (*b*) Snapshot for February 9, 1975.

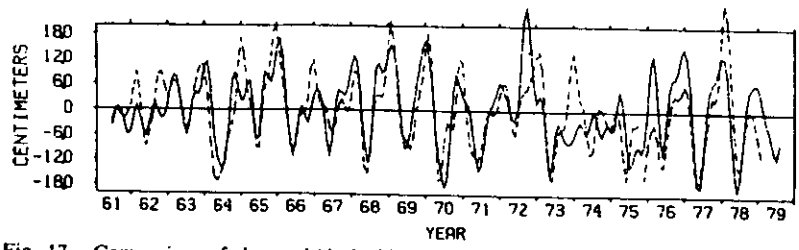

Fig. 17. Comparison of observed (dashed line) and modeled (solid line) for Crescent City.

ward wind forcing in the area and its proper implementation in the model. For most of the years the upwelling events (negative anomalies) have a shorter time scale and larger amplitude than the downwelling events (positive anomalies). This is also reflected in the composite means (Figure 18) and is more evident in the two southern stations, where the two yearly maximums are more pronounced.

For 1974 and 1975 the model results do not follow the observations. The annual cycle in our model breaks down for those years. At least in the San Francisco series (Figure 18*b*), it seems that this perturbation of the annual cycle is also present in the observed series. The amplitude and phase become erratic for 1974 and 1975 in both observations and model. In our model this is the result of the local and remote seasonal cycle becoming out of phase. Indeed, from the separate contributions of each process (Figure 20) it can be seen that the change at 1974 and 1975 is due to the cancelling effect of each signal. Most of the years both the local and remote signal reinforce each other, but for the 1973–1974, 1974–1975 period the remotely forced signal gets out of phase with the wind-driven signal (which maintains its average amplitude and phase) and cancels the total signal. The fact that the observed annual cycle also shows symptoms of disturbance for those years might indicate that the linear cancellation (or reinforcement) mechanism between local and remote signals is a viable one in the California Current region. A complex demodulation analysis of the series around the annual frequency could be useful to further analyze this point.

The amplitude of the annual signal due to each process is of comparable magnitude as seen from Figure 20. From visual comparison it seems that there is more semiannual variability in the model than in the observations. Most of the semiannual variation in our model comes from the equatorial signal. This overemphasis of the equatorial contribution at this frequency is probably the result of the model's lack of some energy dissipation mechanisms (i.e., topography, bottom friction, etc.). Low-pass-filtered time series of SL anomalies are plotted in Figure 21. Again there is a good agreement between model and observations. El Niño events of 1964, 1965–1966, 1972, and 1976 reflected in the data as positive anomalies are reproduced by the model. The largest anomaly in both series is at 1972, the year of the strongest El Niño before the 1982 event. For the two southern stations, the amplitude is very similar. A major difference between the two series is the consistently low model SL at 1966–1967, while the observed data show near-zero or even positive anomalies. This is more pronounced at northern stations. Also, the magnitude of the 1972 event seems to diminish to the north as the observations do. It seems from visual inspection that the correlation between observed and modeled low-passed frequency series decreases to the north.

Comparing the contribution to the low-frequency anomalies from both mechanisms (local versus remote) (Figure 22), it is evident that in contrast to the annual frequency, most of the energy in the El Niño frequency band in the region is of equatorial origin.

To investigate this point further and quantify the different contributions, spectral and cross-spectral analysis were performed.

Spectra were calculated for each model (local, remote, and local plus remote) and observations time series at the four stations: Neah Bay, Crescent City, San Francisco, and San Diego (Figure 23 shows the spectra for Crescent City). Standard smoothing in frequency was done using a 13-band-span Hanning window with 26 degrees of freedom [e.g., *Bendat and Piersol*, 1971].

For the local model, the dominant frequency at all the stations is the annual with a smaller but significant peak at the semiannual frequency. The background spectrum is red (i.e., energy increases toward the low frequencies), and only at the annual frequency are the spectra from the local and remote model of comparable magnitude. For the remote model, the energy at the semiannual, annual, and 2- to 4-year cycle frequency bands are of similar magnitude. The background energy, as in the local model, increases toward the low frequencies, but the amplitude is at least an order of magnitude larger. This magnitude dissimilarity results in the local plus remote model spectrum being dominated by that of the remote model, except at the annual frequency. For the semiannual and lower frequencies, the shape and magnitude of the local plus remote spectrum are similar to those of the observations, but for the higher frequencies (higher than semiannual), the energy drops much more in the first than in the later, evidencing the narrower frequency band response of the model.

The spectrum variation with latitude is mainly in the magnitude of the annual peak. The magnitude of the annual peak increases to the north in observations and model spectrum, and as could be expected, its increase in the model is due to an increase in the local wind-driven model.

Coherence square functions (γ^2) and frequency response functions (H) were calculated [see *Bendat and Piersol*, 1971]. At each station the cross-spectrum functions γ^2 and H were computed between the observed SL time series and the SL time series from (1) the remotely forced model, (2) the locally forced model, and (3) the local plus remote model. Figure 24 shows the results for San Diego. As is suggested by the visual inspection for the El Niño frequency band (2–4 years), there is a large coherence square (≈ 0.80) between observed time series and the remotely forced model (Figure 24*a*). For the annual frequency, although still significant, the coherence is smaller (≈ 0.60). For the local model series, the opposite is

Fig. 18

true; there is a
model data at
50%) coherenc
frequency resp
tween two seri
24*b*) it is clear
coherent at th
small ($H \approx 3$)
the observatior
relation betwee
ures 24*e* show
third of the ob
remote model
shows that the
mechanisms. T
while the cohe
Figure 24 show
of the variance
frequency band
nation of local
75% of the vari

This general
quency respon
other stations.
of the variance
and local mod
As hinted by t
the cross-coher
cent City, and
local model the
and the cohere
frequency the c
of a proper dis
phy, bottom fri
is still significa

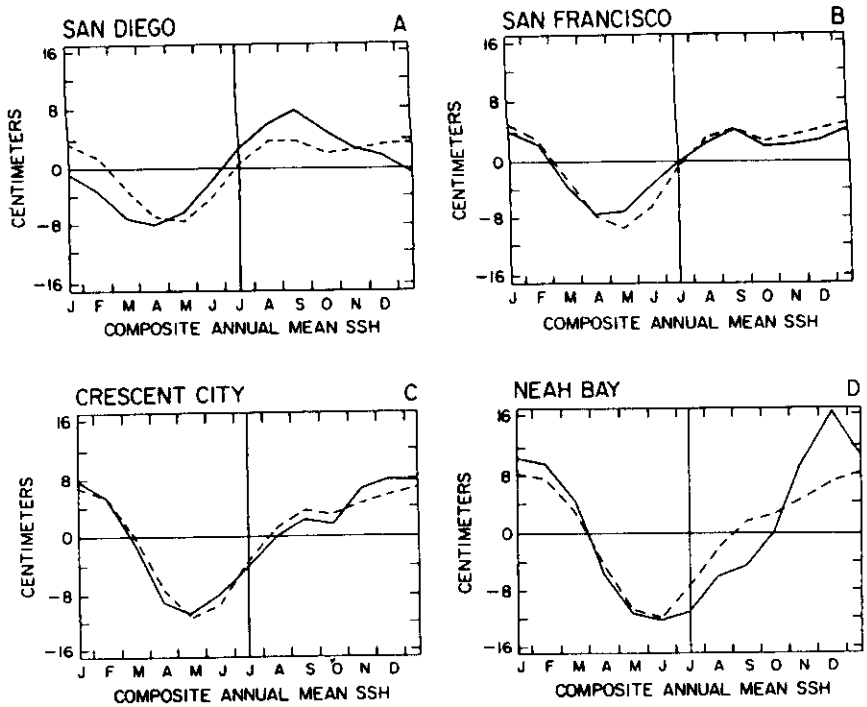

Fig. 18. Composite annual mean sea level anomalies from observations (solid line) and local + remote model (dashed line), for (*a*) San Diego, (*b*) San Francisco, (*c*) Crescent City, and (*d*) Neah Bay.

true; there is a very strong coherence between observed and model data at the annual frequency but no significant (at 50%) coherence at the low-frequency band (Figure 24*b*). The frequency response function represents the power ratio between two series at a given frequency. From Figure 24*e* (and 24*b*) it is clear that though the locally forced model is very coherent at the annual frequency (Figure 24*b*), its energy is small ($H \approx 3$) compared with the energy at that frequency in the observations. In other words, if we assume there is a linear relation between the model output and the observations, Figures 24*e* shows that the local model spectrum is about one third of the observed spectrum. The result from the local plus remote model versus observation comparison (Figure 24*f*) shows that the annual frequency energy is actually due to both mechanisms. The frequency response function is very near 1, while the coherence square is still large (≈ 0.75). In summary, Figure 24 shows that the remotely forced model explains most of the variance (> 75%) in the observations in the El Niño frequency band range, while for the annual frequency a combination of local and remotely forced signal explains also about 75% of the variance.

This general qualitative pattern of the coherence and frequency response function at San Diego is repeated in the other stations. The remote model explains a large percentage of the variance in the low-frequency band, and both remote and local models explain the energy at the annual frequency. As hinted by the visual inspection of the SL anomalies series, the cross-coherence analysis for stations San Francisco, Crescent City, and Neah Bay (not shown) indicates that for the local model the annual contribution becomes more important and the coherence increases to the north, while for the low frequency the coherence decreases again, pointing to the lack of a proper dissipating mechanism in the model (i.e., topography, bottom friction, etc.). At Neah Bay the coherence square is still significant (> 0.40, significant at 90%) for the El Niño frequency band, while for the annual frequency it is up to more than 0.8.

4. Summary of Results

A reduced gravity model that incorporates the geometry of western North America has been used to study the dynamics of the California Current system. Three experiments were implemented: in the first (local model) the model was run using 19 years of wind stress from the Comprehensive Ocean-Atmosphere Data Set; the second experiment (remote model) consisted of forcing the model through its southern boundary using the results of a similar reduced gravity equatorial model; and in the third experiment, both forcings were used simultaneously (local plus remote model). The main objective of this work was to analyze the low-frequency variability of the California Current system in terms of its contributions from remote and local forcing.

Several aspects of the steady large-scale circulation are reproduced by the model. Away from the coast, the basic mean state is determined by the predominantly negative wind curl. The mean flow of the model is in Sverdrup balance; i.e., the negative wind curl is compensated by an east to west pressure gradient that geostrophically drives an equatorward current. The main part of the California Current can be identified with this mechanism.

For the local model, Ekman onshore-offshore transport driven by alongshore winds largely dominates the dynamics near the coast. Seasonal variations in the strength and direction of the winds determine the annual ULT variability there. During spring and summer, strong northwesterly winds drive an offshore Ekman transport that causes the model pycnocline to become shallow near the coast. Associated equatorward geostrophic currents develop, reinforcing the larger-scale (Sverdrupian) equatorward California Current. Weakening of the alongshore winds and actual reversal north of 40° during

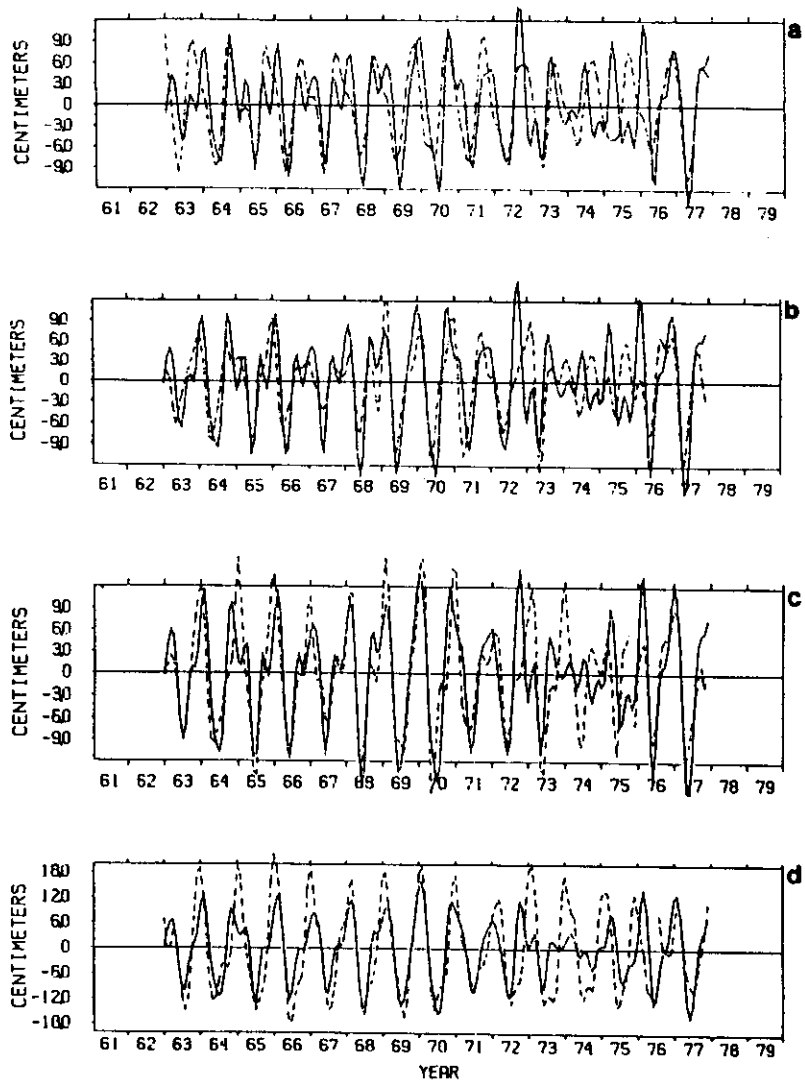

Fig. 19. Comparison of observed (solid line) and model (dashed line) high-pass-filtered (total signal minus low-pass-filtered) series of sea level for (*a*) San Diego, (*b*) San Francisco, (*c*) Crescent City, and (*d*) Neah Bay. A low-passed filter with a pass frequency of $2\pi/2$ years^{-1} and a stop frequency of $2\pi/1$ years^{-1} was used. Note the different scale for Neah Bay.

fall and winter cause the upwelling region near the coast to relax and the coastal countercurrent to develop.

Cross-correlation analysis shows that the ULT signal in the local model slowly propagates from south to north at a speed too slow to represent first baroclinic mode Kelvin waves. It is shown that this motion is in direct response to wind pattern poleward propagation. On the other hand, several features of the ULT-wind correlation analysis suggest that the maximum response in the ULT signal occurs later in time and several hundred kilometers poleward from those of the wind events. This latter phenomenon has been identified as evidence of coastal wave propagation [e.g., *Halliwell and Allen*, 1984].

For the remote model, most of the response along the boundary corresponds to poleward propagating waves. Up-

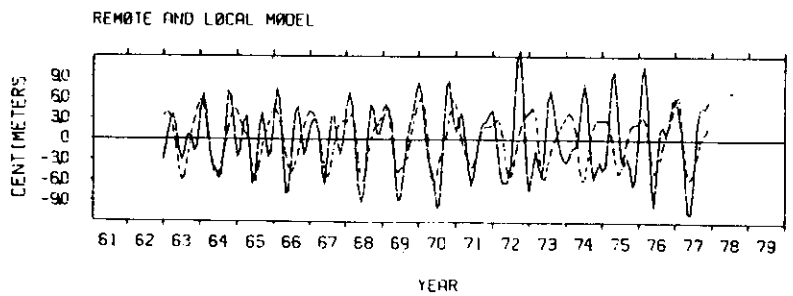

Fig. 20. Comparison of the contribution from the local (dashed line) and remote (solid line) models to the high-pass-filtered sea level anomalies at Crescent City.

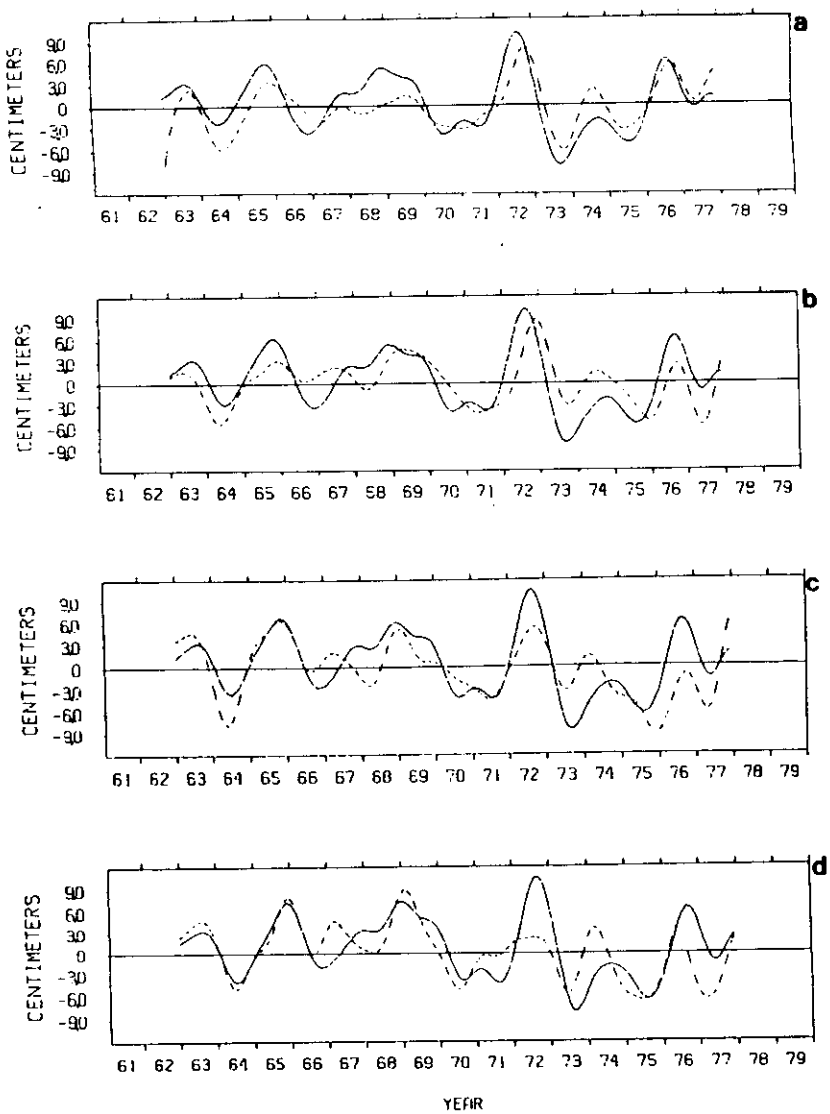

Fig. 21. Comparison of observed (dashed line) and model (solid line) low-pass-filtered series of sea level for (*a*) San Diego, (*b*) San Francisco, (*c*) Crescent City, and (*d*) Neah Bay. A spectral low-pass filter with a stop frequency of $2\pi/1$ years^{-1} and a pass frequency of $2\pi/2$ years^{-1} was used.

welling and downwelling events and associated geostrophic currents succeed each other, appearing at the southern boundary and propagating along the coast with the speed and offshore scale characteristics of coastally trapped first baroclinic mode Kelvin waves.

Time series of sea level data from San Diego, San Francisco, Crescent City, and Neah Bay were used to validate the model. There is good visual correlation between the sea level time series and the scaled model ULT. By separating the low- and high-frequency information for each model, we were able to determine that most of the correlation in the large time scale (El Niño time scale) is due to the signal coming from the equator propagated to the region in the form of coastally trapped Kelvin waves. On the other hand, both models (remote and local) are responsible for the model-observation correlation at the annual frequency.

Spectral and cross-spectral analysis were used to quantitatively corroborate the visual comparison. As was expected, time series from the wind-forced model are very well correlated (high coherence square) with observed sea level data at the annual frequency but are poorly correlated at low frequencies. For the remote model, the coherence is low (but significant) at the annual frequency but high at the low frequencies, which strongly suggests that most of this energy is of equatorial origin. The remote model explains more than 75% of the variance in the low-frequency sea level variability at San Diego and San Francisco. For the two northernmost stations, the coherence between remote model and observations diminishes for the El Niño band while the coherence between the local model and observations increases at the annual frequency.

5. Discussions and Conclusions

The results presented have demonstrated that a significant amount of interannual variability of sea level in the California Current region can be explained by the poleward propagation of Kelvin waves along the coast. This work supports the hypothesis of an oceanic teleconnection as the principal mecha-

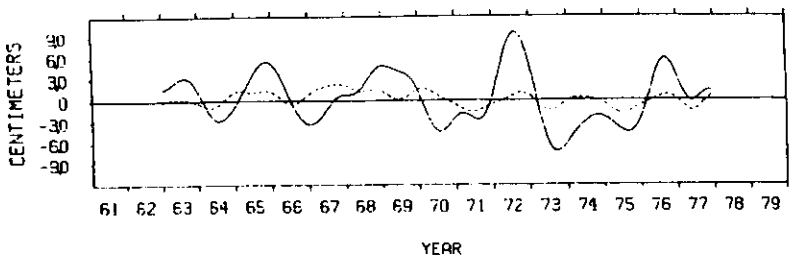

Fig. 22. Comparison of the contribution from the local (dashed line) and remote (solid line) models to the low-pass-filtered sea level series at San Francisco.

nism for the co-occurrence of tropical and mid-latitude El Niño phenomena.

The effect of a basin-wide enhancement of the atmospheric circulation during a tropical warming event (atmospheric teleconnection) is recognized as an important mechanism for augmenting the basic response. However, this latter effect is suggested by this work to be more important for the annual time scale than for the interannual (El Niño) variability (see Figures 20 and 22).

It seems plausible for the local wind driven contribution to become the dominant force for specific events. *Simpson* [1983, 1984*a*, *b*], for example, argued that for the 1982–1983 event, the observations are incompatible with most of the requirements of the theory of coastally trapped waves. Other authors [e.g., *Huyer and Smith*, 1985; *Rienecker and Mooers*, 1986] have concluded that although the initial signals of the 1982–1983 northeastern El Niño arrived by an oceanic path, the initial effects were greatly enhanced by anomalous local atmospheric conditions.

Huyer and Smith concluded that the manifestation of the 1982–1983 El Niño off Oregon was associated with both distant and local causes. They show that the atmospheric forcing became anomalous only after (2–3 months) the initial high sea level developed.

One of the main objections to the oceanic teleconnection hypothesis is the small cross-shelf length scales of the coastal waves ($\approx$ 35 km). *Anderson and Rowlands*' [1976] theoretical work demonstrated how planetary waves lead to a westward broadening of the upwelling fields. *Philander and Yoon* [1982] showed that for long periods (> 200 days) the appropriate offshore scale is not the radius of deformation but the distance a Rossby wave travels in a given time. This broader offshore scale is associated with the existence of a critical latitude defined as $\theta_c = \tan^{-1}[(g'H)^{1/2}/2\sigma a]$, (where σ is the frequency). Poleward of this latitude the waves are β plane Kelvin waves that decay offshore with a e-folding scale of the order of c/f; equatorward of θ_c the waves are offshore-propagating Rossby waves [*McCreary*, 1987]. For periods longer than annual the critical latitude is poleward of the model northern boundary, so that most of this energy leaks offshore.

Our results reflect this condition. Once an upwelling (or downwelling) event has propagated poleward along the coast, a westward shedding of energy occurs (Figure 16). This causes first a broadening of the area of influence of the coastal phenomenon and second an actual export of energy to the model interior. The time scales of these two phenomena are very different. Coastal propagation time scales are of the order of days, while the broadening of the coastal disturbance by planetary waves is of the order of months [*Philander and Yoon*, 1982]. This latter is certainly fast enough to influence the coastal low-frequency El Niño events (2–5 years).

The remote model does not completely determine the model variability. In fact, apart from the low-frequency coastal variations, most of the model response, including the long-term average circulation and the annual variability at the coast (and at the interior), is determined by the local model through the curl of the wind stress and the variability of the alongshore winds.

The resulting long-term average ULT and geostrophic currents are encouraging. A very realistic current structure develops in which a Sverdrup balance is established. The main geostrophic equatorward currents dominate the response away from the coast. The model reproduces several peculiar features of the geostrophic circulation, most conspiciously the shoreward sweep of the southeastward flowing waters at about 32°N (see Figure 4). This feature, observed by *Reid and Schwartzlose* [1963] and described by *Pavlova* [1966], consists of a permanent shoreward bend in the main southward flowing current near 32°N.

Pavlova [1966] suggests that at some distance from the coast, the eastward current divides into a northward component that feeds the California countercurrent and the southern California eddy and a southward component that is part of the main southward flow [*Hickey*, 1979]. This description could have been drawn from our Figure 4. *Pavlova* [1966] speculates about the eastward rotation being caused by features of the bottom topography and by the pattern of prevailing wind along the coast. The fact that our model so consistently reproduces this feature dismisses topography as the main cause (our model does not include any topographic effects), leaving the second explanation as the most probable. In particular, it seems that the minimum in the tangential winds (magnitude of the projected winds in the general direction of the coast) around 34°N, due to the westward bend of the coast at the California bight, causes the splitting of the equatorward currents. This is done by abruptly diminishing the large-scale Ekman onshore transport and coastal downwelling at the bight.

For the local model, coastal wave propagation seems to be masked by Ekman advection. Cross-correlation analysis of the ULT signal along the boundary indicates a propagation speed that is too slow for baroclinic Kelvin waves. The ULT signal probably reproduces the propagation of the wind pattern through direct Ekman forcing (see Figure 11). Information in the remote model, on the other hand, propagates poleward freely along the eastern boundary. The speed, as implied by the ULT cross-correlation matrix (Figure 15) coincides with the theoretical Kelvin wave speed.

SPECTRUM

Eve
good
model
The
ing as
tation
nia C
be cor
curren
concer
someh
curren
other
eratio

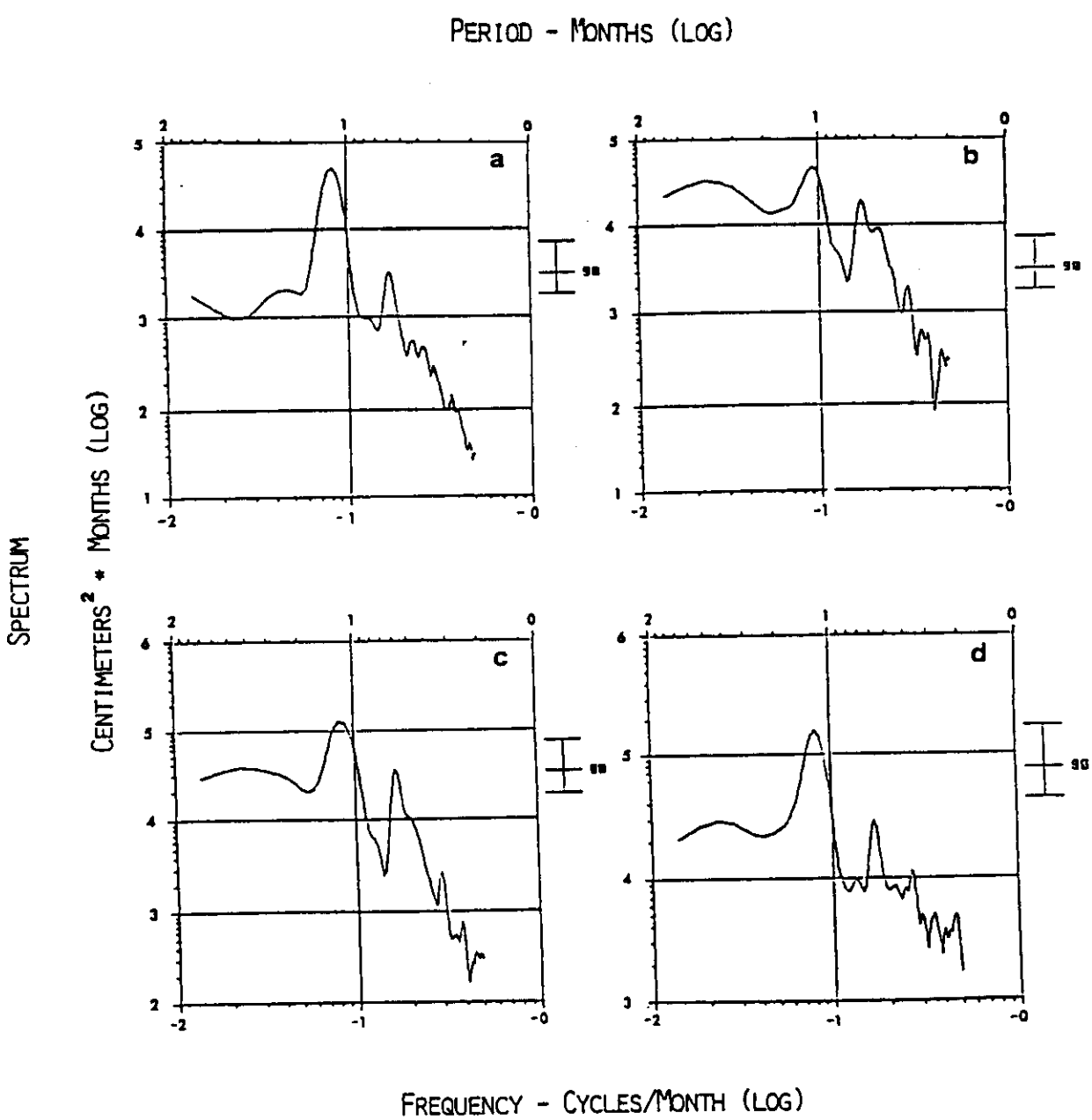

Fig. 23. Crescent City sea level spectra from (*a*) local model, (*b*) remote model, (*c*) local plus remote model, and (*d*) observations. Note that different scales were used for each spectrum. The 90% confidence intervals are shown to the right of each spectrum.

Even though the overall performance of the model is very good and there is a good agreement between observations and model, there are some limitations to this work.

The vertical resolution is poor owing to the vertical averaging associated with the reduced gravity equations. This limitation implies that one of the main constituents of the California Current system, i.e., the California undercurrents, cannot be considered as a separate entity. The influence of the undercurrent, however, inasmuch as its vertical integrated effect is concerned, is included in the model. In fact, it may be that the somehow longer than observed persistence of the countercurrent in the model is the result of the contribution of what otherwise would be an undercurrent. The mechanism for generation of an undercurrent (i.e., region of positive curl along an eastern boundary [*Pedlosky*, 1974; *McCreary et al.*, 1987]) in our model generates only a countercurrent.

A second limitation is the absence of bottom topography. This suppresses the possibility of having the topographic Rossby wave mode complementing the internal Kelvin waves along the eastern boundary (e.g., *Gill and Clarke*, 1974; *Allen*, 1975]. Evidence of this hybrid (part Kelvin and part shelf) wave activity in the eastern Pacific has been presented by *Clarke* [1977], *Christensen et al.* [1983], and *Wang and Mooers* [1977], among others. The theory of hybrid waves, however, has been most successfully used in explaining the character of wind-forced variability at frequencies (hours and days) much higher than those considered in this work (seasonal and interannual). It is not clear how much the presence of

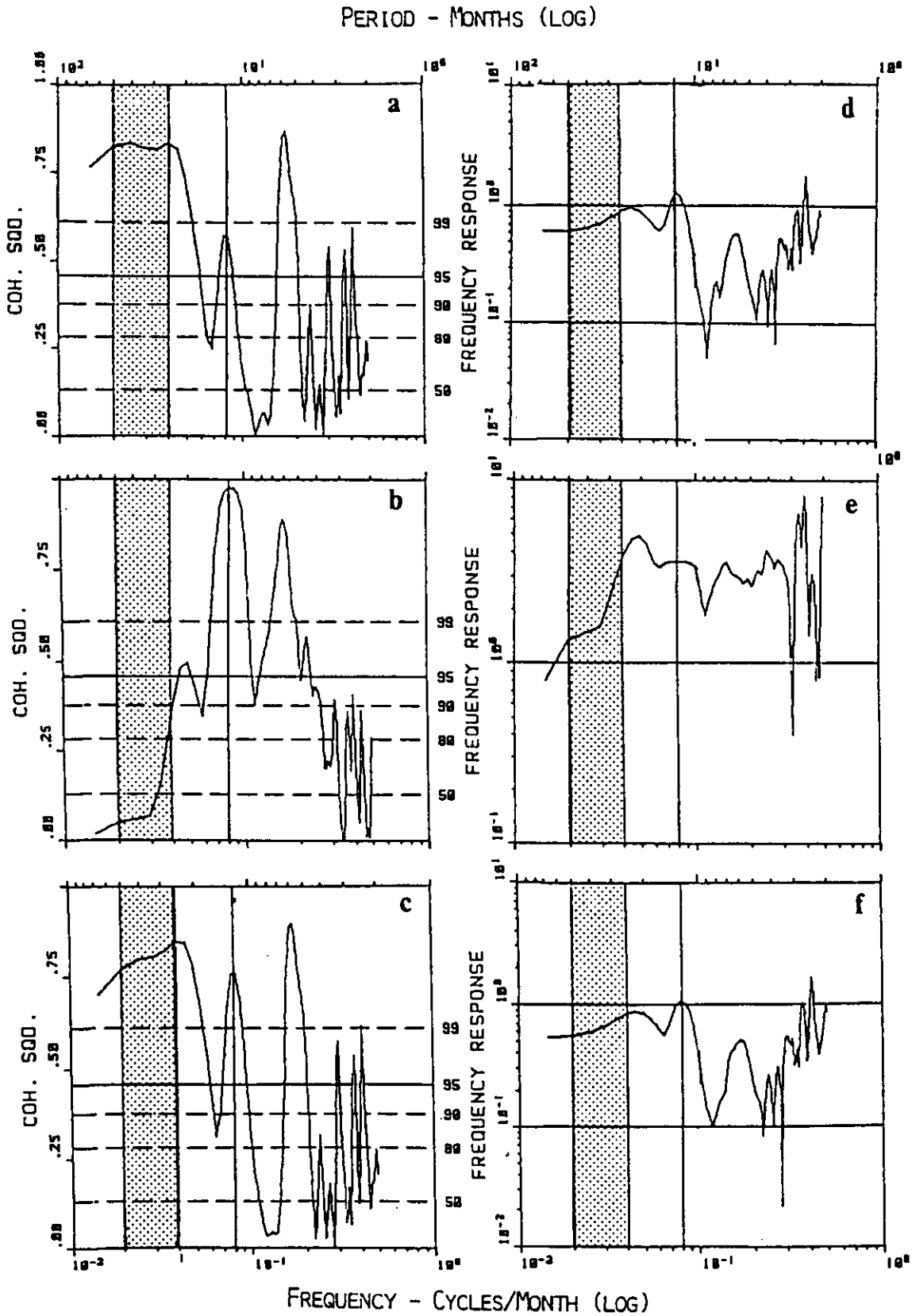

Fig. 24. Coherence square function (CSF) and frequency response function (FRF) between model and observed sea level at San Diego. (*a*) CSF between observations and remote model. (*b*) CSF between observations and local model. (*c*) CSF between observation and local plus model. (*d*) FRF between observations and remote model. (*e*) FRF between observations and local model. (*f*) FRF between observations and local plus remote model. For FRF the time series of observed values is assumed to be linearly related to the model time series. A value of 1 in the FRF at a given frequency indicates that the model and observation spectra contain the same amount of energy at that frequency. A value greater than 1 indicates that the model underestimates the energy of the observations. The 2–4 years band (El Niño band) was shaded, and a line at the annual frequency drawn as a visual aid.

the shelf and slope would affect the long-scale low-frequency event we analyzed. *McCreary et al.* [1987] used both flat bottom and shelf coastal models and found the responses at this scales very similar.

Large-scale topography features like the Mendocino escarpment presumably could influence the response by providing a mean for scatter of poleward propagation waves [e.g., *Chao et al.*, 1979; *Hsueh*, 1980] or by acting as a waveguide [e.g., *Longuet-Higgins*, 1968]. The actual result of these mechanisms would be to diminish the amount of energy transmitted north of Cape Mendocino. This could be one of the reasons why the magnitude of the interannual signal does not decrease poleward as much as is suggested by the observations, for example in the 1972 event.

The effect of submarine ridges and valleys on the upwelling pattern was demonstrated in a numerical study by *Peffley and O'Brien* [1976]. They show that bottom relief can be important in causing localized upwelling.

Acknowledgments. This work was supported by the National Science Foundation grant OCE-84-15986. Additional support was provided by the Consejo Nacional de Ciencia y Tecnología of Mexico and the Office of Naval Research under a URI award (USN N00014-86-K-0752) to Scripps Institution of Oceanography. The Supercomputer Center at Florida State University supplied the computer time for these calculations. Thanks are extended to K. Wyrtki for providing the sea level data used to validate our model. This study would have been impossible without such data. We also wish to thank Julian McCreary and an anonymous reviewer for their very useful comments on the manuscript.

REFERENCES

Allen, J. S., Coastal trapped waves in a stratified ocean, *J. Phys. Oceanogr.*, *5*, 300–325, 1975.

Allen, J. S., and D. W. Denbo, Statistical characteristics of the large scale response of coastal sea level to atmospheric forcing, *J. Phys. Oceanogr.*, *14*, 1079–1094, 1984.

Anderson, D. L. T., and P. B. Rowlands, The role of inertia-gravity and planetary waves in the response of a tropical ocean to the incidence of an equatorial Kelvin wave on a meridional boundary, *J. Mar. Res.*, *34*, 295–312, 1976.

Bendat, J. S., and A. G. Piersol, *Random Data: Analysis and Measurement Procedures*, Wiley-Interscience, New York, 1971.

Bjerkness, J., A possible response of the atmospheric Hadley circulation to equatorial anomalies in ocean temperature, *Tellus*, *18*, 820–829, 1966.

Brink, K. N., Coastal open physical processes, *Rev. Geophys.*, *25*, 204–216, 1987.

Camerlengo, A. L., and J. J. O'Brien, Open boundary conditions in rotating fluids, *J. Comput. Phys*, *35*, 12–35, 1980.

Chao, S.-Y., L. J. Pietrafesa, and G. S. Janowitz, The scattering of continental shelf waves by an isolated topographic irregularity, *J. Phys. Oceanogr.*, *9*, 687–695, 1979.

Chelton, D. B., and R. E. Davis, Monthly mean sea level variability along the west coast of North America, *J. Phys. Oceanogr.*, *12*, 757–784, 1982.

Christensen, N., R. De La Paz, and G. Gutierrez, A study of subinertial waves off the west coast of Mexico, *Deep Sea Res.*, *30*, 835–850, 1983.

Clarke, A. J., Observational and numerical evidence for wind-forced coastal trapped long waves, *J. Phys. Oceanogr.*, *7*, 231, 1977.

Clarke, A. J., The reflection of equatorial waves from oceanic boundaries, *J. Phys. Oceanogr.*, *13*, 1193–1207, 1983.

Cummins, P. F., L. A. Mysak, and K. Hamilton, Generations of annual Rossby waves in the North Pacific by the wind stress curl, *J. Phys. Oceanogr.*, *16*, 1179–1189, 1986.

Emery, W. J., and K. Hamilton, Atmospheric forcing of interannual variability in the northeast Pacific Ocean: Connections with El Niño, *J. Geophys. Res.*, *90*, 857–868, 1985.

Enfield, D. B., and J. S. Allen, On the structure and dynamics of monthly mean sea level anomalies along the Pacific coast of North and South America, *J. Phys. Oceanogr.*, *10*, 557–578, 1980.

Gill, A. E., *Atmosphere-Ocean Dynamics*, *Int. Geophys. Ser.*, vol. 30, 662 pp., Academic, London, 1982.

Gill, A. E., and A. J. Clarke, Wind-induced upwelling, coatal current and sea level changes, *Deep Sea Res.*, *21*, 325–345, 1974.

Grimshaw, R., and J. S. Allen, Low-frequency baroclinic waves off coastal boundaries, *J. Phys. Oceanogr.*, *18*, 1124–1143, 1988.

Halliwell, G. R., and J. S. Allen, Large-scale sea level response to atmospheric forcing along the west coast of North America, summer 1973, *J. Phys. Oceanogr.*, *14*, 864–886, 1984.

Halliwell, G. R., and J. S. Allen, The large-scale coastal wind field along the west coast of North America, 1981–1982, *J. Geophys. Res.*, *92*, 1861–1884, 1987.

Hickey, B. M., The California Current System—Hypothesis and facts, *Prog. Oceanogr.*, *8*, 279 pp., 1979.

Huyer, A., and R. L. Smith, The signature of El Niño off Oregon, 1982–1983, *J. Geophys. Res.*, *90*, 7133–7142, 1985.

Hsueh, Y., Scattering of continental shelf waves by longshore variations in bottom topography, *J. Geophys. Res.*, *85*, 1147–1150,

Kubota, M., and J. J. O'Brien, Variability of the upper tropical Pacific Ocean model, *J. Geophys. Res.*, *93*, 13,930–13,940, 1988.

Longuet-Higgins, M. S., Double Kelvin waves with continuous depth profiles, *J. Fluid Mech.*, *34*, 49–80, 1968.

Luther, M. E., and J. J. O'Brien, A model of the seasonal circulation in the Arabian Sea forced by observed winds, *Prog. Oceanogr.*, *14*, 353–385, 1985.

Lynn, R. L., and J. J. Simpson, The California Current system: The seasonal variability of its physical characteristics, *J. Geophys. Res.*, *92*, 12,947–12,966, 1987.

McCreary, J., Eastern tropical ocean response to changing wind stress systems: With application to El Niño, *J. Phys. Oceanogr.*, *6*, 632–649, 1976.

McCreary, J. P., and P. K. Kundu, Western boundary circulation driven by an alongshore wind: With application to the Somali Current system, *J. Mar. Res.*, *43*, 493–516, 1985.

McCreary, J. P., P. K. Kundu, and S. Chao, On the dynamics of the California Current system, *J. Mar. Res.*, *45*, 1–32, 1987.

Moore, D. W., Planetary-gravity waves in an equatorial ocean, Ph.D. dissertation, 207 pp., Harvard Univ., Cambridge, Mass., 1968.

Moore, D. W., and S. G. Philander, Modelling of the tropical ocean circulation, in *The Sea*, vol. 6, edited by E. D. Goldberg et al., Wiley-Interscience, New York, 1977.

Munk, W. H., On the wind-driven ocean circulation, *J. Meteorol.*, *7*, 79–93, 1950.

Mysak, L. A., Generation of annual Rossby waves in the North Pacific, *J. Phys. Oceanogr.*, *13*, 1908–1923, 1983.

Namias, J., Some statistical and synoptic characteristics associated with El Niño, *J. Phys. Oceanogr.*, *6*, 130–138, 1976.

Nelson, C. S., Wind stress and wind stress curl over the California Current, *NOAA Tech. Rep., NMFS SSRF-714*, 1977.

Pavlova, Yu. V., Seasonal variations of the California Current, *Oceanology*, *6*, 806–814, 1966.

Pearcy, W. G., and A. Schoener, Changes in the marine biota coincident with the 1982–1983 El Niño in the northeastern subarctic Pacific Ocean, *J. Geophys. Res.*, *92*, 14,417–14,428, 1987.

Pedlosky, J., Longshore currents, upwelling and bottom topography, *J. Phys. Oceanogr.*, *4*, 214–226, 1974.

Peffley, M. B., and J. J. O'Brien, A three-dimensional simulation of coastal upwelling off Oregon, *J. Phys. Oceanogr.*, *6*, 164–180, 1976.

Philander, S. G. H., and J. H. Yoon, Eastern boundary currents and coastal upwelling, *J. Phys. Oceanogr.*, *12*, 862–879, 1982.

Quinn, W. H., D. O. Zopf, K. S. Short, and R. T. W. Kuo Yang, Historical trends and statistics of the southern oscillation, El Niño, and Indonesian droughts, *Fish. Bull.*, *76*, 663–678, 1984.

Reid, J. L., and A. Mantyla, The effect of the geostrophic flow upon coastal sea elevations in the northern North Pacific Ocean, *J. of Geophys. Res.*, *81*, 3100–3110, 1976.

Reid, J. L., and R. A. Schwartzlose, Direct measurements of the Davidson Current off central California, *J. Geophys. Res.*, *67*, 2491–2497, 1962.

Reid, J. L., and R. A. Schwartzlose, Direct measurements of a small surface eddy off northern Baja California, *J. Mar. Res.*, *21*, 205–218, 1963.

Reid, J. L., G. L. Roden, and J. G. Wyllie, Studies of the California Current system, progress report, 1 July 1956 to 1 January 1958, Calif. Coop. Ocean Fish. Invest., La Jolla, 1958.

Rienecker, M. M., and L. L. Ehret, Wind stress curl variability over

the North Pacific from the Comprehensive Ocean-Atmosphere Data Set, *J. Geophys. Res.*, *93*, 5069–5077, 1988.

Rienecker, M. M., and C. N. K. Mooers, The 1982–1983 El Niño signal off northern California, *J. Geophys. Res.*, *91*, 6597–6608, 1986.

Simpson, J. J., Large-scale thermal anomalies in the California Current during the 1982–1983 El Niño, *Geophys. Res. Lett.*, *10*, 937–940, 1983.

Simpson, J. J., El Niño-induced onshore transport in the California Current during 1982–83, *Geophys. Res. Lett.*, *11*, 233, 1984*a*.

Simpson, J. J., A simple model of the 1982–83 California "El Niño", *Geophys. Res. Lett.*, *11*, 243–246, 1984*b*.

Sverdrup, H. U., M. W. Johnson, and R. H. Fleming, *The Oceans, Their Physics, Chemistry and General Biology*, 1087 pp., Prentice-Hall, Englewood Cliffs, N. J., 1942.

Wang, D. P., and C. N. K. Mooers, Coastal-trapped waves in a continuously stratified ocean, *J. Phys. Oceanogr.*, *6*, 853–863, 1976.

White, W. B., and J. F. T. Saur, A source of annual baroclinic waves in the eastern subtropical North Pacific, *J. Phys. Oceanogr.*, *11*, 1452–1462, 1981.

Wooster, W. S., and D. L. Fluharty, *El Niño North: Niño Effects in the Eastern Subartic Pacific Ocean*, 313 pp., Washington Sea Grant Program, University of Washington, Seattle, 1985.

J. J. O'Brien, Mesoscale Air-Sea Interaction Group, Florida State University, Tallahassee, FL 32306.

A. Pares-Sierra, Scripps Institution of Oceanography, La Jolla, CA 92093.

(Received April 19, 1988;
accepted October 14, 1988.)